

2015

# Robot dexterity: from deformable grasping to impulsive manipulation

Huan Lin

*Iowa State University*

Follow this and additional works at: <https://lib.dr.iastate.edu/etd>

 Part of the [Computer Sciences Commons](#), and the [Robotics Commons](#)

## Recommended Citation

Lin, Huan, "Robot dexterity: from deformable grasping to impulsive manipulation" (2015). *Graduate Theses and Dissertations*. 14929.  
<https://lib.dr.iastate.edu/etd/14929>

This Dissertation is brought to you for free and open access by the Iowa State University Capstones, Theses and Dissertations at Iowa State University Digital Repository. It has been accepted for inclusion in Graduate Theses and Dissertations by an authorized administrator of Iowa State University Digital Repository. For more information, please contact [digirep@iastate.edu](mailto:digirep@iastate.edu).

**Robot dexterity: From deformable grasping to impulsive manipulation**

by

**Huan Lin**

A dissertation submitted to the graduate faculty  
in partial fulfillment of the requirements for the degree of  
**DOCTOR OF PHILOSOPHY**

Major: Computer Science

Program of Study Committee:

Yan-Bin Jia, Major Professor

David Fernandez-Baca

James Oliver

Greg Luecke

Guang Song

Iowa State University

Ames, Iowa

2015

Copyright © **Huan Lin**, 2015. All rights reserved.

## DEDICATION

I would like to dedicate this thesis to my family without whose support I would not have been able to complete this work. I would also like to thank my friends for their loving guidance and during the writing of this work.

## TABLE OF CONTENTS

<b>LIST OF TABLES</b> . . . . .	vii
<b>LIST OF FIGURES</b> . . . . .	viii
<b>ACKNOWLEDGEMENTS</b> . . . . .	x
<b>ABSTRACT</b> . . . . .	xi
<b>CHAPTER 1. INTRODUCTION</b> . . . . .	1
<b>CHAPTER 2. RELATED WORK</b> . . . . .	4
2.1 Rigid Body and Deformable Grasping . . . . .	4
2.2 Impact Modeling and Planning . . . . .	6
<b>CHAPTER 3. ROBUSTNESS OF DEFORMABLE 2D GRASP</b> . . . . .	8
3.1 Linear Plane Elasticity . . . . .	9
3.2 Foundation of Squeezing . . . . .	10
3.3 Stable Squeeze . . . . .	11
3.4 Pure Squeeze . . . . .	13
3.5 Resisting an Adversary Finger . . . . .	14
3.5.1 Fixed Point Contacts . . . . .	15
3.5.2 Fixed Segment Contacts . . . . .	18
3.5.3 Frictional Segment Contacts . . . . .	19
3.5.4 Simulation and Experiment on Grasp Resistance . . . . .	22

<b>CHAPTER 4. PICKING UP SOFT 3D OBJECTS . . . . .</b>	<b>28</b>
4.1 Linear Elasticity . . . . .	28
4.2 The Finite Element Method with Gravity . . . . .	29
4.3 Deformation from Specified Contact Displacements . . . . .	31
4.4 Grasping to Pick up a Solid . . . . .	32
4.4.1 Updating Shape and Contact Configuration . . . . .	34
4.4.2 Liftability Test . . . . .	38
4.4.3 Experiment . . . . .	40
<b>CHAPTER 5. MODELING OF <i>N</i>-BODY COLLISIONS . . . . .</b>	<b>45</b>
5.1 Frictionless Collision of Translating Balls . . . . .	45
5.1.1 Impact Dynamics and Contact Kinematics . . . . .	45
5.1.2 Numerical Integration . . . . .	48
5.1.3 Example . . . . .	49
5.2 Collision under General Motions with Friction . . . . .	51
5.2.1 Impact Dynamics and Contact Kinematics . . . . .	51
5.2.2 Contact Modes . . . . .	53
5.2.3 Algorithm . . . . .	55
5.3 Simulation and Experiment . . . . .	56
5.3.1 Newton's Cradle . . . . .	56
5.3.2 Billiard Break Shots . . . . .	58
<b>CHAPTER 6. BATTING A FLYING OBJECT TO TARGET . . . . .</b>	<b>61</b>
6.1 Task Description . . . . .	61
6.2 Two-Dimensional Frictionless Impact Planning . . . . .	62
6.2.1 Impact Dynamics and Contact Kinematics . . . . .	62
6.2.2 Motion Planning . . . . .	65
6.2.3 Reachable Region . . . . .	66
6.2.4 Simulation and Experiment . . . . .	70

6.3	Two-Dimensional Frictional Impact Planning . . . . .	72
6.3.1	Impact Dynamics and Contact Kinematics . . . . .	72
6.3.2	Impact planing . . . . .	76
6.4	Three-Dimensional Frictionless Impact Planning . . . . .	77
6.4.1	Impact Dynamics and Contact Kinematics . . . . .	77
6.4.2	Motion Planning . . . . .	78
6.5	Three-Dimensional Frictional Impact Planning . . . . .	80
6.5.1	Impact Dynamics and Contact Kinematics . . . . .	80
6.5.2	Motion Planning . . . . .	84
<b>CHAPTER 7. CONCLUSION . . . . .</b>		<b>93</b>
<b>BIBLIOGRAPHY . . . . .</b>		<b>95</b>

## LIST OF TABLES

Table 3.1	Forces exerted and work performed by the the two grasping fingers in Figure 3.5. . . . .	22
Table 3.2	Forces exerted and work performed by $\mathcal{F}_1$ and $\mathcal{F}_2$ in Figure 3.7. . . . .	24
Table 4.1	Parameters with the objects in Figure 4.3 and 4.4. . . . .	43
Table 4.2	Experimental results for five different objects. . . . .	44
Table 5.1	Comparisons of experimental and simulation outcomes for Newton's cradle. . . . .	57
Table 5.2	Parameters used for modeling break shots. . . . .	59
Table 6.1	Contact modes of impact. . . . .	73
Table 6.2	Iterations of Newton's method. . . . .	86

## LIST OF FIGURES

Figure 3.1	Thin flat object. . . . .	9
Figure 3.2	Comparison between unit stable and pure squeezes. . . . .	14
Figure 3.3	Grasp resistance to a translating adversary finger $\mathcal{A}$ . . . . .	15
Figure 3.4	A grasp resisting an adversary finger. . . . .	17
Figure 3.5	Resisting an adversary semicircular fingertip under friction. . . . .	25
Figure 3.6	Experimental setup for resisting an adversary fingertip. . . . .	26
Figure 3.7	Experiment for resisting an adversary finger. . . . .	27
Figure 4.1	Sliding of a node on the plane. . . . .	35
Figure 4.2	Sliding of a node on the plane. . . . .	36
Figure 4.3	Liftability test for a tomato. . . . .	41
Figure 4.4	Objects (a) at rest and (b) in tetrahedral mesh representations. . . . .	42
Figure 4.5	Successful pickups of four deformable objects. . . . .	44
Figure 5.1	Contact modeling with virtual springs. . . . .	47
Figure 5.2	Newton's cradle initial status . . . . .	50
Figure 5.3	Impulse decomposition along normal and tangential directions. . . . .	52
Figure 5.4	Initial State of Newton's cradle in experiment. . . . .	57
Figure 5.5	Comparison of Newton's cradle. . . . .	58
Figure 5.6	Billiards break shot. . . . .	59
Figure 5.7	Resting configurations of ten balls after break shots. . . . .	60
Figure 6.1	Batting an object to a target destination. . . . .	62



Figure 6.2	Example of reachable regions of the object. . . . .	87
Figure 6.3	Magnitude of linear velocity from image processing, kinematics, and the Kalman filter's estimation. . . . .	88
Figure 6.4	Trajectories of the planning task. . . . .	88
Figure 6.5	Discrepancies between experiment and simulation along time in position and orientation. . . . .	89
Figure 6.6	Solution surface of the frictional planning example for different hitting normal, tangential velocity, and normal velocity of the manipulator. . . . .	90
Figure 6.7	Trajectory of the optimal planning result. . . . .	90
Figure 6.8	Solution curve of the 3D frictionless planning example for different hitting normal. . . . .	91
Figure 6.9	Kinetic energy curve of the 3D frictionless planning example for different $\phi$ and $\theta$ . . . . .	91

## ACKNOWLEDGEMENTS

I would like to take this opportunity to express my thanks to those who helped me with various aspects of conducting research and the writing of this thesis. First and foremost, Dr. Yan-Bin Jia for his guidance, patience and support throughout this research and the writing of this thesis. His insights and words of encouragement have often inspired me and renewed my hopes for completing my graduate education.

I would also like to thank my committee members for their efforts and contributions to this work: Dr. David Fernandez-Baca, Dr. Greg Luecke, Dr. James Oliver and Dr. Guang Song.

The Robotics Lab has provided a great environment for my study and research. All my lab members, Feng Guo, HyunTae Na, Rex Fernando, Feifei Wang, Sean Strickland, Trenton Anagnostopoulos, Matthew Gardner, Jiale Feng and Jacob Stimes have made it an exciting place. I am very much thankful to them all.

Support for this research has been provided in part by Iowa State University, and in part by the National Science Foundation through the grants IIS-0915876 and IIS-1421034. Any opinions, findings and conclusions in this dissertation are those of the author and do not necessarily reflect the views of the National Science Foundation.

## ABSTRACT

Nowadays, it is fairly common for robots to manipulate different objects and perform sophisticated tasks. They lift up massive hard and soft objects, plan the motion with specific speed, and repeat complex tasks with high precision. However, without carefully control, even the most sophisticated robots would not be able to achieve a simple task.

Robot grasping of deformable objects is an under-researched area. The difficulty comes from both mechanics and computation. First, deformation caused by grasping motions changes the global geometry of the object. Second, different from rigid body grasping whose torques are invariant, the torques exerted by the grasping fingers vary during the deformation.

Collision is a common phenomenon in robot manipulation that takes place when objects collide together, as observed in the games of marbles, billiards, and bowling. To make the robot purposefully make use of impact to perform better at certain tasks, a general and computationally efficient model is needed for predicting the outcome of impact. And also, tasks to alter the trajectory of a flying object are also common in our daily life, like batting a baseball, playing ping-pong ball. A good motion planning strategy based on impact is necessary for the robots to accomplish these tasks.

The thesis investigates problems of deformable grasping and impact-based manipulation on rigid bodies. The work contains deformable grasping on 2D and 3D soft objects, multi-body collision modeling, and motion planning of batting a flying object.

In the first part of the thesis, in 2D space an algorithm is proposed to characterize the best resistance by a grasp to an adversary finger which minimizes the work done by the grasping fingers. An optimization scheme is offered to handle the general case of

frictional segment contact. And also, an efficient squeeze-and-test strategy is introduced for a two-finger robot hand to grasp and lift a 3D deformable object resting on the plane.

Next, an  $n$ -body impulse-based collision model that works with or without friction is studied. The model could be used to determine the post-collision motions of any number of objects engaged in the collision. Making use of the impact model, the final part of the thesis investigated the task of batting a flying object with a manipulator. First, motion planning of the task in 2D space is studied. In the frictionless case, a closed-form solution is analyzed, simulated, and validated via the task of a WAM Arm batting a hexagonal object. In the frictional case, contact friction introduces a continuum of solutions, from which we select the one that expends the minimum kinetic energy of the manipulator. Next, analyses and results are generalized to 3D. Without friction the problem ends up with one-dimensional set of solution, from which optimum is obtained. For frictional case hitting normal is fixed for simplicity. The system is then transferred to a root-finding problem, and Newton's method is applied to find the optimal planning.

## CHAPTER 1. INTRODUCTION

The difficulty of robot grasping of deformable objects comes from not only mechanics but also computation. First of all, deformation caused by the grasp actions alters the global geometry of the object. Second, during deformation an object's contacts with the fingers grow from points into areas. Inside the contact area, contact points that stick to the finger may later slide while points that slide may stick later. The torques exerted by the grasping fingers are changing during the deformation, different from rigid body grasping whose torques are invariant.

In the first part of the thesis , we investigate how to characterize the quality of a squeeze grasp in 2D grasping proposed in (15). A successful rigid body grasp should not cause any movement of the contact points. However, on deformable objects, the grasping fingers perform some work due to deformation, most of which is converted to strain energy. Therefore, it makes sense to have an energy-based metric for measuring the quality of grasp. The deformation-space approach (14) was proposed by Gopalakrishnan and Goldberg to characterize the optimal grasp as the one from which the potential energy needed for a release equals the amount at the elastic limit of the object. In this thesis, we present a measure by the amount of the work performed by the grasping fingers to resist a disturbing finger under known displacement.

Next, a simple strategy is introduced for a robot hand without using tactile sensing to pick up 3D deformable objects at rest. Human hands are experienced at handling deformable objects in daily life. To pick up a soft object resting on the table, for instance, human hand usually squeezes it using two or more fingers to achieve a firm grasp, using

the table's support to maintain stability. After that, while considering the object's mass and contact friction, the hand begins to lift the object up at some point. During the lift as an increasing portion of the weight is felt, the hand may apply extra squeeze to prevent slips. Inspired by human hand grasping, our strategy for robot hands is to squeeze the object and after every extra amount of squeeze, a quick liftability test is performed to check if the object is able to be lifted. Once the test is passed, the fingers stop squeezing and pick up the object via upward translation. Through out the process, the object is fully constrained by the grasping fingers, with or without the supporting plane.

The second part of this thesis introduces an  $n$ -body impulse-based collision model that works in both frictionless and frictional cases. The model can be applied to determine the motions after impact of any number of objects involved in the collision. We will focus on the case where the objects' centers of mass engaged in the collision are coplanar.

Adopting the analysis from (21), which focused on three-body impact only, we set up a system for frictionless collisions of  $n$  balls. During one collision process, impulses and energies at the contacts are tracked via numerical integration based on their differential relationships to the dominant impulse, which switches from one period to another. To initialize the impulse derivatives, instead of using wave propagation (29) and (30), we set up a system of equations and solve it numerically using Newton's method. This avoids a tedious analysis that enumerates all possible topologies of active contacts during the collision. An energetic coefficient of restitution (54) is employed for tracking the energy loss.

Taking advantage of the impact model proposed, we next investigate how to batting a moving object to a target destination. Impact planning in both 2D and 3D cases with and without friction is studied. In 2D frictionless case, *reachable region*, which is the feasible region that can be reached by the object given pre-planned configuration via varying impact normal and pre-impact velocity of the manipulator, is presented. In the 2D frictional case considering tangential impulse, multiple solutions exist with an additional

degree of freedom (tangential velocity of the manipulator). The kinetic energy of the manipulator is introduced as a metric to characterize the effort of batting. Numerical methods are applied to search for the optimal pre-impact motion of the manipulator. In the 3D case without friction, solutions end up with a one-dimensional 3D curve. The optimal planning is also achieved by minimizing the kinetic energy of the manipulator. When friction is introduced, hitting normal is fixed to reduce degrees of freedom. The problem is then converted into a root-finding problem which is solved using Newton's method.

The thesis uses meter for length, kilogram for mass, Pascal for pressure, Newton for force, and Joule for work and energy. The units are omitted from now on.

The rest of the manuscript is organized as follows. Chapter 2 surveys related work in robot grasping on rigid body and deformable objects, collision modeling, and impact planning. Chapter 3 will briefly review the foundation of squeezing, and then construct grasps that perform minimum work to resist a disturbing finger, progressing from the cases of fixed point and segment contacts to that of frictional segment contacts. In Chapter 4, we propose a simple strategy for a robot hand to grasp and lift a deformable 3D object sitting on a table. In Chapter 5, a multi-body impact model is introduced which is applicable with or without friction. Chapter 6 investigates the task of batting an flying object to a target by impact planning. Finally, Chapter 7 summarizes the thesis.

## CHAPTER 2. RELATED WORK

In this chapter, we will survey some related work on grasping and impact.

### 2.1 Rigid Body and Deformable Grasping

Rigid body grasping is a widely studied area rich with theoretical analyses, simulations, and experiments with robotic hands (2). First-order form closure (46) is regarded as equivalent to force closure without friction. Mishra (38) offered upper bounds on the numbers of contact points sufficient and/or necessary for form closure. Later tighter bounds for 2D and 3D objects with piecewise smooth boundaries were derived (32). Algorithms were developed to compute all form closure grasps of polygonal parts (5; 53). There was also some work (45; 47) focusing on caging an object with frictionless contacts so that it could move inside freely but never escape.

Two-finger force-closure grasps of planar objects are shown to be efficiently computable for both polygons (40) and piecewise smooth curved shapes (43). Ponce (42) also developed algorithms for grasping 3D objects. Trinkle (57) formulated the force-closure test as a linear program with an objective function characterizing the quality as the distance from losing the closure.

The introduction of task ellipsoid (28) proposed the idea that the choice of a grasp should be based on the capacity to generate wrenches that were relevant to the task. Grasp quality measures for multi-finger hands were introduced to consider selection of internal grasping forces that were furthest from violating any closure, friction, or mechan-



ical constraints (24), or were directly derived from the grasp matrix which characterized the wrench space of a grasp (28). Grasp metrics for polygons and polyhedra usually aimed to maximize the worst-case external force that could be resisted by a unit grasping force (33; 37; 22). A summary on various grasp metrics was given by Mishra (36), addressing the trade-offs among grasp quality, the number of fingers, object geometry, and the efficiency for grasp synthesis. Some recent work (6; 4) applied semidefinite programming techniques to minimize the maximum magnitude of the contact force at any frictional contact of a grasp to maintain equilibrium to resist a known external wrench .

There was little work when it comes to deformable grasping, a difficult problem that needs to handle with changing local contact geometry as well as the global object geometry caused by the deformation. The notion of bounded force-closure (60) was introduced for this type of grasps. Hirai (16) controlled the motion of a grasped deformable object using visual and tactile information. The deformation-space approach (14) characterized the optimal grasp of a deformable part as the one from which the potential energy needed for a release is equal to the amount at the object's elastic limit.

In contrast, manipulation of flexible linear objects such as wires or ropes has been an extensively studied area, with work on static modeling (59), knotting and unknotting (49; 35; 26; 58), pickup (44), and path planning (39). However, these operations can be implemented without the requirement for deformable modeling.

Moreover, Sinha and Abel (52) proposed a model for deformation of the contact regions under a grasp, which predicts normal and tangential contact forces without concerning global deformation or grasp computation. Luo and Xiao (31) showed that simulation accuracy and efficiency could be improved based on the derived geometric properties at a contact. Tian and Jia (56) investigated deformable modeling of shell-like objects that were already grasped by point contacts.

More thorough investigations on the elastic contact problem were conducted by the mechanics community regarding the contact area between two deformable bodies under

a known external load. The gradual physical process implies iterative updates of the increasing contact region(s). Francavilla and Zienkiewicz (11) offered an FEM-based solution for 2D elastic contact problems under frictionless contacts. It was then extended to incorporate Coulomb friction by Okamoto and Nakazawa (41) and Sachdeva and Ramakrishnan (48) via iterative updates of the contact area and the contact modes of nodes. In each iteration, FEM computed the deformed shape according to position and friction constraints derived from the contact modes under Coulomb friction. This event-driven approach was extended by Chandrasekaran et al. (7) to deal with geometric nonlinearities and node-edge contacts to solve for the exact loading condition from designated displacements.

Guo(15) investigated squeeze grasping of deformable 2D objects. One of the ideas reflecting a key difference from rigid body grasping, was to specify the finger movements instead of finger forces. The reason is that force and torque equilibrium are guaranteed over a deformable body which is fully constrained, following (8), (3). Another idea was to obtain the constraints needed to update the deformed shape from the contact sets with the fingers, which are maintained by an event-driven way during the deformation.

## 2.2 Impact Modeling and Planning

Collisions happen in daily life are usually plastic, which do not conserve kinetic energy. Solution of a collision problem requires determining the post-impact velocities of the impact objects from their pre-impact configurations and velocities. The problem is under-constrained by momentum conservation alone. Impact laws need to be imposed accordingly. There are three widely used laws: Newton's law, Poisson's hypothesis, and the energy hypothesis, which specify the ratios between the velocities before and after the impact. The impulse increases during different impact phases, and the strain energies stored and released during those phases. (20) presents a progressive overview of the

research in impact mechanics based on these laws.

In (29) Liu et al. introduced a framework for frictionless multiple impacts in a multi-body system. Numerical integration is performed over the impulse at the contact currently having the maximum potential energy. Energetic coefficients of restitution are applied to individual impacts, each of which may go through multiple compression-restitution phase transitions. Their sequel paper (30) developed a numerical algorithm and presented simulation results for several benchmark problems including Newton's cradle, the Bernoulli problem, etc. It did not analyze the impact behavior during the accumulation of impulses, and did not provide a proof for termination of the algorithm.

Around the same time, Jia et al. (21) proposed a simultaneous impact model that keeps track of contact strain energy. The main difference from the framework of (29) is that this model formulates the physical process as a state transition diagram, where each state represents a different combination of active contacts. A state transition happens when either an active impact finishes impact phase or an inactive impact gets reactivated. Every impact instance yields a sequence of states with proven termination.

Impact planning determines the hitting velocity of the manipulator and a point on an object to strike at. Also, it needs to take into account trajectory planning since after impact the object acts as a free motion. Not much work exists on impact planning, but noticeable work for impulsive manipulation includes (23), (18), (55), (17) and (62).

Batting an object is much easier to perform than to analyze in terms of mechanics. (9) focused on the swing trajectory and the force/torque required to generate it, applying Newton's law of impact (25). Senoo et al. proposed a hybrid trajectory generator as a motion plan for a high-speed robot system to bat the baseball (51). They then extend the algorithm to control the direction of the ball motion after impact (50), though there was no control over the ball's post-impact trajectory.

## CHAPTER 3. ROBUSTNESS OF DEFORMABLE 2D GRASP

This chapter begins with a review of plane linear elasticity, and then introduces the notions of pure and stable squeezes of an deformable object by specifying movements of a subset of boundary points. Finally, we will consider adversary finger resistance.

In this chapter we assume that the entire operation causes by small deformations of the object which can be described within the scope of linear elasticity. In the classical elasticity theory, deformation happens instantaneously. Here we will sometimes consider deformation as a continuous process which happens in an infinitesimal amount of time, in order to capture the varying contact area between the object and the fingers and the changing contact modes of nodes.

For 2D grasping, we make the following assumptions:

1. The object is isotropic, and either planar or thin  $2-\frac{1}{2}$ D.
2. Gravity is ignored.
3. The fingers are rigid and coplanar with the object and make frictional contact with it.

And also the fingers are with semicircular tips in 2D grasping and with hemispherical tips in 3D case.

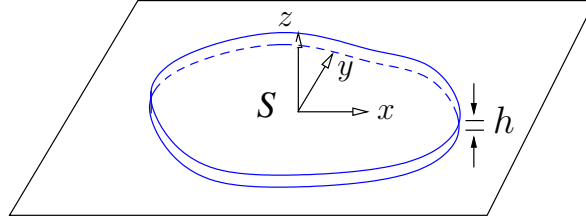


Figure 3.1 Thin flat object.

### 3.1 Linear Plane Elasticity

Consider a thin flat object shown in Figure 3.1 with thickness  $h$  significantly less than its two other dimensions. Essentially, the object is a generalized cylinder which results from translating the region  $S$  bounded by a closed simple curve in the  $xy$ -plane along the  $z$ -direction upward and downward each by  $h/2$ . The origin is placed at the centroid of  $S$ .

In this part, we consider *plane stress* (12) parallel to the  $xy$ -plane which means zero normal stress along the  $z$ -axis and zero shear stresses in the  $xz$ - and  $yz$ -planes. Under a *displacement field*  $\delta = (u(x, y), v(x, y))^T$ , every point  $(x, y)^T$  inside  $S$  moves to  $(x + u, y + v)^T$ . The same displacement applies to the points of the object that are vertically above or below the point  $(x, y)^T$ . The normal strains  $\epsilon_x$  and  $\epsilon_y$  along the  $x$ - and  $y$ -axes, respectively, and the shearing strain  $\gamma_{xy}$  are given below:

$$\begin{aligned}\epsilon_x &= \frac{\partial u}{\partial x}, \\ \epsilon_y &= \frac{\partial v}{\partial y}, \\ \gamma_{xy} &= \frac{\partial u}{\partial y} + \frac{\partial v}{\partial x}.\end{aligned}\tag{3.1}$$

Under Hooke's law, the following stress-strain relationships hold:

$$\begin{aligned}\epsilon_x &= \frac{\sigma_x - \nu\sigma_y}{E}, \\ \epsilon_y &= \frac{\sigma_y - \nu\sigma_x}{E}, \\ \gamma_{xy} &= \frac{\tau_{xy}}{G} = \frac{2(1 + \nu)}{E}\tau_{xy},\end{aligned}\tag{3.2}$$

where  $E$  and  $\nu$  are Young's modulus and Poisson's ratio of the material, respectively,  $\sigma_x$  and  $\sigma_y$  are the normal stress components in the  $x$ - and  $y$ -directions, respectively, and  $\tau_{xy}$  is the shear stress in the  $x$ - $y$  plane. The strain energy of the object (8) is

$$U = \frac{h}{2} \iint_S \left( \frac{E}{1-\nu^2} (\epsilon_x^2 + 2\nu\epsilon_x\epsilon_y + \epsilon_y^2) + \frac{E}{2(1+\nu)} \gamma_{xy} \right) dx dy. \quad (3.3)$$

Suppose  $\boldsymbol{\delta}$  is the displacement vector caused by external forces applied in the plane at some boundary points, which forms a set  $\Gamma$ . Denote by  $\mathbf{f}(x, y)$  the force exerts at point  $(x, y)^T \in \Gamma$ . The total potential of the applied forces is

$$W = - \sum_{(x,y)^T \in \Gamma} \boldsymbol{\delta}(x, y)^T \mathbf{f}(x, y). \quad (3.4)$$

The total potential energy of the system is

$$\Pi = U + W. \quad (3.5)$$

The principle of minimum potential energy states that  $\boldsymbol{\delta}$  minimizes  $\Pi$ .

### 3.2 Foundation of Squeezing

This section goes through a quick review of (15) on squeeze grasp with two fingers in 2D grasping. The cross section of the object is discretized into small uniform triangular elements with  $n$  vertices. Minimization of the potential energy yields the familiar constitutive equation:  $K\boldsymbol{\delta} = \mathbf{f}$ , where  $K$  is the object's stiffness matrix that is symmetric and positive semi-definite with rank  $2n - 3$ ,  $\boldsymbol{\delta}$  is the displacement vector, and  $\mathbf{f}$  is the external force vector.

The matrix assumes a spectral decomposition that

$$K = V\Lambda V^T, \quad (3.6)$$

where  $V = (v_{ij}) = (\mathbf{v}_1, \mathbf{v}_2, \dots, \mathbf{v}_{2n})$  and  $\Lambda = \text{diag}(\lambda_1, \dots, \lambda_{2n-3}, 0, 0, 0)$ . The null space of  $K$  is spanned by the following three vectors which represent translations and pure

rotation:

$$\mathbf{v}_{2n-2} = \frac{(1, 0, \dots, 1, 0)^T}{\sqrt{n}}, \mathbf{v}_{2n-1} = \frac{(0, 1, \dots, 0, 1)^T}{\sqrt{n}}, \text{ and } \mathbf{v}_{2n} = \frac{\mathbf{r}}{\|\mathbf{r}\|}, \quad (3.7)$$

where  $\mathbf{r}$  is the component of  $(-y_1, x_1, \dots, -y_n, x_n)^T$  that is orthogonal to  $\mathbf{v}_{2n-2}$  and  $\mathbf{v}_{2n-1}$ .

The grasp strategy is to specify the displacements  $\boldsymbol{\delta}_t$  of  $m$  boundary contact nodes  $\mathbf{p}_t$ ,  $t \in \mathbb{I}$ . Denote by  $\bar{\mathbf{v}}_l$ ,  $1 \leq l \leq 2m$ , the  $2m$ -vector that aggregates  $v_{2t-1,l}$  and  $v_{2t,l}$ , for all  $t \in \mathbb{I}$ , in the increasing index order. Introduce the matrix

$$M = \begin{pmatrix} A & B \\ B^T & \mathbf{0} \end{pmatrix}, \quad (3.8)$$

where  $A = \sum_{l=1}^{2n-3} \frac{1}{\lambda_l} \bar{\mathbf{v}}_l \bar{\mathbf{v}}_l^T$  and  $B = (\bar{\mathbf{v}}_{2n-2}, \bar{\mathbf{v}}_{2n-1}, \bar{\mathbf{v}}_{2n})$ . It was shown in (15) that the  $(2m+3) \times (2m+3)$  matrix  $M$  has an inverse when  $m \geq 2$ :

$$M^{-1} = \begin{pmatrix} C & E \\ E^T & -E^T A E \end{pmatrix}, \quad (3.9)$$

where  $C$  is symmetric and of dimension  $2m \times 2m$ .

Deformation is uniquely determined for  $m \geq 2$  under specified  $\boldsymbol{\delta}_t$ ,  $t \in \mathbb{I}$ , and  $\mathbf{f}_l = 0$ ,  $l \notin \mathbb{I}$ . Apply the same bar notation to select entries with indices  $i \in \mathbb{I}$  from the force vector  $\mathbf{f}$  and the displacement field  $\boldsymbol{\delta}$ . We have

$$\bar{\mathbf{f}} = C \bar{\boldsymbol{\delta}} \quad \text{and} \quad \boldsymbol{\delta} = H \bar{\boldsymbol{\delta}}, \quad (3.10)$$

for some  $2n \times 2m$  matrix  $H$ . The submatrix  $C$  is referred to as the *reduced stiffness matrix*. The strain energy of the object is

$$U = \frac{1}{2} \bar{\boldsymbol{\delta}}^T C \bar{\boldsymbol{\delta}}. \quad (3.11)$$

### 3.3 Stable Squeeze

Denoted by  $\mathcal{G}(\mathbf{p}_i, \mathbf{p}_j)$  the placement of two fingers  $\mathcal{F}_1$  and  $\mathcal{F}_2$  at the nodes  $\mathbf{p}_i$  and  $\mathbf{p}_j$ .

For clarity of description, in this section we assume that  $\mathcal{F}_1$  and  $\mathcal{F}_2$  are point fingers,

and  $\mathbf{p}_i$  and  $\mathbf{p}_j$  will always stay as the only contact points during a grasp operation by the fingers as if it is glued with the object.

**Theorem 3.3.1.** *Suppose  $m \geq 2$ . The following statements hold for the submatrices of  $M$  and  $M^{-1}$ .*

(1)  $\text{rank}(B) = 3$ .

(2)  $C$  is symmetric and positive semi-definite such that  $\text{null}(C) = \text{col}(B)$ . This implies that the  $2m$ -dimensional space is a direct sum of the column spaces of  $C$  and  $B$ :

$$\mathbb{R}^{2m} = \text{col}(C) \oplus \text{col}(B). \quad (3.12)$$

(3)  $\text{rank}(AC) = 2m - 3$  and  $AC$  has only one eigenvalue 1 (of multiplicity  $2m - 3$ ).

(4)  $\mathbb{R}^{2m} = \text{col}(AC) \oplus \text{col}(E)$ .

For stability reason we want to determine the direction under the same amount of squeeze that minimizes the potential energy

$$\Pi = U - \boldsymbol{\delta}^T \mathbf{f} = U - \bar{\boldsymbol{\delta}}^T \bar{\mathbf{f}} = -\frac{1}{2} \bar{\boldsymbol{\delta}}^T C \bar{\boldsymbol{\delta}}. \quad (3.13)$$

by equations (3.10) and (3.11). Because  $m = 2$ ,  $\text{rank}(C) = 4 - \text{rank}(B) = 1$  following Theorem 3.3.1. It is clear that  $\Pi$  is minimized by a unit vector orthogonal to  $\text{col}(B)$ . We can easily show that

$$\hat{\mathbf{u}} = \frac{1}{\sqrt{2} \|\mathbf{p}_i - \mathbf{p}_j\|} \begin{pmatrix} \mathbf{p}_j - \mathbf{p}_i \\ \mathbf{p}_i - \mathbf{p}_j \end{pmatrix} \quad (3.14)$$

is such a unit vector. Indeed, it is the only one corresponding to a grasp because  $-\hat{\mathbf{u}}$  pulls at the contacts.

**Theorem 3.3.2.**  $\hat{\mathbf{u}}$  is orthogonal to  $\text{null}(C)$ . Moreover,

$$C = \frac{1}{\hat{\mathbf{u}}^T A \hat{\mathbf{u}}} \hat{\mathbf{u}} \hat{\mathbf{u}}^T. \quad (3.15)$$



We refer to a movement of  $\mathcal{F}_1$  and  $\mathcal{F}_2$  specified by  $\bar{\boldsymbol{\delta}} = \rho \hat{\boldsymbol{u}}, \rho > 0$ , as a *stable squeeze*, so called because it minimizes the system's potential energy among all squeezes of magnitude  $\rho$ . Substituting  $\hat{\boldsymbol{\delta}} = \rho \hat{\boldsymbol{u}}$  and (3.15) into (3.11), we obtain the strain energy

$$U_s = \rho^2 / (2\hat{\boldsymbol{u}}^T A \hat{\boldsymbol{u}}). \quad (3.16)$$

### 3.4 Pure Squeeze

A stable squeeze is good since it minimize the potential energy. However, it does not guarantee that the resulting displacement field has no rigid body motion component. Since linear elasticity cannot describe large rotation, sometimes we would like to avoid rotation. That is why we introduce pure squeeze which yields no rigid body motion. This is equivalent to  $E^T \bar{\boldsymbol{\delta}} = 0$  as we can establish using (3.10). By Theorem 3.3.1, the set  $\text{col}(AC)$  includes all pure squeezes. Since  $AC = A\hat{\boldsymbol{u}}\hat{\boldsymbol{u}}^T / (\hat{\boldsymbol{u}}^T A \hat{\boldsymbol{u}})$  following Theorem 3.3.2, we can infer that  $\text{col}(AC)$  is spanned by  $A\hat{\boldsymbol{u}}$ . Let  $\hat{\boldsymbol{v}} = A\hat{\boldsymbol{u}} / \|A\hat{\boldsymbol{u}}\|$ . The squeeze  $\hat{\boldsymbol{v}}$  can be viewed as what is left from the squeeze  $\hat{\boldsymbol{u}}$  after stripping off its component that is responsible for rigid body movement. For a pure squeeze specified by  $\rho \hat{\boldsymbol{v}}, \rho > 0$ , we derive the resulting strain energy

$$U_p = \rho^2 \hat{\boldsymbol{u}}^T A \hat{\boldsymbol{u}} / (2\hat{\boldsymbol{u}}^T A A \hat{\boldsymbol{u}}). \quad (3.17)$$

While a stable squeeze makes sure that the movements of the two fingers do not contain any rigid body motion, a pure squeeze makes sure that the object deforms without rigid body motion component. Figure 3.2 compares the effects of the unit stable squeeze  $\hat{\boldsymbol{u}}$  and the unit pure squeeze  $\hat{\boldsymbol{v}}$  on an object. While under  $\hat{\boldsymbol{u}}$  the fingers drive the two contact points toward each other, under  $\hat{\boldsymbol{v}}$  they bend the object to prevent any Euclidean motion, in a “smart” way by exerting smaller contact forces.

Since translating two fingers  $\mathcal{F}_1$  and  $\mathcal{F}_2$  by  $\boldsymbol{\delta}_i$  and  $\boldsymbol{\delta}_j$ , respectively, is equivalent to fixing one finger, say  $\mathcal{F}_1$ , while translating  $\mathcal{F}_2$  by  $\boldsymbol{\delta}_j - \boldsymbol{\delta}_i$  the two resulting configurations are identical except for a translation by  $\boldsymbol{\delta}_i$ . Thus, we consider a squeeze as

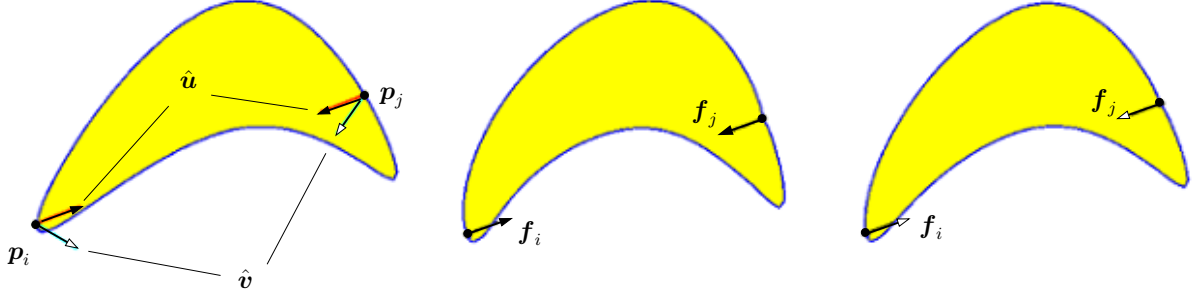


Figure 3.2 Comparison between unit stable and pure squeezes: (a) original shape shown with a stable squeeze  $\hat{u} = (0.65923, 0.25577, -0.65923, -0.25577)^T$  in brown and a pure squeeze  $\hat{v} = (0.79644, -0.49167, -0.20702, -0.28477)^T$  in green; (b) deformed shape under  $\hat{u}$  with resulting contact forces  $f_i = (0.90772, 0.35218)^T$  and  $f_j = (0.90772, 0.35218)^T$ ; (c) deformed shape under  $\hat{v}$  with  $f_i = (0.55243, 0.21433)^T$  and  $f_j = (-0.55243, -0.21433)^T$ .

stable(respectively, pure) if it is the same as  $\rho\hat{u}$ (respectively,  $\rho\hat{v}$ ) up to translation and rotation.

### 3.5 Resisting an Adversary Finger

Consider a finger placement  $\mathcal{G}(p_i, p_j)$  on a deformable object. Now that an adversary finger  $\mathcal{A}$  comes in, makes contact with the object at  $p_k$ , and tries to break the grasp via a translation  $\mathbf{a}$ . To resist  $\mathcal{A}$ , the two grasping fingers  $\mathcal{F}_1$  and  $\mathcal{F}_2$  translate by  $\mathbf{d}_1$  and  $\mathbf{d}_2$  accordingly, respectively. We would like to find  $\mathbf{d}_1$  and  $\mathbf{d}_2$  that result in the minimum total effort by  $\mathcal{F}_1$  and  $\mathcal{F}_2$  in such resistance. The effort of resistance is best characterized as the total work performed by the two grasping fingers.

The general scenario is depicted in Figure 3.3, in which the finger contacts have evolved from the nodes  $p_i, p_j, p_k$  into segments as  $\mathcal{F}_1, \mathcal{F}_2, \mathcal{A}$  translate. Every contact segment is uniquely represented by a set of nodes on it. Suppose that at one moment during the process,  $\mathcal{F}_1$  makes contact with the set of nodes  $\{\mathbf{p}_t \mid t \in \mathbb{I}\}$ ,  $\mathcal{F}_2$  with  $\{\mathbf{p}_t \mid t \in \mathbb{J}\}$ , and  $\mathcal{A}$  with  $\{\mathbf{p}_t \mid t \in \mathbb{K}\}$ . Some nodes (solid dots in the figure) are sticking on the fingertips, while others (hollow dots) are sliding. We can divide the scenario into

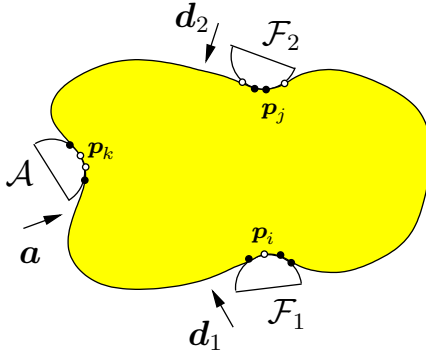


Figure 3.3 Grasp resistance to a translating adversary finger  $\mathcal{A}$ .

small periods, such that within each period the contact index sets  $\mathbb{I}, \mathbb{J}, \mathbb{K}$  do not change.

We will approach this optimization problem in three steps. In Section 4.1, we will look at fixed point contacts (i.e.,  $|\mathbb{I}| = |\mathbb{J}| = |\mathbb{K}| = 1$  and the three sets never change) during the resistance. In Section 4.2, we will generalize the result to fixed segment contacts ( $|\mathbb{I}| = |\mathbb{J}| = |\mathbb{K}| \geq 1$  and the sets do not vary). Based on this we will tackle the general situation with varying  $\mathbb{I}, \mathbb{J}, \mathbb{K}$  and changing contact modes at individual nodes during the resistance under Coulomb friction in Section 4.3.

### 3.5.1 Fixed Point Contacts

The nodes  $\mathbf{p}_i, \mathbf{p}_j$ , and  $\mathbf{p}_k$  will stay as the only contact points with the fingers  $\mathcal{F}_1, \mathcal{F}_2$ , and  $\mathcal{A}$ , respectively (as if the fingers and the object were glued together). Deformation of the object is due to their displacements

$$\bar{\boldsymbol{\delta}} = \begin{pmatrix} \boldsymbol{\delta}_i \\ \boldsymbol{\delta}_j \\ \boldsymbol{\delta}_k \end{pmatrix} = \begin{pmatrix} \mathbf{d}_i \\ \mathbf{d}_j \\ \mathbf{a} \end{pmatrix}. \quad (3.18)$$

By (3.10) the work done by  $\mathcal{F}_1$  and  $\mathcal{F}_2$  is

$$W_{\mathcal{F}} = \frac{1}{2} \begin{pmatrix} \mathbf{d}_1 \\ \mathbf{d}_2 \\ 0 \end{pmatrix}^T \bar{\mathbf{f}} = \frac{1}{2} \begin{pmatrix} \mathbf{d}_1 \\ \mathbf{d}_2 \\ 0 \end{pmatrix}^T C \begin{pmatrix} \mathbf{d}_1 \\ \mathbf{d}_2 \\ \mathbf{a} \end{pmatrix}. \quad (3.19)$$

Similarly, for the three point fingers we call  $\bar{\boldsymbol{\delta}}$  a *stable resistance* if  $\bar{\boldsymbol{\delta}} \in \text{col}(C)$ , and a *pure resistance* if  $\bar{\boldsymbol{\delta}} \in \text{col}(AC)$ . Since  $m = 3$ , both  $\text{col}(C)$  and  $\text{col}(AC)$  have three dimensions by Theorem 3.3.1.

### 3.5.1.1 Optimal Stable Resistance

Consider all  $\mathbf{d}_1$  and  $\mathbf{d}_2$  such that  $\bar{\boldsymbol{\delta}} \in \text{col}(C)$ , or equivalently,  $\bar{\boldsymbol{\delta}} \perp \text{col}(B)$ , which is spanned by  $(1, 0, 1, 0, 1, 0)^T$ ,  $(0, 1, 0, 1, 0, 1)^T$ , and  $(-y_i, x_i, -y_j, x_j, -y_k, x_k)^T$ . Equivalently, we require

$$\mathbf{d}_1 + \mathbf{d}_2 + \mathbf{a} = \mathbf{0}, \quad (3.20)$$

$$\mathbf{p}_i \times \mathbf{d}_1 + \mathbf{p}_j \times \mathbf{d}_2 + \mathbf{p}_k \times \mathbf{a} = \mathbf{0}, \quad (3.21)$$

Substitute (3.20) into (3.19) for  $\mathbf{d}_2$ , and rewrite  $W_{\mathcal{F}}$  as a quadratic form in terms of  $\mathbf{d}_1$ :

$$W_{\mathcal{F}} = \frac{1}{2} \mathbf{d}_1^T H \mathbf{d}_1 + \mathbf{c}^T \mathbf{d}_1 + \omega, \quad (3.22)$$

where  $H$ ,  $\mathbf{c}$ , and  $\omega$  are constant matrix and vectors depending on  $\mathbf{a}$  and  $C$ . It is easy to show that  $H$  is positive semi-definite.

Denote by  $\hat{\mathbf{t}}$  the unit vector in the direction of  $\mathbf{p}_i - \mathbf{p}_j$ , and  $\hat{\mathbf{n}}$  the unit vector such that  $\hat{\mathbf{t}} \cdot \hat{\mathbf{n}} = 0$  and  $\hat{\mathbf{t}} \times \hat{\mathbf{n}} = 1$ . Write  $\mathbf{d}_1 = \tau \hat{\mathbf{t}} + \eta \hat{\mathbf{n}}$ . Substituting it and (3.20) into (3.21), we obtain

$$\eta = \mathbf{d} \cdot \hat{\mathbf{n}} = (\mathbf{p}_j - \mathbf{p}_k) \times \mathbf{a} / \|\mathbf{p}_i - \mathbf{p}_j\|. \quad (3.23)$$

Now, plug  $\mathbf{d}_1 = \tau \hat{\mathbf{t}} + \eta \hat{\mathbf{n}}$  into (3.21). After a few steps, we have a new form for the work:

$$W_{\mathcal{F}} = \frac{1}{2} b_2 \tau^2 + b_1 \tau + b_0, \quad (3.24)$$

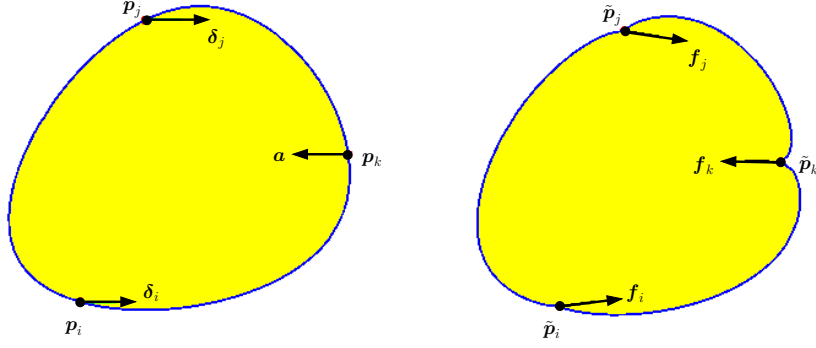


Figure 3.4 A grasp  $\mathcal{G}(\mathbf{p}_i, \mathbf{p}_j)$  resisting an adversary finger at  $\mathbf{p}_k = (0.05900, 0.00502)^T$  under translation  $\boldsymbol{\delta}_k = \mathbf{a} = (-0.01, 0)^T$ , where  $\mathbf{p}_i = (-0.03537, -0.04685)^T$  and  $\mathbf{p}_j = (-0.01256, 0.05212)^T$ : (a) undeformed shape marked with optimal displacements:  $\boldsymbol{\delta}_i = (0.00475, 0.00006)^T$  and  $\boldsymbol{\delta}_j = (0.00525, -0.00006)^T$ ; and (b) deformed shape marked with the corresponding nodal forces:  $\mathbf{f}_i = (2.5031, 0.3105)^T$ ,  $\mathbf{f}_j = (2.8792, -0.4901)^T$ , and  $\mathbf{f}_k = (-5.3823, 0.1796)^T$ .

where  $b_0 = \omega + \eta(\frac{1}{2}\eta\hat{\mathbf{n}}^T H + \mathbf{c}^T)$ ,  $b_1 = (\eta\hat{\mathbf{n}}^T H + \mathbf{c}^T)\hat{\mathbf{t}}$ , and  $b_2 = \hat{\mathbf{t}}^T H \hat{\mathbf{t}}$ . The positive semi-definiteness of  $H$  implies that  $b_2 > 0$ . Therefore,  $W_{\mathcal{F}}$  is a parabola with the minimum value  $W_{\mathcal{F}}^* = b_0 - \frac{b_1^2}{2b_2}$  achieved at  $\tau = -b_1/b_2$ . Note that  $b_0$  scales with  $\|a\|^2$  and  $b_1$  scales with  $\|a\|$ , while  $b_2$  is constant. The minimum work  $W_{\mathcal{F}}^*$  scales quadratically with  $\|a\|$ .

Figure 3.4 shows a resistance scenario. The minimum work is  $W_{\mathcal{F}}^* = 0.01031$ . The average rotation per node is  $\boldsymbol{\delta} \cdot \mathbf{v}_{2n} = 0.0035418$ .

### 3.5.1.2 Optimal Pure Resistance

In this section we find a pure resistance that minimizes  $W_{\mathcal{F}}$ , considering only  $\mathbf{d}_1$  and  $\mathbf{d}_2$  such that  $\bar{\boldsymbol{\delta}} \in \text{col}(AC)$ . Represent  $\bar{\boldsymbol{\delta}} = \tau_1 \hat{\mathbf{u}}_1 + \tau_2 \hat{\mathbf{u}}_2 + \tau_3 \hat{\mathbf{u}}_3$ , where  $\hat{\mathbf{u}}_1, \hat{\mathbf{u}}_2, \hat{\mathbf{u}}_3$  are the orthogonal unit vectors that span  $\text{col}(AC)$ . From these two equivalent representations of  $\bar{\boldsymbol{\delta}}$ , we infer that

$$\mathbf{a} = Q \begin{pmatrix} \tau_1 \\ \tau_2 \\ \tau_3 \end{pmatrix}, \quad (3.25)$$

where the  $2 \times 3$  matrix  $Q = (\mathbf{0}, I_2)(\hat{\mathbf{u}}_1, \hat{\mathbf{u}}_2, \hat{\mathbf{u}}_3)$ .

If  $Q$  is not of full rank and  $\mathbf{a}$  is not in its column space, then we infer that  $\bar{\boldsymbol{\delta}} \in \text{col}(AC)$  and the adversary finger cannot be resisted.

In the general case  $\text{rank}(Q) = 2$ ,  $\tau_2$  and  $\tau_3$  are linear in  $\tau_1$ , yielding  $W_{\mathcal{F}}$  as a quadratic function of  $\tau_1$ . The optimal grasping finger displacements can be obtained from  $dW_{\mathcal{F}}/d\tau_1 = 0$ . This solution also works for  $\text{rank}(Q) = 1$  and  $\mathbf{a} \in \text{col}(Q)$ , after proper permutation of  $\tau_1, \tau_2, \tau_3$  to set the latter two to zero.

### 3.5.2 Fixed Segment Contacts

In this section, the contact index sets  $\mathbb{I}, \mathbb{J}, \mathbb{K}$  may have sizes greater than one, but still they will not change during the resistance. In other words, no existing contacts will break and no new contacts will come in. All the nodes in contact with the same finger undergo the same displacement. More specifically, a contact node  $\mathbf{p}_t$  is displaced by

$$\boldsymbol{\delta}_t = \begin{cases} \mathbf{d}_1, & \text{if } t \in \mathbb{I}; \\ \mathbf{d}_2, & \text{if } t \in \mathbb{J}; \\ \mathbf{a}, & \text{if } t \in \mathbb{K}. \end{cases} \quad (3.26)$$

Rearrange the rows and columns of the reduced stiffness matrix in the same index order as in  $\bar{\boldsymbol{\delta}}$ .

Again, we first consider stable resistances, for which the following generalizations of (3.20) and (3.21) hold:

$$\sum_{t \in \mathbb{I} \cup \mathbb{J} \cup \mathbb{K}} \boldsymbol{\delta}_t = \mathbf{0} \quad \text{and} \quad \sum_{t \in \mathbb{I} \cup \mathbb{J} \cup \mathbb{K}} \mathbf{p}_t \times \boldsymbol{\delta}_t = \mathbf{0}. \quad (3.27)$$

The first condition above yields  $\mathbf{d}_2$  in terms of  $\mathbf{d}_1$  and  $\mathbf{a}$ . Substitute it into the second condition to yield

$$|\mathbb{I}|(\check{\mathbf{p}} - \check{\mathbf{q}}) \times \mathbf{d}_1 + |\mathbb{K}|(\check{\mathbf{r}} - \check{\mathbf{q}}) \times \mathbf{a} = \mathbf{0}, \quad (3.28)$$

where  $\check{\mathbf{p}} = \frac{1}{|\mathbb{I}|} \sum_{t \in \mathbb{I}} \mathbf{p}_t$ ,  $\check{\mathbf{q}} = \frac{1}{|\mathbb{J}|} \sum_{t \in \mathbb{J}} \mathbf{p}_t$ , and  $\check{\mathbf{r}} = \frac{1}{|\mathbb{K}|} \sum_{t \in \mathbb{K}} \mathbf{p}_t$  are referred to as the *contact centroids* of the fingers  $\mathcal{F}_1, \mathcal{F}_2, \mathcal{A}$ , respectively.

$\mathcal{F}_1$  and  $\mathcal{F}_2$  into the form of (3.22), where  $H$ ,  $\mathbf{c}$ , and  $\omega$  assume new expressions. Minimization parallels that in Section 4.1 with a decomposition of  $\mathbf{d}_1$  along the direction  $\hat{\mathbf{t}}$  of  $\check{\mathbf{p}} - \check{\mathbf{q}}$ , and its orthogonal direction  $\hat{\mathbf{n}}$ .

The case of a pure resistance with fixed segment contacts also generalizes that of fixed point contacts in Section 4.1. We will end up with a very similar optimization problem. Aside from a different form of  $W_{\mathcal{F}}$  and different variables  $\tau'_1, \tau'_2, \tau'_3$ , over which the constraint is  $\mathbf{a} = (\mathbf{0}, I_2)(\hat{\mathbf{u}}'_1, \hat{\mathbf{u}}'_2, \hat{\mathbf{u}}'_3)(\tau'_1, \tau'_2, \tau'_3)^T$ .

### 3.5.3 Frictional Segment Contacts

We are now ready to consider optimal resistance with varying segment contacts under friction. The two grasping fingers and the adversary finger have semicircular fingertips with possibly different radii. In a realistic scenario, the grasping fingers  $\mathcal{F}_1$  and  $\mathcal{F}_2$  first perform a squeeze on the object by translating toward each other via  $s(\mathbf{p}_j - \mathbf{p}_i)$  and  $s(\mathbf{p}_i - \mathbf{p}_j)$ , for some  $s > 0$ , which is called the *pre-grasp*. Then the adversary finger  $\mathcal{A}$  makes contact at the node  $\mathbf{p}_k$  and exerts a translation  $\mathbf{a}$  to try to break the grasp. The system configuration right before this disturbance, including the object's deformed shape and the contact index sets  $\mathbb{I}$  and  $\mathbb{J}$  for  $\mathcal{F}_1$  and  $\mathcal{F}_2$ , can be determined by the event-driven squeeze grasping algorithm from (15).

The translation distance by the adversary finger  $\mathcal{A}$  will be sequenced into  $a_0 = 0 < a_1 < \dots < a_l < \dots < |\mathbf{a}|$  such that at every  $a_l$ , one of the four contact events A, B, C, and D described in (15) takes place.

Consider the moment when  $\mathcal{A}$  has translated by the distance  $a_l$ . For a contact node  $\mathbf{p}_t$  we use  $\delta_t^{(l)}$ ,  $\mathbf{f}_t^{(l)}$ , and  $\theta_t^{(l)}$  to refer to its displacement, contact force, and polar angle with respect to the center of its contacting fingertip.

Next,  $\mathcal{A}$  will continue moving by an extra distance  $\xi$  in the direction of  $\mathbf{a}$ . Suppose that  $\xi$  is small enough such that all contacts and their modes will not change. We determine the extra translations  $\mathbf{d}'_1$  of  $\mathcal{F}_1$  and  $\mathbf{d}'_2$  of  $\mathcal{F}_2$  to resist this extra movement by

$\mathcal{A}$ , via minimizing the extra work performed by these two fingers:

$$W'_{\mathcal{F}} = \sum_{t \in \mathbb{I} \cup \mathbb{J}} \delta'_t \mathbf{f}_t^{(l)} + \frac{1}{2} \sum_{t \in \mathbb{I} \cup \mathbb{J}} \delta'_t \mathbf{f}'_t \quad (3.29)$$

In the above, for  $t \in \mathbb{I} \cup \mathbb{J}$ ,  $\delta'_t$  is the change in the displacement of the contact node  $\mathbf{p}_t$  from  $\delta_t^{(l)}$ , and  $\mathbf{f}'_t$  the change in its contact force from  $\mathbf{f}_t^{(l)}$ .

During this extra translation period, if a node  $\mathbf{p}_t$ ,  $t \in \mathbb{I} \cup \mathbb{J}$ , sticks, then  $\delta'_t = \mathbf{d}'_1$  or  $\mathbf{d}'_2$ . If it slides, then  $\delta'_t$  will be the sum of  $\mathbf{d}'_1$  or  $\mathbf{d}'_2$  and the node's movement  $r \begin{pmatrix} \cos \theta_t - \cos \theta_t^{(l)} \\ \sin \theta_t - \sin \theta_t^{(l)} \end{pmatrix}$ , on the tip of  $\mathcal{F}_1$  or  $\mathcal{F}_2$  that it is in contact with. Minimization of  $W'_{\mathcal{F}}$  would be over  $\delta'_1$  and  $\delta'_2$ , and the polar angle  $\theta_t$  of every sliding contact  $\mathbf{p}_t$ . It could get too inefficient.

We stipulate that the work performed on  $\mathbf{p}_t$ ,  $t \in \mathbb{I} \cup \mathbb{J}$ , due to its sliding, by the contacting finger  $\mathcal{F}_1$  or  $\mathcal{F}_2$  will be significantly less than the amount due to its translation with the finger. Instead of minimizing  $W'_{\mathcal{F}}$ , we minimize its approximation  $\tilde{W}'_{\mathcal{F}}$  by treating every sliding node in contact with  $\mathcal{F}_1$ ,  $\mathcal{F}_2$ , or  $\mathcal{A}$  as if it would be sticking during the period of the extra resistance period.

In short, whether a contact node  $\mathbf{p}_t$  sticks or slips, its extra displacement  $\delta'_t$  will be set as follows:

$$\delta'_t = \begin{cases} \mathbf{d}'_1, & \text{if } t \in \mathbb{I}; \\ \mathbf{d}'_2, & \text{if } t \in \mathbb{J}; \\ \xi \hat{\mathbf{a}}, & \text{if } t \in \mathbb{K}. \end{cases} \quad (3.30)$$

Then  $\mathbf{d}'_1 = \xi \boldsymbol{\psi}_1$  and  $\mathbf{d}'_2 = \xi \boldsymbol{\psi}_2$ , where  $\boldsymbol{\psi}_1$  and  $\boldsymbol{\psi}_2$  are determined like  $\mathbf{d}_1$  and  $\mathbf{d}_2$  in Section 4.2 with  $\hat{\mathbf{a}}$  replacing  $\mathbf{a}$ .

We determine the extra distance  $\xi$  by which  $\mathcal{A}$  translates until the next contact event happens, by using the event-driven algorithm proposed in (15). Once an event occurs, the overall translation distance for  $\mathcal{A}$  is updated as  $a_{l+1} = a_l + \xi$ . In addition to the index sets  $\mathbb{I}$ ,  $\mathbb{J}$ ,  $\mathbb{K}$ , update the set  $\mathbb{P}$  of sliding contacts and the set  $\mathbb{T}$  of sticking contacts. If the adversary finger  $\mathcal{A}$  begins to slip after an event, it has been successfully resisted. If



either  $\mathcal{F}_1$  or  $\mathcal{F}_2$  starts to slide, the grasp fails to resist  $\mathcal{A}$ . If none of the above two cases happens,  $\mathcal{A}$  will complete its translation  $\mathbf{a}$  while being resisted. Algorithm 1 summarizes how  $\mathcal{F}_1$  and  $\mathcal{F}_2$  resist  $\mathcal{A}$ .

---

**Algorithm 1** Resisting a Translating Adversary Finger under Frictional Segment Contact

---

**Input:** contact index sets  $\mathbb{I}, \mathbb{J}, \mathbb{K}$  for  $\mathcal{F}_1, \mathcal{F}_2, \mathcal{A}$ , translation  $a$  of  $\mathcal{F}_2$

---

- 1:  $a \leftarrow 0$
  - 2: let  $\mathbb{I}, \mathbb{J}, \mathbb{K}$  contain the indices of the initial point contacts with  $\mathcal{F}_1, \mathcal{F}_2, \mathcal{A}$ , respectively
  - 3: initialize  $\mathbb{T}$  and  $\mathbb{P}$
  - 4: **while**  $a < \|\mathbf{a}\|$  and no finger slips **do**
  - 5:     construct the form of  $\tilde{W}'_{\mathcal{F}}$  based on (3.29), (3.30), and  $\mathbb{I}, \mathbb{J}, \mathbb{K}$
  - 6:     minimize  $\tilde{W}'_{\mathcal{F}}$  to obtain  $\psi_1$  and  $\psi_2$  as the translations of  $\mathcal{F}_1$  and  $\mathcal{F}_2$  in response to a (hypothesized) unit translation  $a/\|\mathbf{a}\|$  by  $\mathcal{A}$
  - 7:     execute the event-driven algorithm in (15) along the displacement directions computed in step 6 until the next contact event occurs
  - 8:     compute the actual work  $W'_{\mathcal{F}}$
  - 9:      $W_{\mathcal{F}} \leftarrow W_{\mathcal{F}} + W'_{\mathcal{F}}$
  - 10:    update  $\mathbb{I}, \mathbb{J}, \mathbb{K}, \mathbb{T}, \mathbb{P}$  according to the contact event
  - 11:    update the contact force  $\mathbf{f}_t, \forall t \in \mathbb{I} \cup \mathbb{J} \cup \mathbb{K}$
  - 12: **end while**
  - 13: **if**  $a < \|\mathbf{a}\|$  and ( $\mathcal{F}_1$  or  $\mathcal{F}_2$  slips) **then**
  - 14:     **return** failure
  - 15: **else**
  - 16:     **return**  $W_{\mathcal{F}}$
  - 17: **end if**
-

Table 3.1 Forces exerted and work performed by the the two grasping fingers in Figure 3.5 under translations  $\mathbf{d}_1$ ,  $\mathbf{d}_2$ , and  $\mathbf{a}$ .

	$\mathcal{F}_1$	$\mathcal{F}_2$
force(start)	2.098	-2.566
force(end)	8.136	-1.23
work	0.0101	-0.0015

### 3.5.4 Simulation and Experiment on Grasp Resistance

Figure 3.5(a) shows an object with convex shape grasped under a stable squeeze by  $\mathcal{F}_1$  (translating via  $(0.00068, 0.002)^T$  from  $p_i$  to  $p_j$ ) and  $\mathcal{F}_2$  (motionless). Then, an adversary finger  $\mathcal{A}$  starts pushing the object through translation  $\mathbf{a} = (0.0024, 0.0044)^T$ , as shown in (b). All three fingertips have radius 0.02. Algorithm 1 generates two trajectories for  $\mathcal{F}_1$  and  $\mathcal{F}_2$  for a stable squeeze shown in (c). They have total displacements  $\mathbf{d}_1 = (-0.0008, -0.0019)^T$  and  $\mathbf{d}_2 = (-0.0007, -0.0005)^T$ . Table 3.1 displays the components of the finger forces exerted along the translation directions, at the start and the end of resistance, and the work performed by the fingers. A negative force reading on  $\mathcal{F}_2$  indicates that the contact force influenced by friction was pulling away from the translation direction of the finger. Contact events A, B, C, D occurred 7, 0, 3, and 2 times, respectively, during the resistance. The coefficient of contact friction is 0.4.

Shown in Figure 3.6(a) is an experiment to validate the results in Table 3.1 from the instance in Figure 3.5. The object with exactly the same shape in Figure 3.5 was placed on a raised platform. The grasping fingertips  $\mathcal{F}_1$  and  $\mathcal{F}_2$  were respectively controlled by an Adept Cobra 600 manipulator and the Barrett Hand. As shown in (b),  $\mathcal{F}_1$  was attached to a force meter from Ametek Hunter Spring, which was connected to the Adept's open end via an adapter. The manipulator has an accuracy of 0.02mm in any horizontal direction. Since none of the three fingers of the Barrett Hand could be controlled to perform straight line motions, we let its middle finger push fingertip  $\mathcal{F}_2$

via a linear mechanism, which is shown in (c) in both top-down and side views. The mechanism was an aluminum cylindrical stick constrained by ball bearings embedded inside two boxes. At its one end was a disk to be pushed by the finger of the Barrett Hand or human hand. Near its other end, a force meter was attached underneath. The tip  $\mathcal{F}_2$  was mounted at the front of the force meter, which would be able to measure the force exerted by the tip once it made contact with the object.

The human hand pushed the adversary fingertip  $\mathcal{A}$  via another linear mechanism identical to the one driving  $\mathcal{F}_2$ . No force meter was attached to this pusher. A ruler was mounted on the tops of the two ball bearing boxes to measure the travel distance by  $\mathcal{A}$ . The translations by  $\mathcal{F}_1$  and  $\mathcal{F}_2$ , meanwhile, were precisely controlled by the Adept and the Barrett Hand. The fingers  $\mathcal{F}_1$  and  $\mathcal{F}_2$  first made contact with a foam object. To repeat the simulation instance in the above,  $\mathcal{F}_2$  stayed still and  $\mathcal{F}_1$  squeezed the object via a translation  $(-0.00068, 0.002)^T$  along the line through their initial contact points with the object. The configuration after the squeeze is shown in Figure 3.7(a). Afterward, the human hand pushed  $\mathcal{A}$  via the linear mechanism to complete a translation  $\mathbf{a} = (0.0024, 0.0044)^T$ . Algorithm 1 generated two trajectories shown in Figure 3.5(c) respectively for  $\mathcal{F}_1$  and  $\mathcal{F}_2$  based on stable squeezes. For ease of control, each trajectory was straightened by connecting its starting location to its final location, yielding translations  $\mathbf{d}_1 = (-0.0008, -0.0019)^T$  and  $\mathbf{d}_2 = (-0.0007, -0.0005)^T$  (see the dashed lines in Figure 3.5(c)). The human hand executed the push  $\mathbf{a}$ , which was simultaneously being resisted by the Adept arm and the Barrett hand via translations  $\mathbf{d}_1$  and  $\mathbf{d}_2$ , respectively.

We refer to the resistance specified by  $\mathbf{d}_1$  and  $\mathbf{d}_2$  as the “optimal” resistance. The work done by  $\mathcal{F}_1$  or  $\mathcal{F}_2$  was estimated as half the product of the translation distance with the summation of the initial and final force readings for each finger. Columns 2 and 3 in Table 3.2 displayed the force readings on these two grasping fingers at the start and the end of the resistance, and the work they performed. We can see that small discrepancies

Table 3.2 Forces exerted and work performed by  $\mathcal{F}_1$  and  $\mathcal{F}_2$  in Figure 3.7 under  $\mathbf{d}_1$  and  $\mathbf{d}_2$  computed by the resistance algorithm (columns 23) or arbitrarily chosen (columns 45).

	“optimal” resist.		“arbitrary” resist.	
	$\mathcal{F}_1$	$\mathcal{F}_2$	$\mathcal{F}_1$	$\mathcal{F}_2$
force(start)	2.22	-2.67	7.05	4.20
force(end)	8.06	-1.45	14.86	13.93
work	0.0107	-0.0017	0.0463	0.0328

exist compared to Table 3.1. They were mainly due to the trajectory straightening and measurement errors in the experiment. For comparison, we also tested an “arbitrary” resistance strategy against the same adversary finger disturbance. We arbitrarily chose a translation direction  $\mathbf{d}_2/\|\mathbf{d}_2\| = (0.447, -0.894)^T$  for  $\mathcal{F}_2$ . Then  $\mathbf{d}_1 = (-0.004, -0.0012)^T$  and  $\mathbf{d}_2 = (0.0016, -0.0032)^T$  were determined from the condition  $(\mathbf{d}_1^T, \mathbf{d}_2^T, \mathbf{a}^T)^T \perp \text{col}(B)$  for a stable squeeze. The experimental result was included in Table 3.2. It can be seen that much less work was carried out by  $\mathcal{F}_1$  and  $\mathcal{F}_2$  under the optimal resistance strategy.

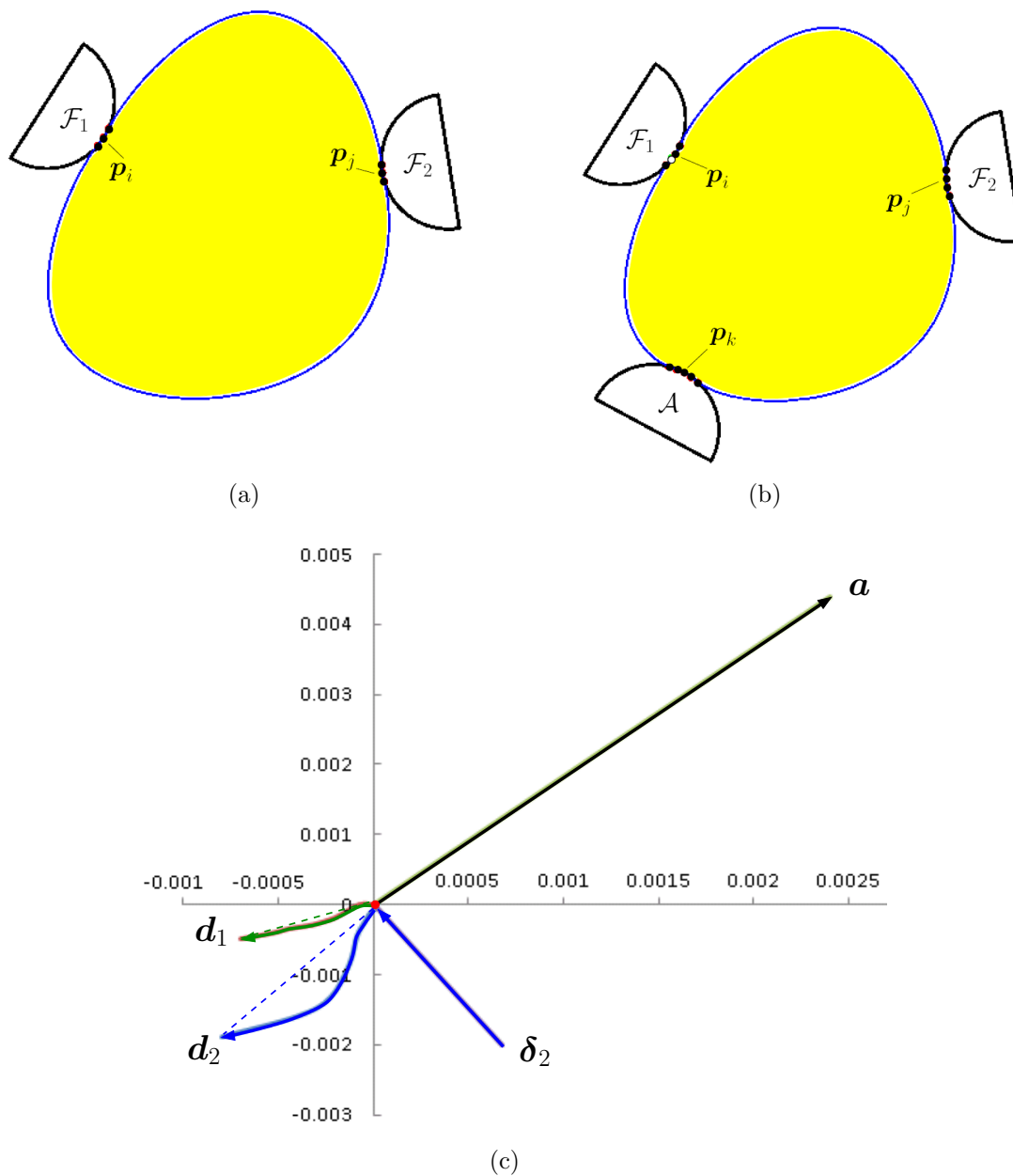


Figure 3.5 Resisting an adversary semicircular fingertip under friction: (a) A convex shape grasped via a stable squeeze. (b) Successful resistance to an adversary finger  $\mathcal{A}$ . (c) Trajectories of the three fingers during the resistance, with their starting points translated to coincide with the origin, which, for display purpose, is also made the ending point of the trajectory  $\delta_1$  of  $\mathcal{F}_1$  in achieving an initial grasp before the resistance.

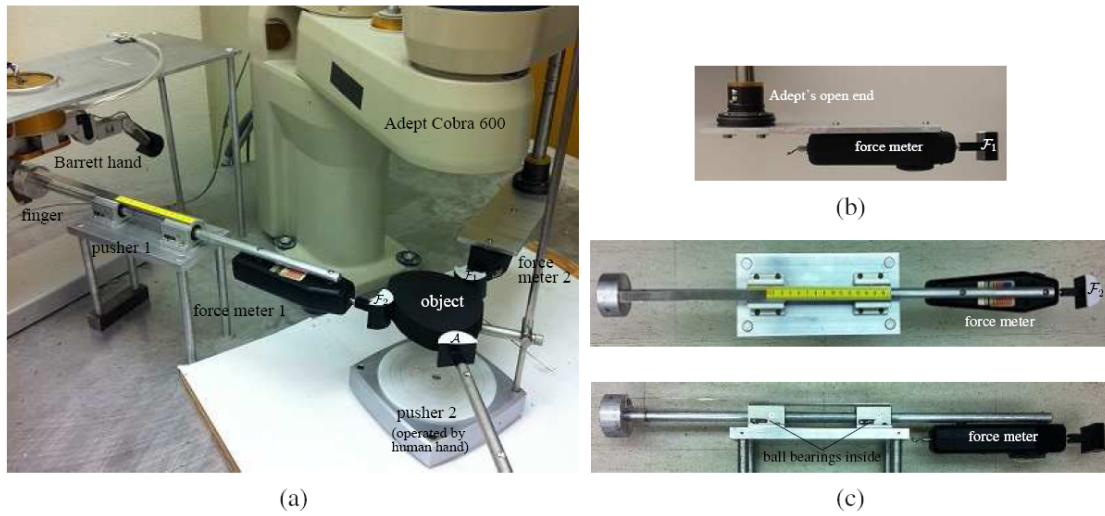


Figure 3.6 Experimental setup for resisting an adversary fingertip  $\mathcal{A}$ : (a) grasping fingertips  $\mathcal{F}_1$  and  $\mathcal{F}_2$  driven by an Adept Cobra 600 manipulator and a finger of the Barrett hand, respectively, and  $\mathcal{A}$  by the human hand; (b)  $\mathcal{F}_1$  attached to a force meter rigidly connected to the Adept's open end via an adapter; (c)  $\mathcal{F}_2$  attached to another force meter rigidly connected to a linear mechanism to be pushed by the Barrett finger.

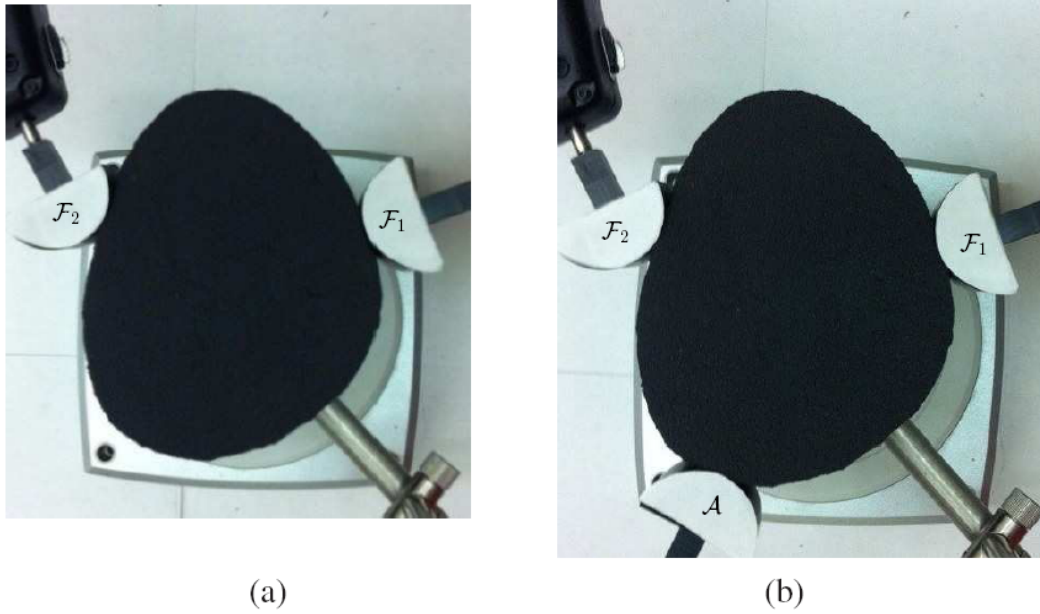


Figure 3.7 Experiment for resisting an adversary finger: (a) Grasp of a convex object and (b) its resistance to an adversary finger  $\mathcal{A}$ . The translation  $\delta_1$  of  $\mathcal{F}_1$  in (a), and the translations  $\mathbf{d}_1$ ,  $\mathbf{d}_2$ , and  $\mathbf{a}$  of  $\mathcal{F}_1, \mathcal{F}_2$  and  $\mathcal{A}$  are drawn in Figure 3.5.

## CHAPTER 4. PICKING UP SOFT 3D OBJECTS

This chapter will start with a brief review of linear elasticity for 3D solids, and the characterization of all displacement fields that represent rigid body movements. It will then describe an FEM formulation of deformation under gravity. We will move on to offer a solution of the deformed shape of a solid object from specified contact displacements. Finally we will propose a strategy to pick up a deformable 3D object with two fingers under resting.

### 4.1 Linear Elasticity

Consider a 3D object under a displacement field  $(u(x, y, z), v(x, y, z), w(x, y, z))^T$ . Every point  $(x, y, z)^T$  inside the object moves to  $(x + u, y + v, z + w)^T$ . Denote by  $\epsilon_x$ ,  $\epsilon_y$ ,  $\epsilon_z$  the normal strains along the  $x$ -,  $y$ -, and  $z$ -directions, respectively, and  $\gamma_{xy}$ ,  $\gamma_{xz}$ ,  $\gamma_{yz}$  the shear strains in the  $xy$ -,  $xz$ -, and  $yz$ -planes, respectively. They are given below:

$$\begin{aligned}
 \epsilon_x &= \frac{\partial u}{\partial x}, \\
 \epsilon_y &= \frac{\partial v}{\partial y}, \\
 \epsilon_z &= \frac{\partial w}{\partial z}, \\
 \gamma_{xy} &= \frac{\partial u}{\partial y} + \frac{\partial v}{\partial x}, \\
 \gamma_{xz} &= \frac{\partial u}{\partial z} + \frac{\partial w}{\partial x}, \\
 \gamma_{yz} &= \frac{\partial w}{\partial y} + \frac{\partial v}{\partial z}.
 \end{aligned} \tag{4.1}$$



The strain energy of the object can be derived:

$$U = \frac{E}{2(1+\nu)} \int_V ((\epsilon_x^2 + \epsilon_y^2 + \epsilon_z^2) + \frac{\nu}{(1-2\nu)} (\epsilon_x + \epsilon_y + \epsilon_z)^2 + \frac{1}{2} (\gamma_{xy}^2 + \gamma_{xz}^2 + \gamma_{yz}^2)) dV. \quad (4.2)$$

where  $E$  and  $\nu$  are Young's modulus and Poisson's ratio of the material, respectively, with  $E > 0$  and  $-1 < \nu < \frac{1}{2}$  for most materials including those considered in our grasping task.

**Theorem 4.1.1.** *Under linear elasticity, any displacement field  $(u, v, w)^T$  that yields zero strain energy is linearly spanned by the following six fields:*

$$\begin{pmatrix} 1 \\ 0 \\ 0 \end{pmatrix}, \begin{pmatrix} 0 \\ 1 \\ 0 \end{pmatrix}, \begin{pmatrix} 0 \\ 0 \\ 1 \end{pmatrix}, \begin{pmatrix} 0 \\ -z \\ y \end{pmatrix}, \begin{pmatrix} z \\ 0 \\ -x \end{pmatrix}, \begin{pmatrix} -y \\ x \\ 0 \end{pmatrix}.$$

The first three displacement fields in the theorem represent unit translations in the  $x$ -,  $y$ -, and  $z$ -directions, respectively. The next three fields represent rotations along the  $x$ -,  $y$ -, and  $z$ -axes, respectively.

## 4.2 The Finite Element Method with Gravity

We represent a solid as a tetrahedral mesh with  $n$  vertices  $\mathbf{p}_1, \dots, \mathbf{p}_n$ , where  $\mathbf{p}_i = (x_i, y_i, z_i)^T$ , for  $1 \leq i \leq n$ .

Similar as in the planar case, we infer from Theorem 4.1.1 that the stiffness matrix has a null space spanned by the following six  $3n$ -vectors:

$$\begin{aligned} \mathbf{t}_x &= (1, 0, 0, 1, 0, \dots, 0)^T, \\ \mathbf{t}_y &= (0, 1, 0, 0, 1, \dots, 0)^T, \\ \mathbf{t}_z &= (0, 0, 1, 0, 0, \dots, 1)^T, \\ \mathbf{r}_x &= (0, -z_1, y_1, 0, -z_2, \dots, y_n)^T, \\ \mathbf{r}_y &= (z_1, 0, x_1, z_2, 0, \dots, -x_n)^T, \\ \mathbf{r}_z &= (-y_1, x_1, 0, -y_2, x_2, \dots, 0)^T. \end{aligned} \quad (4.3)$$

On 3D grasping, the gravitational force can rarely be ignored since it plays an important role during the deformation. Assume that the mass is uniformly distributed inside the body. Thus every element has mass proportional to its volume. We assign the element's mass evenly to its four vertices. Thus the total gravitational force exerted on a vertex  $\mathbf{p}_i$ ,  $1 \leq i \leq n$ , sums up a quarter of the gravitational force on each tetrahedron it is incident on. Write all nodal gravitation forces into a vector  $\mathbf{G}$ . It is straightforward to verify that  $\mathbf{G}$  is orthogonal to all the six vectors spanning the null space except  $\mathbf{t}_z$ , with which it has a dot product  $-mg$ , where  $m$  is the object's mass and  $g = 9.8$  is the gravitational acceleration.

The potential energy of the system can be represented as

$$\Pi = \frac{1}{2} \mathbf{\Delta}^T K \mathbf{\Delta} - \mathbf{\Delta}^T (\mathbf{F} + \mathbf{G}). \quad (4.4)$$

At equilibrium, it reaches its minimum value, implying

$$K \mathbf{\Delta}^T = \mathbf{F} + \mathbf{G}. \quad (4.5)$$

The stiffness matrix  $K$  is symmetric and thus diagonalizable. With  $3n$  independent eigenvectors, it is also known to be positive semi-definite. Given its six-dimensional null space,  $K$  has  $3n - 6$  positive eigenvalues  $\lambda_1, \dots, \lambda_{3n-6}$  corresponding to unit eigenvectors  $\mathbf{v}_1, \dots, \mathbf{v}_{3n-6}$ . Let  $\mathbf{v}_{3n-5}, \mathbf{v}_{3n-4}, \mathbf{v}_{3n-3}$  be normalized over  $\mathbf{t}_x, \mathbf{t}_y, \mathbf{t}_z$ , respectively. And let  $\mathbf{v}_{3n-2}, \mathbf{v}_{3n-1}, \mathbf{v}_{3n}$  be orthogonalized over  $\mathbf{r}_x, \mathbf{r}_y, \mathbf{r}_z$  using Gram-Schmidt procedure. Thus,  $\mathbf{G} \cdot \mathbf{v}_{3n-3} = -mg/\sqrt{n}$  while  $\mathbf{G} \cdot \mathbf{v}_j = 0$ ,  $3n - 5 \leq j \leq 3n$  and  $j \neq 3n - 3$ . The matrix has a spectral decomposition  $K = V \Lambda V^T$ , where  $V = (\mathbf{v}_1, \dots, \mathbf{v}_{3n})$  and  $\Lambda = \text{diag}(\lambda_1, \dots, \lambda_{3n-6}, 0, \dots, 0)$ .

Because of the singularity of  $K$ , boundary conditions are required for solution of (4.5). They will come from the displacements of the contact nodes as they move with the squeezing fingers or stay with the supporting plane.

### 4.3 Deformation from Specified Contact Displacements

The set of contact nodes will not vary during a very small period of squeeze on the solid by the fingers. First we need to compute the deformation of the 3D object from specified displacements  $\boldsymbol{\delta}_{i_1}, \dots, \boldsymbol{\delta}_{i_m}$  of some boundary nodes  $\mathbf{p}_{i_1}, \dots, \mathbf{p}_{i_m}$ , which are supposed to be in contact with a grasping finger or the supporting plane. We refer to the set  $\mathbb{C} = \{i_1, \dots, i_m\}$  as the contact index set. Zero external forces are applied at the non-contact nodes, that is,  $\mathbf{f}_k = 0$ , for  $k = 1, \dots, n$  and  $k \notin \mathbb{C}$ .

Denote  $\bar{\boldsymbol{\Delta}} = (\boldsymbol{\delta}_{i_1}^T, \dots, \boldsymbol{\delta}_{i_m}^T)^T$  as before. We can solve for the contact force vector  $\bar{\mathbf{F}}$  and the displacement field  $\boldsymbol{\Delta}$  from  $\bar{\boldsymbol{\Delta}}$  by performing a procedure similar to the one in (15). Substitute  $K = V\Lambda V^T$  into (4.5), and left multiply both sides of the resulting equation with  $V^T$ . This yields

$$\begin{aligned} \boldsymbol{\Delta} &= \sum_{k=1}^{3n-6} \frac{1}{\lambda_k} (\mathbf{v}_k^T (\mathbf{F} + \mathbf{G})) \mathbf{v}_k + (\mathbf{v}_{3n-5}, \dots, \mathbf{v}_{3n}) \mathbf{b} \\ &= \sum_{k=1}^{3n-6} \frac{1}{\lambda_k} (\bar{\mathbf{v}}_k^T \bar{\mathbf{F}}) \mathbf{v}_k + (\mathbf{v}_{3n-5}, \dots, \mathbf{v}_{3n}) \mathbf{b} + \mathbf{D}, \end{aligned} \quad (4.6)$$

where  $\mathbf{D} = \sum_{k=1}^{3n-6} \frac{1}{\lambda_k} (\mathbf{v}_k^T \mathbf{G}) \mathbf{v}_k$  is a constant vector. The  $3m$  equations for  $\boldsymbol{\delta}_{i_1}, \dots, \boldsymbol{\delta}_{i_m}$  are extracted from (4.6), and combined with the six equations  $\mathbf{v}_k^T (\mathbf{F} + \mathbf{G}) = 0$ ,  $k = 3n - 5, \dots, 3n$ . This sets up a linear equation in  $\bar{\mathbf{F}}$  and  $\mathbf{b}$ :

$$M \begin{pmatrix} \bar{\mathbf{F}} \\ \mathbf{b} \end{pmatrix} = \begin{pmatrix} \bar{\boldsymbol{\Delta}} - \bar{\mathbf{D}} \\ (0, 0, mg/\sqrt{n}, 0, 0, 0)^T \end{pmatrix}, \quad (4.7)$$

where

$$M = \begin{pmatrix} A & B \\ B^T & 0 \end{pmatrix}, \quad (4.8)$$

with the  $3m \times 3m$  matrix  $A = \sum_{k=1}^{3n-6} \frac{1}{\lambda_k} \bar{\mathbf{v}}_k \bar{\mathbf{v}}_k^T$  and the  $6 \times 6$  matrix  $B = (\bar{\mathbf{v}}_{3n-5}, \dots, \bar{\mathbf{v}}_{3n})$ .

**Theorem 4.3.1.** *The matrix  $M$  is non-singular if and only if the  $m$  contact points are not collinear.*

Under the above theorem, when the contacts are not collinear, the system (4.7) has a unique solution, in other words, the deformation is uniquely determined. To solve the system, we invert the matrix  $M$  to obtain

$$M^{-1} = \begin{pmatrix} C & E \\ E^T & H \end{pmatrix}, \quad (4.9)$$

where  $C$ ,  $E$ , and  $H$  are matrices of dimensions  $3m \times 3m$ ,  $3m \times 6$ , and  $6 \times 6$ , respectively. Left multiplication of  $M^{-1}$  with both sides of (4.7) yields

$$\begin{aligned} \bar{\mathbf{F}} &= C(\bar{\mathbf{\Delta}} - \bar{\mathbf{D}}) - E(0, 0, mg/\sqrt{n}, 0, 0, 0)^T \\ &= C(\bar{\mathbf{\Delta}} - \bar{\mathbf{D}}) - \frac{mg}{\sqrt{n}} \mathbf{e}_3, \end{aligned} \quad (4.10)$$

where  $\mathbf{e}_3$  is the third column of  $E$ . The equation relates the contact forces to the specified contact displacements. With  $\mathbf{F}$  and  $\mathbf{D}$  determined, the displacement vector follows from (4.7).

#### 4.4 Grasping to Pick up a Solid

Having studied deformation under contacts, we move on to consider the task of using two fingers to pick up a deformable 3D solid on a horizontal plane  $\mathcal{P}$ . The two fingertips  $\mathcal{F}_1$  and  $\mathcal{F}_2$  make initial point contacts with the object at the nodes  $\mathbf{p}_i$  and  $\mathbf{p}_j$ , respectively. The fingers have identical hemispherical tips  $\mathcal{F}_1$  and  $\mathcal{F}_2$  for simplicity. The strategy is described in Algorithm 2.

In the current phase of our work, the fingers are assumed to be translating during the squeeze in constant directions, denoted by unit vectors  $\hat{\mathbf{d}}_1$  and  $\hat{\mathbf{d}}_2$ , respectively. Without loss of generality, let  $\mathcal{F}_1$  be the moving fingertip. For every unit distance  $\mathcal{F}_1$  translates in  $\hat{\mathbf{d}}_1$ ,  $\mathcal{F}_2$  translates in  $\hat{\mathbf{d}}_2$  by  $s \geq 0$ . Thus, the squeeze action can be represented by  $\rho(\hat{\mathbf{d}}_1, s\hat{\mathbf{d}}_2)$ , where  $\rho \geq 0$  is referred to as the *squeeze depth*.

---

**Algorithm 2** Two-finger pickup of a 3D solid
 

---

**Input:** values of physical parameters, shape geometry, contacts  $\mathbb{K}_0 \cup \{i, j\}$ , squeeze  $(\hat{\mathbf{d}}_1, s\hat{\mathbf{d}}_2)$

**Output:** liftoff outcome

```

1: if  $\mathbf{p}_i$  and  $\mathbf{p}_j$  are not force closure with the plane contact then
2:   return failure
3: end if
4: while not yet "liftable" or not enough squeeze do
5:   increment the squeeze depth  $\rho$ 
6:   update the contact configuration (Subroutine 3 in Section 4.4.1)
7:   if a fingertip slips then
8:     return failure
9:   end if
10:  update the liftable weight  $w(\rho)$  (Subroutine 4 in Section 4.4.2)
11: end while
12: if  $w(\rho) \geq w_0$  then
13:  lift the object off  $\mathcal{P}$ 
14:  if a fingertip slips then
15:    return failure
16:  else
17:    return success
18:  end if
19: else
20:  return failure
21: end if

```

---

The **while** loop of lines 4–11 performs the squeeze until upward forces can balance the gravity of the object. As the squeeze depth  $\rho$  increases, the finger contacts will grow from points into regions. The contact region with the plane will also change.

The movements of all the sliding nodes are tracked. Their indices form a set  $\mathbb{P}$ . The indices of all the sticking nodes also form a set  $\mathbb{T}$ . Together they make up the contact index set  $\mathbb{C} = \mathbb{P} \cup \mathbb{T}$ . Denote by  $\mathbb{I}, \mathbb{J}, \mathbb{K}$  the sets of the indices of the object's surface nodes that are in contact with  $\mathcal{F}_1, \mathcal{F}_2, \mathcal{P}$ , respectively. They also change as the squeeze continues. Clearly,  $\mathbb{C} = \mathbb{I} \cup \mathbb{J} \cup \mathbb{K}$ .

We extend the three-finger squeeze-grasp algorithm from (20) on grasping deformable 2D objects. The squeeze depth  $\rho$  will be sequenced such that at every depth in the sequence some event happens.

The squeeze continues until the object becomes liftable, or the amount of squeeze becomes so large that a pickup is deemed impossible under the initial finger placement and the squeezing directions. In the former case, the fingers translate upward to lift the objects. If during the squeeze or pickup all the contacts with one finger are sliding, then the finger slips and the operation fails. This situation is checked on lines 7–9 and 14–15. Otherwise, the object is successfully picked up.

Line 5 of Algorithm 2 applies an extra squeeze in the current iteration. Line 6 updates on the nodes that are in contact with either fingertip or the plane. It also determines their contact modes and displacements. This update will be described in Section 4.4.1. After the extra of squeeze, virtual lifting is performed to determine whether the fingers have made enough contact with the object to pick it up. The liftability test, carried out on line 10, will be introduced in Section 4.4.2.

#### 4.4.1 Updating Shape and Contact Configuration

As in 2D deformable grasping (20), we know that during the deformation four events may happen between the object, the supporting plane, and the two fingertips: contact establishment (A), contact break (B), stick-to-slip (C), and slip-to-stick (D). Event A is detected when a node is about to penetrate into  $\mathcal{F}_1$ ,  $\mathcal{F}_2$ , or  $\mathcal{P}$ . Event B takes place when the contact force at a node is pointing out of the object. Event C happens when the contact force at a node is going out of its friction cone. Event D occurs when the change rate of the sliding distance of a node with respect to the squeeze depth  $\rho$  becomes zero.

This section describes how line 6 in Algorithm 2 updates the contact configuration. From now on, we will use a prime to denote the change in a physical quantity due to the extra squeeze. For example,  $\bar{\mathbf{F}}'$  and  $\bar{\Delta}'$  respectively represent the change in the contact force vector and the displacement vector that have happened under the extra squeeze. It follows from (4.10) that

$$\bar{\mathbf{F}}' = C\bar{\Delta}'. \quad (4.11)$$

---

**Subroutine 3** Contact and deformation update
 

---

**Input:**  $\Delta, \mathbb{I}, \mathbb{J}, \mathbb{K}, \mathbb{T}, \mathbb{P}$  at  $\rho^{(l)}$ 
**Output:** their values at  $\rho^{(l+1)}$ 

- 1: solve for  $\bar{\mathbf{F}}'$  and  $\Delta'$  based on the contact state just before the extra squeeze in line 5 of Algorithm 2
  - 2: **if** a contact event happens **then**
  - 3:     update the index sets  $\mathbb{I}, \mathbb{J}, \mathbb{K}$  of finger contacts
  - 4:     update the index sets  $\mathbb{T}$  and  $\mathbb{P}$  of sticking and sliding contacts
  - 5: **end if**
  - 6: solve for contact slips and modify  $\bar{\mathbf{F}}'$  and  $\Delta'$  again based on updated contact state
- 

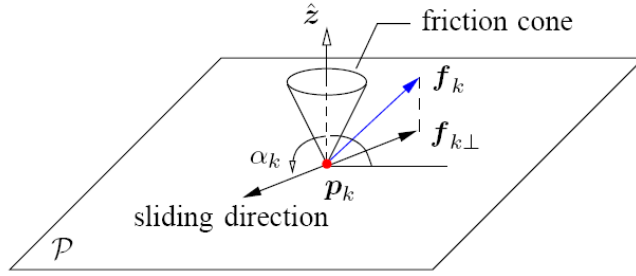


Figure 4.1 Sliding of a node on the plane.

#### 4.4.1.1 Extra Displacement of a Node

Subroutine 3 describe the details of line 6 in Algorithm 2. It handles the update of contact configuration in two rounds.

Line 1 of the subroutine evaluates  $\bar{\mathbf{F}}'$  and  $\Delta'$  that would happen with the squeeze depth increment if the contact state does not change. Every sticking node  $\mathbf{p}_k$  is assumed to remain sticking during this extra squeeze. A node  $\mathbf{p}_k$  that was sliding at  $\rho^{(l)}$  before the extra squeeze is assumed to continue sliding in the same direction, i.e. , its extra displacement is

$$\delta'_k = \mathbf{0}. \quad (4.12)$$

Suppose that a node is sliding on the supporting plane in the direction given by the polar angle  $\alpha_k$  as shown in Figure 4.1. The extra displacement of the node is then

$$\delta'_k = d_k (\cos \alpha_k, \sin \alpha_k, 0)^T, \quad (4.13)$$

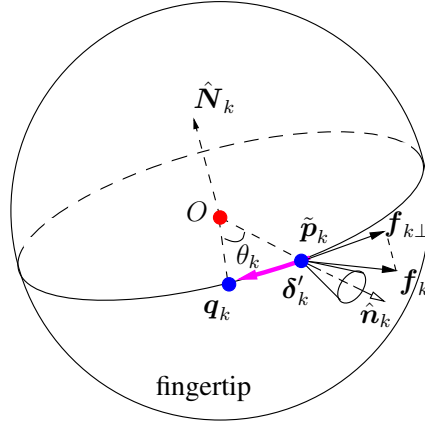


Figure 4.2 Sliding of a node on the plane.

where  $d_k$  is the sliding distance. And its contact force  $\mathbf{f}_k$  lies on the boundary of the friction cone is described by the following quadratic equation:

$$(1 + \mu_{\mathcal{P}}^2)(\mathbf{f}_k \cdot \hat{\mathbf{z}})^2 = \mathbf{f}_k \cdot \mathbf{f}_k, \quad (4.14)$$

where  $\mu_{\mathcal{P}}$  is the coefficient of friction between the object and the plane.

Now we look at the situation that a node  $\mathbf{p}_k$  slides on a fingertip as illustrated in Figure 4.2. At  $\rho^{(l)}$ ,  $\mathbf{p}_k$  was at the position  $\tilde{\mathbf{p}}_k$  with the normal  $\hat{\mathbf{n}}_k$  pointing out of the fingertip. Let  $\hat{\mathbf{t}}_k$  be the tangential direction in which it was sliding at the moment. The node  $\mathbf{p}_k$  will reach some point  $\mathbf{q}_k$  on the great circle co-planar with  $\hat{\mathbf{t}}_k$  and  $\hat{\mathbf{n}}_k$ . The change in the displacement as a result of this extra squeeze will be

$$\delta'_k = \mathbf{q}_k - \tilde{\mathbf{p}}_k. \quad (4.15)$$

The unit normal  $\hat{\mathbf{N}}_k$  to the plane containing this great circle is in the direction of  $\hat{\mathbf{t}}_k \times \hat{\mathbf{n}}_k$ . Essentially,  $\mathbf{q}_k$  is obtained from rotating  $\tilde{\mathbf{p}}_k$  about  $\hat{\mathbf{N}}_k$  through some angle  $\theta_k < 0$ . We have  $\mathbf{q}_k = \mathbf{o} + c_k(\tilde{\mathbf{p}}_k - \mathbf{o}) + s_k(\hat{\mathbf{N}}_k \times (\tilde{\mathbf{p}}_k - \mathbf{o}))$ , where  $\mathbf{o}$  is the center of the fingertip, and  $c_k$  and  $s_k$  are the shorthand notations for  $\cos \theta_k$  and  $\sin \theta_k$ , respectively. Under Coulomb's law, the force  $\mathbf{f}_k$  lying on the friction cone yields a quadratic equation:

$$(1 + \mu_{\mathcal{F}}^2)(\mathbf{f}_k \cdot \hat{\mathbf{n}}_k)^2 = \mathbf{f}_k \cdot \mathbf{f}_k, \quad (4.16)$$



coupled with

$$c_k^2 + s_k^2 = 1. \quad (4.17)$$

In the above,  $\mu_{\mathcal{F}}$  is the coefficient of friction between the object and the fingertip.

#### 4.4.1.2 Contact Configuration after the Extra Squeeze

From (4.12), (4.13), and (4.15), the additional displacement of a contact node  $\mathbf{p}_k$  can be summarized as:

$$\delta'_k = \begin{cases} \mathbf{0} & \text{if } k \in \mathbb{T}, \\ d_k(\cos \alpha_k, \sin \alpha_k, 0)^T & \text{if } k \in \mathbb{P} \cap \mathbb{K}, \\ \mathbf{q}_k - \tilde{\mathbf{p}}_k & \text{if } k \in \mathbb{P} \cap (\mathbb{I} \cup \mathbb{J}). \end{cases} \quad (4.18)$$

The change  $\bar{\Delta}'$  in the contact displacement vector is in terms of  $d_k$ ,  $k \in \mathbb{P} \cap \mathbb{K}$ , and  $c_l = \cos \theta_l$ ,  $s_l = \sin \theta_l$ ,  $l \in \mathbb{P} \cap (\mathbb{I} \cup \mathbb{J})$ . So is  $\bar{\mathbf{F}}'$  given in (4.11). Add  $\bar{\mathbf{F}}'$  to the value  $\bar{\mathbf{F}}^{(l)}$  of  $\bar{\mathbf{F}}$  before the extra squeeze, and plug the result into (4.14), or (4.16) and (4.17). We end up with a system of quadratic equations in the same number of variables:

$$\begin{aligned} (1 + \mu_{\mathcal{P}}^2)(\mathbf{f}_k \cdot \hat{\mathbf{z}})^2 &= \mathbf{f}_k \cdot \mathbf{f}_k, & k \in \mathbb{P} \cap \mathbb{K}; \\ (1 + \mu_{\mathcal{F}}^2)(\mathbf{f}_l \cdot \hat{\mathbf{n}}_l)^2 &= \mathbf{f}_l \cdot \mathbf{f}_l, & l \in \mathbb{P} \cap (\mathbb{I} \cup \mathbb{J}), \\ c_l^2 + s_l^2 &= 1, & l \in \mathbb{P} \cap (\mathbb{I} \cup \mathbb{J}). \end{aligned} \quad (4.19)$$

We solve the above system using the homotopy continuation method for  $d_k$ ,  $k \in \mathbb{P} \cap \mathbb{K}$ , and  $c_l, s_l$ ,  $l \in \mathbb{P} \cap (\mathbb{I} \cup \mathbb{J})$ .

We determine the change  $\Delta'$  using (4.6):

$$\Delta' = \sum_{k=1}^{3n-6} \frac{1}{\lambda_k} (\bar{\mathbf{v}}_k^T \bar{\mathbf{F}}') \mathbf{v}_k + (\mathbf{v}_{3n-5}, \dots, \mathbf{v}_{3n}) E^T \bar{\Delta}', \quad (4.20)$$

where the change  $\bar{\mathbf{F}}'$  in the contact force is given in (4.11). Assign  $\Delta \leftarrow \Delta^{(l)} + \Delta'$  and  $\bar{\mathbf{F}} \leftarrow \bar{\mathbf{F}}^{(l)} + \bar{\mathbf{F}}'$ .

Based on the updated  $\Delta$  and  $\bar{\mathbf{F}}$ , line 2 of Subroutine 3 checks for contact events. If an event happens, lines 3 and 4 then update the contact index sets  $\mathbb{I}, \mathbb{J}, \mathbb{K}, \mathbb{T}, \mathbb{P}$ .

#### 4.4.2 Liftability Test

When the squeeze depth  $\rho$  is small, the contacts on the fingertips are not able to create enough friction to lift the object up. As  $\rho$  increases, the fingertips  $\mathcal{F}_1$  and  $\mathcal{F}_2$  may stop squeezing when they “feel” that the object is liftable. To check on such “feeling”, line 10 of Algorithm 2 conducts a virtual liftability test repeatedly as  $\rho$  increases. Such a test, involving no actual physical action, predicts the finger contact forces at the current squeeze depth if the supporting plane  $\mathcal{P}$  were to be removed, and then checks if any of  $\mathcal{F}_1$  and  $\mathcal{F}_2$  was slipping.

A straightforward approach might be performed as the following. We let the set  $\mathbb{C}$  of contact nodes suddenly reduce from  $\mathbb{I} \cup \mathbb{J} \cup \mathbb{K}$  to  $\mathbb{I} \cup \mathbb{J}$  as if the supporting plane  $\mathcal{P}$  were removed. Next, we recompute the contact force vector in two rounds as in Subroutine 3, handling sliding nodes if any. If it ends up with  $\mathcal{F}_1$  or  $\mathcal{F}_2$  sliding, the squeeze test fails and the object is not liftable at the current squeeze depth. The issue with the above test is numerical convergence. The movements of the sliding nodes are solved from the system (4.19) of quadratic equations, in a manner sensitive to the initial guess. Dramatic reduction in the contact set  $\mathbb{C}$  from  $\mathbb{I} \cup \mathbb{J} \cup \mathbb{K}$  to  $\mathbb{I} \cup \mathbb{J}$  causes a big change to the system such that the finger contact positions in the configuration  $\mathbb{I} \cup \mathbb{J} \cup \mathbb{K}$  would serve as a very bad initial guess in the contact configuration  $\mathbb{I} \cup \mathbb{J}$ . Such change is too dramatic for tracking the contact positions even using the homotopy continuation method.

We would like to find a quantity that reflects the continual progress made by the two fingers towards lifting the object up. Its value should change with the squeeze depth  $\rho$ , and can be updated incrementally just like the contact configuration.

This leads us to the notion of “liftable weight”. When  $\rho = 0$ ,  $\mathcal{F}_1$  and  $\mathcal{F}_2$  exert zero contact force. The object would be liftable only if it had zero weight. At a squeeze depth  $\rho$ , the *liftable weight*  $w(\rho)$  is the maximum hypothetical weight of the object that would not result in any fingertip sliding if  $\mathcal{P}$  were removed. The harder the two fingertips squeeze, the more weight they tend to be able to lift. Physics will ensure the function  $w$

---

**Subroutine 4** Update of Lifiable Weight
 

---

**Input:** Lifiable weight  $w(\rho^{(l)})$ 
**Output:** Lifiable weight  $w(\rho^{(l+1)})$ 

- 1: save  $\Delta, \mathbb{I}, \mathbb{J}, \mathbb{K}, \mathbb{T}, \mathbb{P}, \mathbf{c}$
  - 2:  $w \leftarrow w(\rho^{(l)})$
  - 3:  $\mathbb{C} \leftarrow \mathbb{I} \cup \mathbb{J}$
  - 4: **while** no finger slips **do**
  - 5:      $w \leftarrow w + h$
  - 6:     re-evaluate  $\bar{\mathbf{F}}$  according to (4.10) with  $mg$  replaced by  $w$
  - 7:     detect contact events
  - 8:     update  $\mathbb{I}, \mathbb{J}, \mathbb{T}, \mathbb{P}$
  - 9:     determine if  $\mathbb{I} \cap \mathbb{P} = \mathbb{I}$  or  $\mathbb{J} \cap \mathbb{P} = \mathbb{J}$
  - 10: **end while**
  - 11:  $w(\rho^{(l+1)}) \leftarrow w - h$
  - 12: restore  $\Delta, \mathbb{I}, \mathbb{J}, \mathbb{K}, \mathbb{T}, \mathbb{P}, \mathbf{c}$
- 

to be continuous in  $\rho$ . Generally, we expect  $w$  to be also monotonically increasing.

The idea is then to track  $w(\rho)$  as  $\rho$  increases until it equals the real weight  $w_0$  of the object. Consider the  $l$ th iteration of the **while** loop of lines 4–11 in Algorithm 2, when the squeeze depth increases from, say,  $\rho^{(l)}$  to  $\rho^{(l+1)}$ . Line 10 expands into Subroutine 4, which obtains  $w(\rho^{(l+1)})$  based on the contact configuration at  $\rho^{(l+1)}$  and the lifiable weight  $w(\rho^{(l)})$  at  $\rho^{(l)}$ . It iterates to test the weights  $w(\rho^{(l)}) + h, w(\rho^{(l)}) + 2h, \dots$ , for some small increment  $h$ , until the object is no longer lifiable at some  $w(\rho^{(l)} + kh), k > 0$ . Then, set  $w(\rho^{(l+1)}) = w(\rho^{(l)}) + (k - 1)h$ .

Line 1 in the subroutine saves the shape and contact configuration at the current squeeze depth  $\rho^{(l+1)}$ . They result from the extra squeeze performed in line 5 of Algorithm 2, and are updated in line 6.

In line 3 of Subroutine 4, the contact index set is set to  $\mathbb{I} \cup \mathbb{J}$ , to reflect the hypothetical removal of the supporting plane. The **while** loop of lines 4–10 determines the lifiable weight at the squeeze depth  $\rho^{(l+1)}$  by performing a virtual lift operation. Line 6 recomputes the hypothetical finger contact forces  $\bar{\mathbf{F}}$  according to (4.10) with  $mg$  replaced by  $w$ . Lines 7–8 detect the contact events and, if any, update the contact state accordingly.

Line 9 checks if any of the fingertips slips.

After line 11 updates the liftable weight over the new squeeze depth  $\rho^{(l+1)}$ , the real shape and contact configurations are restored. The execution goes back to line 4 of Algorithm 2.

Since the squeeze depth  $\rho$  undergoes a small increment, small changes occur to the contact configuration and the liftable weight  $w(\rho)$ , which makes tracking of  $w$  feasible. Once  $w$  reaches or exceeds the actual weight  $w_0$  of the object, the liftable test is passed.

Figure 4.3 shows a tomato grasped by two hemispherical plastic fingertips of radius 0.2 mounted on the fingers of a Barrett Hand. As plotted in (a), the ratio  $w/w_0$  increases monotonically with the squeeze depth  $\rho$ . The object becomes liftable when  $\rho = 0.0088$ . The moment is shown in (b) with seven contact nodes on each finger and five in the plane. The object is lifted off the plane as shown in (c).

Once the liftable test is passed, in line 13 of Algorithm 2 the two fingers translate upward. During the lift, the nodal contacts with the plane  $\mathcal{P}$  will break one by one, and some contacts with the fingertips could also break under the gravitational force. However, Contact modeling is no different from that in squeezing. If a fingertip slips during the lift, the pickup fails. Otherwise, the pickup is a success once the object leaves the plane.

#### 4.4.3 Experiment

Experiment was performed with a Barrett Hand mounted with hemispherical fingertips of radius 0.02. The fingertips are made of the material acetal. Tetrahedral meshes for objects used in the experiment were first acquired by a 3D scanner from Next Engine, Inc., and then simplified using MeshLab<sup>1</sup>. Generation of tetrahedral meshes and transformation of the objects were implemented using the Computational Geometry Algorithm Library (<http://www.cgal.org>). All computation was performed on a PC with an Intel Core i7-3770 Processor and 8 GB system RAM.

<sup>1</sup><http://meshlab.sourceforge.net/>

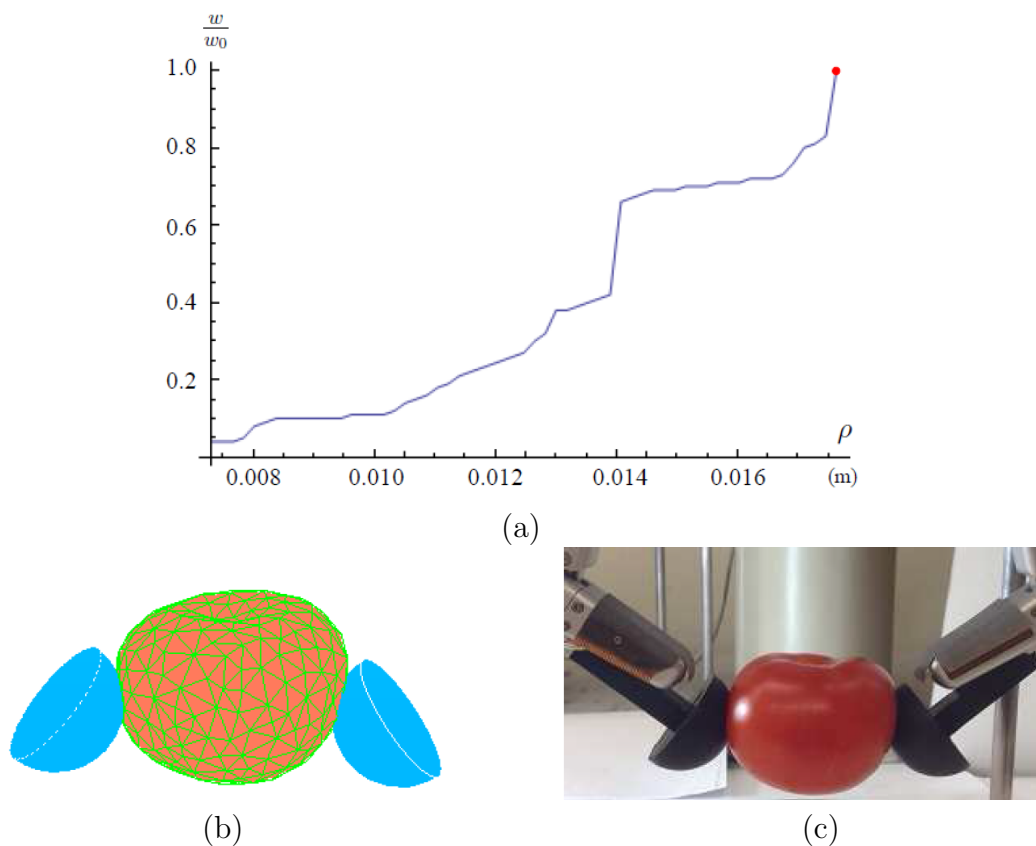


Figure 4.3 Liftability test for a tomato: (a) Ratio of the liftable weight  $w$  to the tomato's actual weight  $w_0 = 1.246$  increases with the squeeze depth  $\rho$ . (b) Shape and contact configuration at the squeeze depth  $\rho = 0.0088$  when the tomato becomes liftable. (c) Liftoff of the tomato at the same squeeze depth. Young's modulus  $E = 10^5$ , Poisson's ratio  $\nu = 0.4$ , and the coefficient of friction  $\mu_{\mathcal{F}} = 0.32$  for the finger-tomato contacts.

To validate Algorithm 2, we performed the experiments on the tomato in Figure 4.3, and four other objects listed in Figure 4.4: an orange, an eggplant, a steamed bun, and a toy football.

Table 4.1 lists the mesh and physical parameter values of the five objects. In the table,  $\mu_{\mathcal{P}}$  and  $\mu_{\mathcal{F}}$  are the coefficients of friction between the plane and the object and between the fingertips and the object, respectively. On all five objects, the two fingertips applied a squeeze  $\rho(\hat{\mathbf{d}}_1, \hat{\mathbf{d}}_2)$ , where  $\hat{\mathbf{d}}_1 = (0, 0.974, -0.227)$  and  $\hat{\mathbf{d}}_2 = (0, -0.974, -0.227)$ . As soon as the liftability test was passed at the squeeze depth  $\rho^*$ , the fingers switched

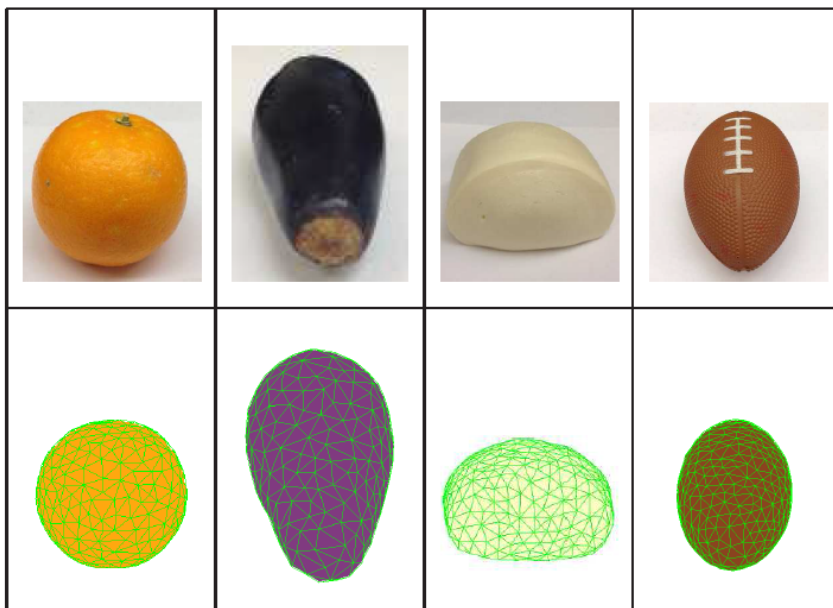


Figure 4.4 Objects (a) at rest and (b) in tetrahedral mesh representations.

their action from squeezing to lifting.

The results are shown in Figure 4.5, the first row shows the four objects picked up by the Barrett Hand, the second row shows the simulation results, at the squeeze depths listed in the third row, respectively. The fourth row lists the numbers of contact nodes when the objects are in the air. The fifth row lists the simulation times (in seconds) of Algorithm 2 before the pickup, which were significantly less than the times spent on computing the spectral decompositions of the stiffness matrices using the SVD, which were 53.7, 99.0, 106.3, 130.6, and 299.2, respectively.

We also perform some experiments to check how closely the liftability test capture the moment when an object becomes liftable. Comparison is done between the minimum squeeze passing the liftability test and the minimum squeeze for a liftoff. Denote by  $f^*$  the magnitude of the total squeeze force exerted by the fingers at the squeeze depth  $\rho^*$  passing the liftability test. Meanwhile, denote by  $\rho_{\min}$  the minimum squeeze depth for a lift, and  $f_{\min}$  the magnitude of the total force exerted by the two fingers at the moment of the object breaking its contact with the table.  $\rho_{\min}$  can be computed via bisection over

Table 4.1 Parameters with the objects in Figure 4.3 and 4.4.

	Tomato	Orange	Eggplant	Bun	Football
# Vert.	490	600	612	658	875
# Facets	498	564	616	646	782
# Tetra.	2129	2692	2676	2941	4058
$w_0$	1.246	1.868	3.336	0.467	0.489
$E$	$1.0 \times 10^5$	$1.4 \times 10^5$	$1.1 \times 10^5$	$2 \times 10^3$	$6 \times 10^3$
$\nu$	0.4	0.4	0.4	0.2	0.3
$\mu_{\mathcal{F}}$	0.32	0.34	0.5	0.4	0.45
$\mu_{\mathcal{P}}$	0.35	0.36	0.6	0.42	0.47

$[0, \rho^*]$ , since  $\rho = \rho^*$  has resulted in a success and  $\rho = 0$  will lead to a failure. For every intermediate value of  $\rho$ , the corresponding squeeze and the following lift attempt are simulated by updating the shape and contact configuration as described in Section 4.4.1. The outcome is a success if no finger slips on the object before the object breaks contact with the table, and a failure otherwise.

Table 4.2 compares  $(\rho^*, f^*)$  with  $(\rho_{\min}, f_{\min})$  over the five objects under the same finger placements and squeeze directions in the experiment. We see that for every object  $\rho^*$  and  $f^*$  are slightly greater than  $\rho_{\min}$  and  $f_{\min}$ , respectively. This suggests that the liftability test is conservative. In the liftability test the supporting plane is suddenly removed, while in calculating  $\rho_{\min}$  the object breaks contact with the table one node after another. In the latter case, less force needs to be exerted on the object to prevent the fingertips from sliding, and thus, less squeeze needs to be performed.



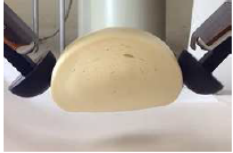

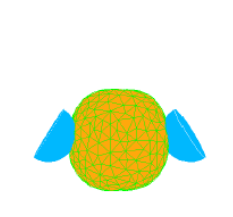
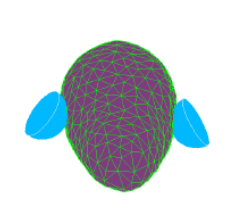
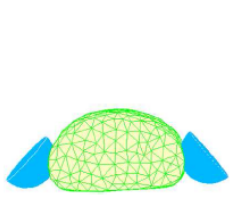
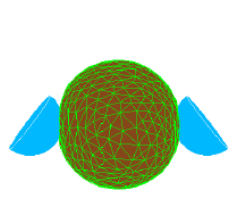
			
			
$\rho^* = 0.0124$	0.0071	0.0052	0.0053
# nodes: 15	8	10	8
Simul. time: 2.75	2.41	3.12	2.54

Figure 4.5 Successful pickups of four deformable objects. The liftoff configurations in experiment (row 1) and simulation (row 2). Row 3 lists the squeeze depths passing the liftable test at which the action switches to pickup. Rows 4 and 5 display respectively the numbers of contact nodes at liftoff and the simulation times.

Table 4.2 Comparisons between the squeeze depth  $\rho^*$  predicted by the liftable test and the minimum squeeze depth  $\rho_{\min}$  for lift off, and between the corresponding total forces  $f^*$  and  $f_{\min}$  exerted by the two fingers. The results are listed for the five objects used in the experiment.

	Tomato	Orange	Eggplant	Bun	Football
$\rho^*$	0.01764	0.0247	0.01412	0.01028	0.01058
$f^*$	2.173	3.041	3.881	0.727	0.632
$\rho_{\min}$	0.01587	0.02383	0.01355	0.00982	0.01039
$f_{\min}$	2.055	2.913	3.74	0.638	0.605



## CHAPTER 5. MODELING OF $N$ -BODY COLLISIONS

This chapter will begin with introducing a frictionless impact model of balls without considering angular velocities. It will then generalize the model to collision under general motions with friction. Finally, simulation and experiment on Newton's cradle is performed to validate the model in the frictionless case, and simulation of nine-ball break shots is presented.

### 5.1 Frictionless Collision of Translating Balls

In this section, we investigate a frictionless collision among  $n$  translating balls whose centers of mass are co-planar, and describe an algorithm to compute the collision outcome. In the next section, the model will be extended to objects with arbitrary geometry, rotating motions, and contact friction. Later in this section, the model is then applied to solve the classical problem of Newton's Cradle.

#### 5.1.1 Impact Dynamics and Contact Kinematics

Suppose that  $n$  rigid balls  $\mathcal{B}_1, \dots, \mathcal{B}_n$  are engaged in a collision. Let  $\mathbf{v}_i$  be the velocity of  $\mathcal{B}_i$ ,  $\mathbf{I}_{ij}$  the impulse that  $\mathcal{B}_i$  receives from  $\mathcal{B}_j$ . By Newton's third law,  $\mathbf{I}_{ij} = -\mathbf{I}_{ji}$ . For  $1 \leq i \leq n$ , denote  $\mathcal{C}_i$  as the set of subscripts of the objects that are in contact with  $\mathcal{B}_i$ , which has initial velocity  $\mathbf{v}_i^{(0)}$ . Then the velocity of  $\mathcal{B}_i$  during the collision changes as follows:

$$\mathbf{v}_i = \mathbf{v}_i^{(0)} + \frac{1}{m_i} \sum_{k \in \mathcal{C}_i} \mathbf{I}_{ik}, \quad i = 1, 2, \dots, n. \quad (5.1)$$

For every two balls  $\mathcal{B}_i$  and  $\mathcal{B}_j$  in contact, we add a virtual spring  $\{i, j\}$  at the contact point. Without ambiguity, we will also refer to the contact by the same notation  $\{i, j\}$ . This spring is along the contacting normal which is perpendicular to their common tangent plane.

Figure 5.1 shows the ball  $\mathcal{B}_i$  with the contact set  $\mathbb{C}_i = \{j_1, j_2, j_3\}$ . Since impulsive forces on the balls are much larger than the gravitational forces, it is ignored here consequently. Reorient the system such that all the balls lie on a horizontal plane. For the spring  $\{i, j\}$ , let  $\theta_{ij}$  be the angle from the  $x$ -axis to the spring direction vector, which points from  $\mathcal{B}_j$  to  $\mathcal{B}_i$  if  $j > i$ , and in the opposite direction otherwise. Thus, the unit normal vector  $\hat{\mathbf{n}}_{ij} = (\cos \theta_{ij}, \sin \theta_{ij})$  always points from the ball with the bigger subscript to the ball with the smaller one. We let  $I_{ij} = \sigma_{ij} \|\mathbf{I}_{ij}\|$ , where

$$\sigma_{ij} = \begin{cases} 1, & \text{if } i < j, \\ -1, & \text{if } i > j. \end{cases}$$

The velocity components of ball  $\mathcal{B}_i$  during impact can then be written as:

$$\begin{pmatrix} v_{ix} \\ v_{iy} \end{pmatrix} = \begin{pmatrix} v_{ix}^{(0)} \\ v_{iy}^{(0)} \end{pmatrix} + \frac{1}{m_i} \sum_{k \in \mathbb{C}_i} \begin{pmatrix} I_{ik} \cos \theta_{ik} \\ I_{ik} \sin \theta_{ik} \end{pmatrix}. \quad (5.2)$$

Denote  $\mathbb{P}$  as the set of contacts, and  $\tilde{v}_{ij}$  as  $\mathcal{B}_i$ 's velocity component projected onto the direction of the spring  $\{i, j\}$ . For every contact  $\{i, j\} \in \mathbb{P}$ , we thus have

$$\tilde{v}_{ij} = \mathbf{v}_i \cdot \hat{\mathbf{n}}_{ij}. \quad (5.3)$$

Let  $x_{ij}$  be the change in length of the virtual spring  $\{i, j\}$ , and  $k_{ij}$  as its stiffness. The derivative of energy with respect to its impulse follow from (5.1) and (5.3):

$$\begin{aligned} \frac{dE_{ij}}{dI_{ij}} &= -\dot{x}_{ij} = \tilde{v}_{ji} - \tilde{v}_{ij} \\ &= \left( \mathbf{v}_j^{(0)} - \mathbf{v}_i^{(0)} \right) \cdot \hat{\mathbf{n}}_{ij} + \frac{1}{m_j} \sum_{k \in \mathbb{C}_j} I_{jk} (\hat{\mathbf{n}}_{jk} \cdot \hat{\mathbf{n}}_{ij}) - \frac{1}{m_i} \sum_{k \in \mathbb{C}_i} I_{ik} (\hat{\mathbf{n}}_{ik} \cdot \hat{\mathbf{n}}_{ij}). \end{aligned}$$

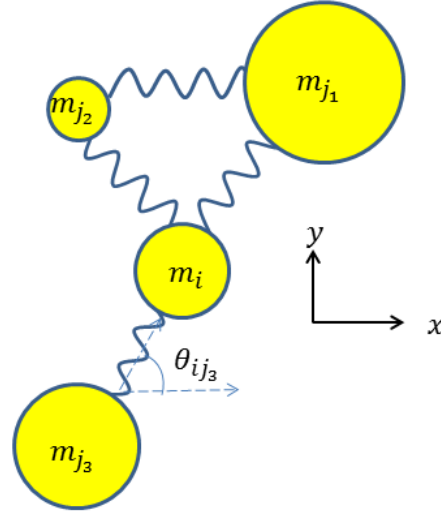


Figure 5.1 Contact modeling with virtual springs.

The potential energy stored in the spring  $\{i, j\}$  is  $E_{ij} = \frac{1}{2}k_{ij}x_{ij}^2$ , and by Hooke's law the formula for the contact force is  $F_{ij} = k_{ij}x_{ij}$ . Suppose the spring  $\{p, q\}$  is the primary impulse  $I_{pq}$ , which has the largest growth during the period. The expression of  $dE_{pq}/dI_{pq}$  is given by (5.4) after replacing  $i, j$  with  $p, q$  from (5.4). Then, the differential ratio between  $I_{ij}$  and  $I_{pq}$  can be derived as

$$\rho_{ij} = \frac{dI_{ij}}{dI_{pq}} = \frac{F_{ij}}{F_{pq}} = \sigma_{ij}\sigma_{pq} \sqrt{\frac{k_{ij}E_{ij}}{k_{pq}E_{pq}}}. \quad (5.4)$$

Integration of (5.4) with initial value  $I_{ij}^{(0)}$  yields the accumulated change of energy:

$$\begin{aligned} \Delta E_{ij} = & \left( \mathbf{v}_j^{(0)} - \mathbf{v}_i^{(0)} \right) \cdot \hat{\mathbf{n}}_{ij} \Delta I_{ij} - \frac{1}{m_i} \sum_{k \in \mathbb{C}_i} \int_{\rho_{ij} I_{pq}^{(0)}}^{\rho_{ij} (I_{pq}^{(0)} + \delta)} (\hat{\mathbf{n}}_{ik} \cdot \hat{\mathbf{n}}_{ij}) \Delta I_{ik} dI_{ij} \\ & + \frac{1}{m_j} \sum_{k \in \mathbb{C}_j} \int_{\rho_{ij} I_{pq}^{(0)}}^{\rho_{ij} (I_{pq}^{(0)} + \delta)} (\hat{\mathbf{n}}_{jk} \cdot \hat{\mathbf{n}}_{ij}) \Delta I_{jk} dI_{ij} + \alpha_{ij} (e_{ij}^2 - 1) E_{ijmax}, \end{aligned} \quad (5.5)$$

where  $\delta$  is the increment of the primary impulse  $I_{pq}$ , and  $e_{ij} \in [0, 1]$  is the energy coefficient of restitution determined by the material properties of the two impacting objects. After the spring ends compression, it starts to restitute, with the stiffness  $k_{ij}$  adjusted to  $k_{ij}/e_{ij}^2$  to reflect material hardening as explained in (21). The value of  $\alpha_{ij}$  is

set to be 0 during compression and 1 during restitution. At the end of compression, the spring stores the maximum elastic energy  $E_{ijmax}$ , and then immediately loses a portion of  $1 - e_{ij}^2$ . We can work out the integrals in (5.5) below:

$$\int_{\rho_{ij} I_{pq}^{(0)}}^{\rho_{ij} (I_{pq}^{(0)} + \delta)} \Delta I_{ik} dI_{ij} = c \rho_{ij} \rho_{ik}, \quad (5.6)$$

$$\int_{\rho_{ij} I_{pq}^{(0)}}^{\rho_{ij} (I_{pq}^{(0)} + \delta)} \Delta I_{jk} dI_{ij} = c \rho_{ij} \rho_{jk}, \quad (5.7)$$

where  $c = (\delta^2 + 2I_{pq}^{(0)}\delta)/2$ . Substituting (5.6), (5.7) into (5.5), and adding initial energy  $E_{ij}^{(0)}$ , we get

$$\begin{aligned} E_{ij} = & E_{ij}^{(0)} + \delta \left( \frac{dE_{ij}}{dI_{ij}} \right)^{(0)} \rho_{ij} - c \left( \frac{1}{m_j} + \frac{1}{m_i} \right) \rho_{ij}^2 + \frac{c \rho_{ij}}{m_j} \left( \sum_{k \neq i, k \in \mathbb{C}_j} \rho_{jk} (\hat{\mathbf{n}}_{jk} \cdot \hat{\mathbf{n}}_{ij}) \right) \\ & - \frac{c \rho_{ij}}{m_i} \left( \sum_{k \neq j, k \in \mathbb{C}_i} \rho_{ik} (\hat{\mathbf{n}}_{ik} \cdot \hat{\mathbf{n}}_{ij}) \right) + \alpha_{ij} (e_{ij}^2 - 1) E_{ijmax}. \end{aligned} \quad (5.8)$$

Squaring both sides of (5.4) and then plugging in (5.8), we get a cubic system of equations:

$$\frac{k_{pq}}{k_{ij}} \rho_{ij}^2 E_{pq} = E_{ij}, \quad \{i, j\} \in \mathbb{P}. \quad (5.9)$$

Newton's method can be applied to solve this non-linear system, with the initial guesses of 1 for  $\rho_{pq}$ , where  $\{p, q\}$  is the contact yielding the primary impulse, and of 0 for  $\rho_{ij}$ , for any  $\{i, j\} \neq \{p, q\}$ . In the first round of initialization, if any  $\rho_{ij}$  exceeds 1, set the primary contact  $\{p, q\}$  to be such  $\{i, j\}$  that has the biggest  $\rho_{ij}$  value. With the updated primary impulse pair, the system should now be solved again to finish the initialization. This process ensures the impulse that varies the most stay as the denominator in the differential relationships, which improves numerical stability.

### 5.1.2 Numerical Integration

After initialization of  $\rho_{ij}^{(0)}$ , numerical integration is performed as follows. At the  $n$ th step, increment the primary impulse  $I_{pq}$  by some small amount  $\delta$ , and make the updates

---

**Algorithm 5** Frictionless collision for  $n$  balls with translation only
 

---

**Input:**  $\mathcal{B}_i$  with velocities  $\mathbf{v}_i^{(0)}$ ,  $1 \leq i \leq n$ , and contact set  $\mathbb{P}$

- 1: set the active contact set  $\mathbb{A} = \mathbb{P}$
  - 2: **while**  $\mathbb{A} \neq \emptyset$  **do**
  - 3:     solve  $\rho_{ij}$  from the system (5.9), update  $\mathbf{I}_{ij}, E_{ij}$  according to (5.11) and (5.12), also  $\mathbf{v}_i, 1 \leq i \leq n$  according to (5.1)
  - 4:     **while**  $\mathbb{A}$  does not change **do**
  - 5:         update  $\rho_{ij}, \mathbf{I}_{ij}, E_{ij}$ , for all  $\{i, j\} \in \mathbb{A}$  and  $\mathbf{v}_i, 1 \leq i \leq n$  according to (5.10)–(5.12), and (5.1)
  - 6:         **for** every  $\{i, j\} \in \mathbb{A}$  **do**
  - 7:             **if** compression ends **then**
  - 8:                 set  $E_{ij} = e^2 E_{ij}$
  - 9:             **else if** restitution ends **then**
  - 10:                 remove the contact  $\{i, j\}$  from  $\mathbb{A}$
  - 11:             **end if**
  - 12:         **end for**
  - 13:         **for** every  $\{i, j\} \in \mathbb{P} \setminus \mathbb{A}$  that  $\mathbf{v}_i = \mathbf{v}_j$  **do**
  - 14:             add contact  $\{i, j\}$  to  $\mathbb{A}$
  - 15:         **end for**
  - 16:     **end while**
  - 17: **end while**
- 

below:

$$\rho_{ij}^{(n)} = \sigma_{ij} \sigma_{pq} \sqrt{\frac{k_{ij} E_{ij}^{(n-1)}}{k_{pq} E_{pq}^{(n-1)}}}, \quad (5.10)$$

$$\mathbf{I}_{ij}^{(n)} = \mathbf{I}_{ij}^{(n-1)} + \delta \rho_{ij}^{(n)}, \quad (5.11)$$

$$E_{ij}^{(n)} = E_{ij}^{(n-1)} + \delta \rho_{ij}^{(n)} \left( \frac{dE_{ij}}{dI_{ij}} \right)^{(n)}, \quad (5.12)$$

where  $\left( \frac{dE_{ij}}{dI_{ij}} \right)^{(n-1)}$  is evaluated according to (5.4). In the step, the ball velocities are computed from (5.1). Algorithm 5 summarizes the above procedure.

### 5.1.3 Example

A Newton's cradle as Shown in Figure 5.2 consists of five identical balls with mass  $m$  and radius  $r$  aligned in a row. Each ball is hanged by a string of length  $l$ . Denote by  $e$  the energy coefficient of restitution between two balls. Usually one drags the left end ball to a certain height and then releases it. Several multi-body collisions will happen

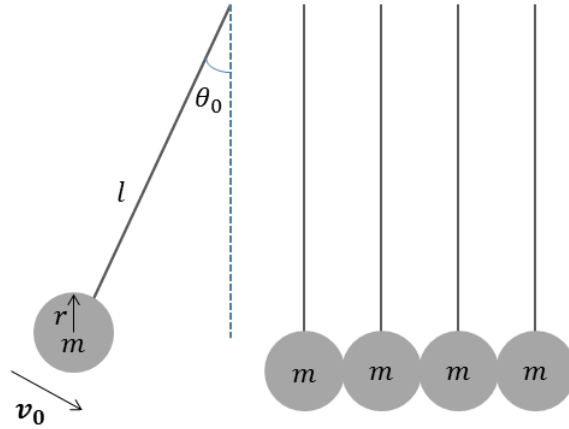


Figure 5.2 Newton's cradle.

after the release. Every ball carries out a simple pendulum motion before it collides with another ball. The angle  $\theta(t)$  between the perpendicular direction and the string at time  $t$  satisfies a second order ordinary differential equation. When it is small, under the approximation  $\sin \theta \approx \theta$ , the angle has a solution in the form of

$$\theta(t) = A \cos(\omega t + \phi),$$

where  $\omega = \sqrt{g/l}$ , with  $g$  as the gravitational acceleration constant. The constants  $A$  and  $\phi$  can be determined from the initial configuration at time  $t = t_0$ : the angle  $\theta_0$  of the pendulum and the tangential velocity  $v_0$  as shown in Figure 5.2. We can obtain

$$\begin{aligned} \theta(t) &= \sqrt{\theta_0^2 + \frac{v_0^2}{gl}} \cos\left(\sqrt{\frac{g}{l}}t + \beta_0 - \sqrt{\frac{g}{l}}t_0\right), \\ v(t) &= -\sqrt{\theta_0^2 + \frac{v_0^2}{gl}} \sqrt{gl} \sin\left(\sqrt{\frac{g}{l}}t + \beta_0 - \sqrt{\frac{g}{l}}t_0\right). \end{aligned}$$

where  $\beta_0$  is a constant offset determined by  $\theta_0$ ,  $v_0$ ,  $g$ , and  $l$ .

As time goes by, collisions are detected by checking if several balls are close enough with non-negligible relative velocities. A ball will switch to a different simple pendulum motion if collision happens which results in a sudden change of velocity. Algorithm 5 is applied to compute the motion of the balls for each collision. For more accuracy of

modeling, Hertz contact is used with  $F = kx^{3/2}$ . Then (5.4) becomes

$$\rho_{ij} = \frac{dI_{ij}}{dI_{pq}} = \frac{F_{ij}}{F_{pq}} = \sigma_{ij}\sigma_{pq} \sqrt[5/2]{\frac{k_{ij}E_{ij}^{3/2}}{k_{pq}E_{pq}^{3/2}}}.$$

Newton's method can still be applied to solve this quartic polynomial system. Simulation and experimental results will be shown in Section 5.3.1.

## 5.2 Collision under General Motions with Friction

In this section, we will extend the impact model by considering friction and angular velocity of arbitrary shape objects in the system of collision treated in Section 5.1. As before, the objects involved in the collision are assumed to have their centers of mass lying on the same plane. Suppose for every pair of objects, the center of masses and the contact point are in the same line.

### 5.2.1 Impact Dynamics and Contact Kinematics

Denote by  $\mathbf{v}_i$  and  $\boldsymbol{\omega}_i$  the velocity and angular velocity of the object  $\mathcal{B}_i$  in the world frame. At the moment of collision, let  $\mathbf{r}_{ik}$  be the vector from  $\mathcal{B}_i$ 's center of mass to the contact point between  $\mathcal{B}_i$  and  $\mathcal{B}_k$ . The angular inertia matrix  $Q_i$  of  $\mathcal{B}_i$  is diagonal in its principal frame, which has a rotation described by the matrix  $R_i$  from the world frame. For instance, if  $\mathcal{B}_i$  is a ball with radius  $\tau$ , then

$$Q_i = \frac{2}{5}m_i\tau^2 \begin{pmatrix} 1 & 0 & 0 \\ 0 & 1 & 0 \\ 0 & 0 & 1 \end{pmatrix}.$$

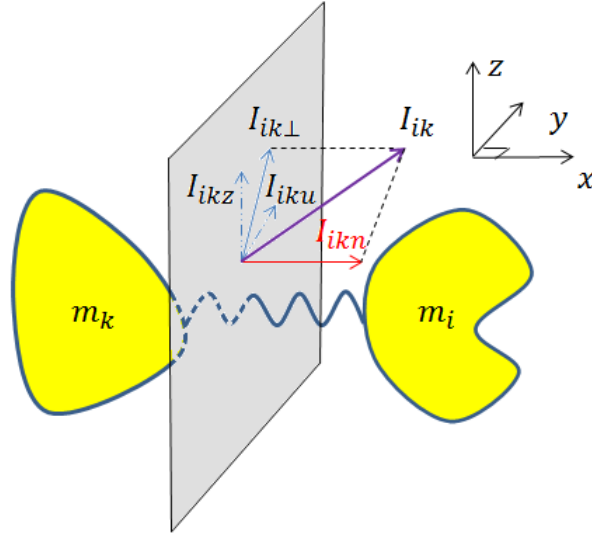


Figure 5.3 Impulse decomposition along normal and tangential directions.

In the world frame, the changes in the velocities and angular velocities of  $\mathcal{B}_i$ ,  $i = 1, \dots, n$ , during the impact can be derived from dynamics:

$$m_i \Delta \mathbf{v}_i = \sum_{k \in \mathcal{C}_i} \mathbf{I}_{ik}, \quad (5.13)$$

$$Q_i (R_i^{-1} \Delta \boldsymbol{\omega}_i) = \sum_{k \in \mathcal{C}_i} R_i^{-1} (\mathbf{r}_{ik} \times \mathbf{I}_{ik}). \quad (5.14)$$

Compared with the frictionless case studied in Section 5.1, impulse now exists in the tangential plane at the contact between two objects. Here, let  $I_{ik\perp}$  be the magnitude of the tangential impulse between  $\mathcal{B}_i$  and  $\mathcal{B}_k$  shown in Figure 5.3, which is the projection of the total impulse  $\mathbf{I}_{ik}$ , exerted by  $\mathcal{B}_k$  on  $\mathcal{B}_i$ , onto the tangential plane. The component of  $I_{ij\perp}$  in the  $x$ - $y$  plane is  $I_{iku}$ , and the vertical component in  $z$ -direction is  $I_{ikz}$ . Compared to (5.2), we now have

$$\begin{pmatrix} v_{ix} \\ v_{iy} \end{pmatrix} = \begin{pmatrix} v_{ix}^{(0)} \\ v_{iy}^{(0)} \end{pmatrix} + \frac{1}{m_i} \sum_{k \in \mathcal{C}_i} \begin{pmatrix} I_{ikn} \cos \theta_{ik} - I_{iku} \sin \theta_{ik} \\ I_{ikn} \sin \theta_{ik} + I_{iku} \cos \theta_{ik} \end{pmatrix}. \quad (5.15)$$



The differential relationship between the energy and normal impulse at the contact between object  $\mathcal{B}_i$  and  $\mathcal{B}_j$  is

$$\begin{aligned} \frac{dE_{ij}}{dI_{ijn}} = & \hat{\mathbf{n}}_{ij} \cdot \left( \left( \mathbf{v}_j^{(0)} - \mathbf{v}_i^{(0)} \right) + \frac{1}{m_j} \sum_{k \in \mathcal{C}_j} (I_{jkn} \hat{\mathbf{n}}_{jk} + I_{jku} \hat{\mathbf{u}}_{jk}) \right. \\ & \left. - \frac{1}{m_i} \sum_{k \in \mathcal{C}_i} (I_{ikn} \hat{\mathbf{n}}_{ik} + I_{iku} \hat{\mathbf{u}}_{ik}) \right). \end{aligned} \quad (5.16)$$

The variable  $\rho_{ij}$  defined in (5.4) for the frictionless case is now replaced by  $\rho_{ijn}$ , whose initial value will still be solved from the system of equations using Newton's method. An expression for  $E_{ij}$  can be derived by integrating (5.16) similarly as in Section 5.1.

During the impact, we need to consider the contact mode (stick or slip) between  $\mathcal{B}_i$  and  $\mathcal{B}_j$ . The contact velocity of  $\mathcal{B}_i$  relative to that of object  $\mathcal{B}_j$  at the contact is

$$\Delta \mathbf{v}_{ij} = \mathbf{v}_i - \mathbf{v}_j + \boldsymbol{\omega}_i \times \mathbf{r}_{ij} - \boldsymbol{\omega}_j \times \mathbf{r}_{ji}.$$

Project  $\Delta \mathbf{v}_{ij}$  onto the tangent plane,

$$\Delta \mathbf{v}_{ij\perp} = \Delta \mathbf{v}_{ij} - \Delta \mathbf{v}_{ij} \cdot \hat{\mathbf{n}}_{ij}. \quad (5.17)$$

After simplification, the right hand side of the above equation can be written as linear combinations of  $\Delta I_{ijx}$ ,  $\Delta I_{ijy}$ , and  $\Delta I_{ijz}$ .

The contacts among the  $n$  objects can be either sliding or sticking. We denote the set of sliding contacts as  $\mathbb{S}$ , and the set of sticking contacts as  $\mathbb{T}$ . The elements in each set are the pairs of indices for objects engaged in the corresponding contact mode. Clearly,  $\mathbb{P} = \mathbb{S} \cup \mathbb{T}$ .

### 5.2.2 Contact Modes

A contact node during the impact could be either sticking or sliding. For all the contacts  $\{i, j\} \in \mathbb{T}$ , their relative velocities in the tangent plane should be zero, i.e.,

$$\Delta \mathbf{v}_{ij\perp} = 0, \quad \{i, j\} \in \mathbb{T}. \quad (5.18)$$

Let  $|\mathbb{T}|$  be the size of the set  $\mathbb{T}$ . The above equations form a linear system with  $3|\mathbb{T}|$  equations and  $3|\mathbb{T}|$  variables. Each  $\Delta\bar{\mathbf{v}}_{ij}$  has three components along the  $x$ -,  $y$ - and  $z$ -axes, and also each equation has  $3|\mathbb{T}|$  variables  $\Delta I_{ijx}$ ,  $\Delta I_{ijy}$ , and  $\Delta I_{ijz}$ ,  $\{i, j\} \in \mathbb{T}$ . The values for  $\Delta I_{ijn}$ ,  $\Delta I_{iju}$ , and  $\Delta I_{ijz}$  can be computed by:

$$\begin{pmatrix} \Delta I_{ijn} \\ \Delta I_{iju} \\ \Delta I_{ijz} \end{pmatrix} = R_{ik}^{-1} \begin{pmatrix} \Delta I_{ijx} \\ \Delta I_{ijy} \\ \Delta I_{ijz} \end{pmatrix}. \quad (5.19)$$

After solving the system, one can check the ratio  $\gamma_{ij}$  between the tangential impulse and the normal impulse at the contact  $\{i, j\}$ , that is,

$$\gamma_{ij} = \Delta I_{ij\perp} / \Delta I_{ijn}.$$

Denote  $\mu_{ij}$  as the coefficient of friction between  $\mathcal{B}_i$  and  $\mathcal{B}_j$ . If  $\gamma_{ij} < \mu_{ij}$ , we still have values of  $\Delta I_{iju}$  and  $\Delta I_{ijz}$  as they are solved from the system, and

$$\Delta I_{ij\perp} = \gamma_{ij} \Delta I_{ijn}. \quad (5.20)$$

A node is sliding when the following holds:

$$\Delta \mathbf{v}_{ij\perp} \neq 0, \quad \{i, j\} \in \mathbb{T}. \quad (5.21)$$

Then,

$$\Delta I_{ij\perp} = \mu_{ij} \Delta I_{ijn}. \quad (5.22)$$

Variables  $\Delta I_{iju}$  and  $\Delta I_{ijz}$  are determined by

$$\begin{aligned} \frac{1}{\|\mathbf{I}_{ij\perp}\|} \begin{pmatrix} \Delta I_{iju} \\ \Delta I_{ijz} \end{pmatrix} &= -\Delta \mathbf{v}_{ij} / \|\Delta \mathbf{v}_{ij}\|, \\ \Delta I_{iju}^2 + \Delta I_{ijz}^2 &= \Delta I_{ij\perp}^2. \end{aligned} \quad (5.23)$$

---

**Algorithm 6** Frictional  $n$ -body collision
 

---

**Input:** objects  $\mathcal{B}_i$  with velocities  $\mathbf{v}_i^{(0)}$  and angular velocities  $\boldsymbol{\omega}_i^{(0)}$ ,  $1 \leq i \leq n$ , and contact set  $\mathbb{P}$

- 1: set the active contact set  $\mathbb{A} = \mathbb{P}$ . Compute the initial relative velocity  $\Delta \mathbf{v}_{ij}$  of each  $\{i, j\} \in \mathbb{A}$  to set up the initial sliding set  $\mathbb{S}$  and sticking set  $\mathbb{T}$ .
- 2: **while**  $\mathbb{A} \neq \emptyset$  **do**
- 3:     solve  $\rho_{ij}$  from the system (5.9) according to  $\frac{dE_{ij}}{dI_{ijn}}$  from (5.16), update  $I_{ijn}, E_{ij}$  from (5.11) and (5.12),  $I_{ij\perp}$  from (5.20) or (5.24), also update  $\mathbf{v}_i, \boldsymbol{\omega}_i, 1 \leq i \leq n$  by (5.13) and (5.14) according to set  $\mathbb{S}$  or  $\mathbb{T}$
- 4:     **while**  $\mathbb{A}$  does not change **do**
- 5:         update  $\rho_{ij}, I_{ijn}, E_{ij}$  and  $\mathbf{v}_i, \boldsymbol{\omega}_i, 1 \leq i \leq n$  from (5.10)–(5.14)
- 6:         check if any of the events happen based on Section 5.2.2. Update the sets  $\mathbb{S}$  and  $\mathbb{T}$ , and values of  $I_{iju}$  and  $I_{ijz}$  of each  $\{i, j\} \in \mathbb{A}$
- 7:         execute lines 6–15 in Algorithm 5
- 8:     **end while**
- 9: **end while**

---

A transition of the contact mode is detected and computed by the following conditions:

1) *sticking to sliding*: if  $\gamma_{ij} \geq \mu_{ij}$ , then sliding happens between  $\mathcal{B}_i$  and  $\mathcal{B}_j$ . According to Coulomb's friction law, we set

$$\Delta I_{ij\perp} = \mu_{ij} \Delta I_{ijn}. \quad (5.24)$$

The values of  $\Delta I_{iju}$  and  $\Delta I_{ijz}$  are modified to be  $\Delta I_{iju} \mu_{ij} / \gamma_{ij}$  and  $\Delta I_{ijz} \mu_{ij} / \gamma_{ij}$ . The sliding direction is opposite to the vector  $(\Delta I_{iju} \mu_{ij} / \gamma_{ij}, \Delta I_{ijz} \mu_{ij} / \gamma_{ij})$ .

2) *sliding to sticking*: whenever the relative velocity  $\Delta \mathbf{v}_{ij}$  vanishes, we move the contact  $\{i, j\}$  from  $\mathbb{S}$  to  $\mathbb{T}$ .

### 5.2.3 Algorithm

We perform numerical integration to update all the impulses, energies, velocities, and angular velocities. The computation is described in Algorithm 6. Simulation results of nine-ball break shots will be presented in Section 5.3.2.

The assumption of the mass centers of the objects being co-planar has been made in this section. However, the model is easily extendable to a general configuration with

modifications of equations (5.15) and (5.16) to take into account the  $z$ -direction components.

### 5.3 Simulation and Experiment

In this section, we first present simulation of Newton's cradle to verify the frictionless model described in Section 5.1, and compare the results with those from an experiment we performed. Next, we conduct simulation on nine-ball break shots using the model in Section 5.2.

#### 5.3.1 Newton's Cradle

To experimentally validate Algorithm 5, a Newton's Cradle with string length  $l = 0.129\text{m}$  was placed on a horizontal table. The five identical balls of the cradle have radius  $r = 0.011\text{m}$ . The coefficient of restitution between any two balls is  $e = 0.95$ , and the stiffness between them is the same. The leftmost ball was initially raised and held static with oscillation angle  $5\pi/36$  as shown in Figure 5.4. Started at the release, a video was captured by a Fujifilm FinePix HS10 camera with frame rate 30fps. Hough Circle Transform algorithm in Matlab was applied to track the contours of five balls during their motion. Velocities were estimated based on the tracked positions of balls and the frame rate.

Table 5.1 compares the horizontal velocities  $v_x$  and  $\tilde{v}_x$  from experiment and simulation, respectively, of the five balls right after they were disengaged from the first collision in the experiment and the simulation. Interestingly, ball 1 was moving leftward slightly, and ball 4 was moving rightward with noticeable velocity in both the experiment and simulation. This phenomenon cannot be explained by a simpler model based on conservation of momentum and energy only.

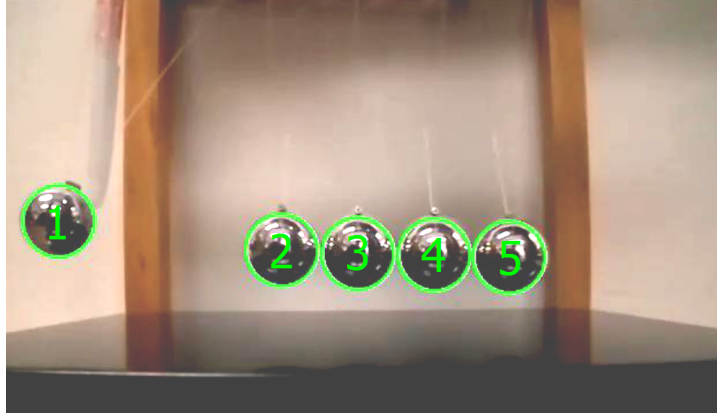


Figure 5.4 Initial State of Newton's cradle. Green circles mark the contours of the five balls, which are number 1 to 5 from left to right.

Table 5.1 Comparisons of experimental (second row) and simulation (third row) outcomes from the first collision of the five balls. Listed are the ball velocities in the  $x$ -direction.

ball	1	2	3	4	5
$v_x$	-0.0578	-0.0224	0.0003	0.1322	0.4508
$\tilde{v}_x$	-0.0568	-0.0380	-0.0002	0.1450	0.4401

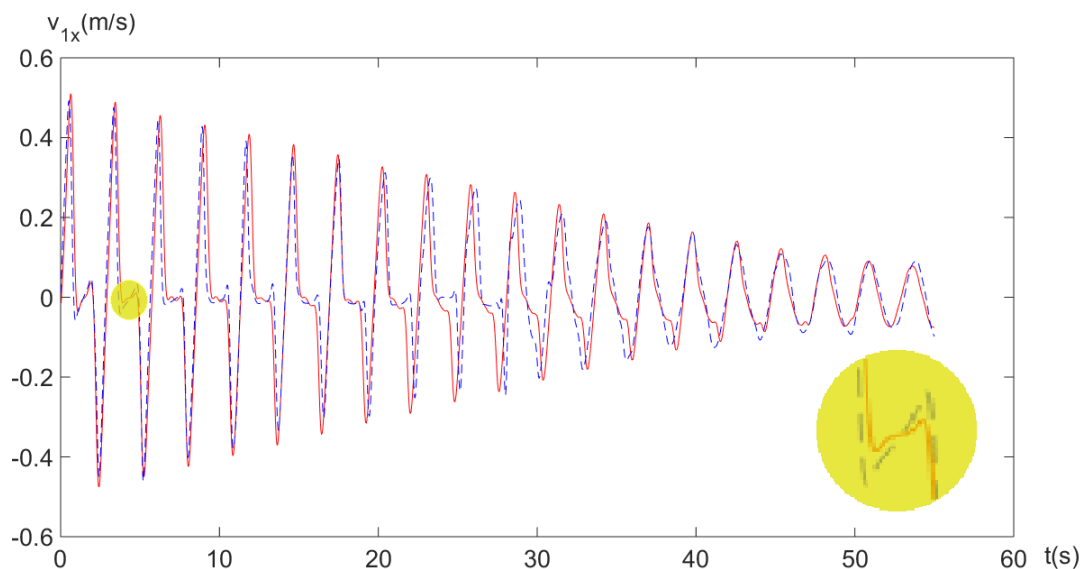


Figure 5.5 Comparison of Newton's cradle. Time trajectories of the horizontal velocity of Newton's cradle: experiment (red line) vs. simulation (blue dashed line).

The experimental and simulation results are also compared along the time axis until no more impact happened and all the balls swung together. Figure 5.5 compares the time trajectories of the horizontal velocities of ball 1 observed in the experiment and predicted by simulation. The two trajectories match very well, except that during each cycle (shown in the inset) the ball velocity fluctuates slightly more in simulation than in the experiment. This is mainly due to some sticking effect between the balls in the experiment that is not modeled by Algorithm 5.

### 5.3.2 Billiard Break Shots

Nine-ball break shots are a good testbed for Algorithm 6 described in Section 5.2. There are ten identical balls (including a cue ball) on the pool table with radius  $r$  and mass  $m$ . The cue stick shoots the cue ball to generate initial velocity  $\mathbf{v}_0$  and angular velocity  $\boldsymbol{\omega}_0$ . The initial configuration is shown in Figure 5.6. The coefficient of friction between any two balls is the same, and denoted as  $\mu_{bb}$ . Friction between a ball and the table is ignored during the impact. After the shot, the balls will be moving under sliding

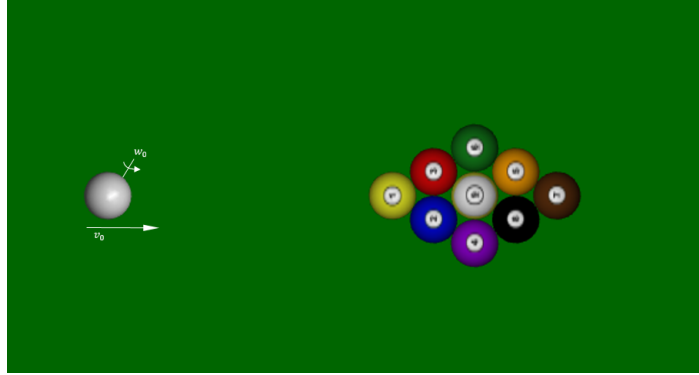


Figure 5.6 Initial state of nine-ball break shot.

or rolling friction with the table. Let  $\mu_{bt}$  and  $\tilde{\mu}_{bt}$  be the coefficients of sliding and rolling friction. We applied the technique in (19) to compute the trajectories of the balls with given velocities and angular velocities in our simulation.

Algorithm 6 is implemented to simulate break shots with parameters listed in Table 5.2. Figure 5.7 compares the final configurations following three different shots at the cue ball: stop shot, follow shot and draw shot. Immediately after each shot, the cue ball gains the same initial velocity  $(1, 0, 0)$ , but angular velocities  $(0, 0, 0)$ ,  $(0, 20, 0)$ , and  $(0, -20, 0)$ , respectively. The results show that compared to a stop shot, the balls tend to spread out more under a follow shot and less under a draw shot.

Table 5.2 Parameters used for modeling break shots include  $d_b$ : the diameter of the balls;  $m_b$ , the mass of the balls;  $\mu_{bb}$ , the ball-ball coefficient of friction;  $e_{bb}$ , the ball coefficient of restitution;  $\mu_{bt}$ , the ball-table coefficient of friction; and  $\tilde{\mu}_{bt}$ , the ball-table coefficient of rolling resistance.

$d_b$ (m)	$m_b$ (kg)	$\mu_{bb}$	$e_{bb}$	$\mu_{bt}$	$\tilde{\mu}_{bt}$
0.06	0.17	0.03	0.96	0.2	0.01

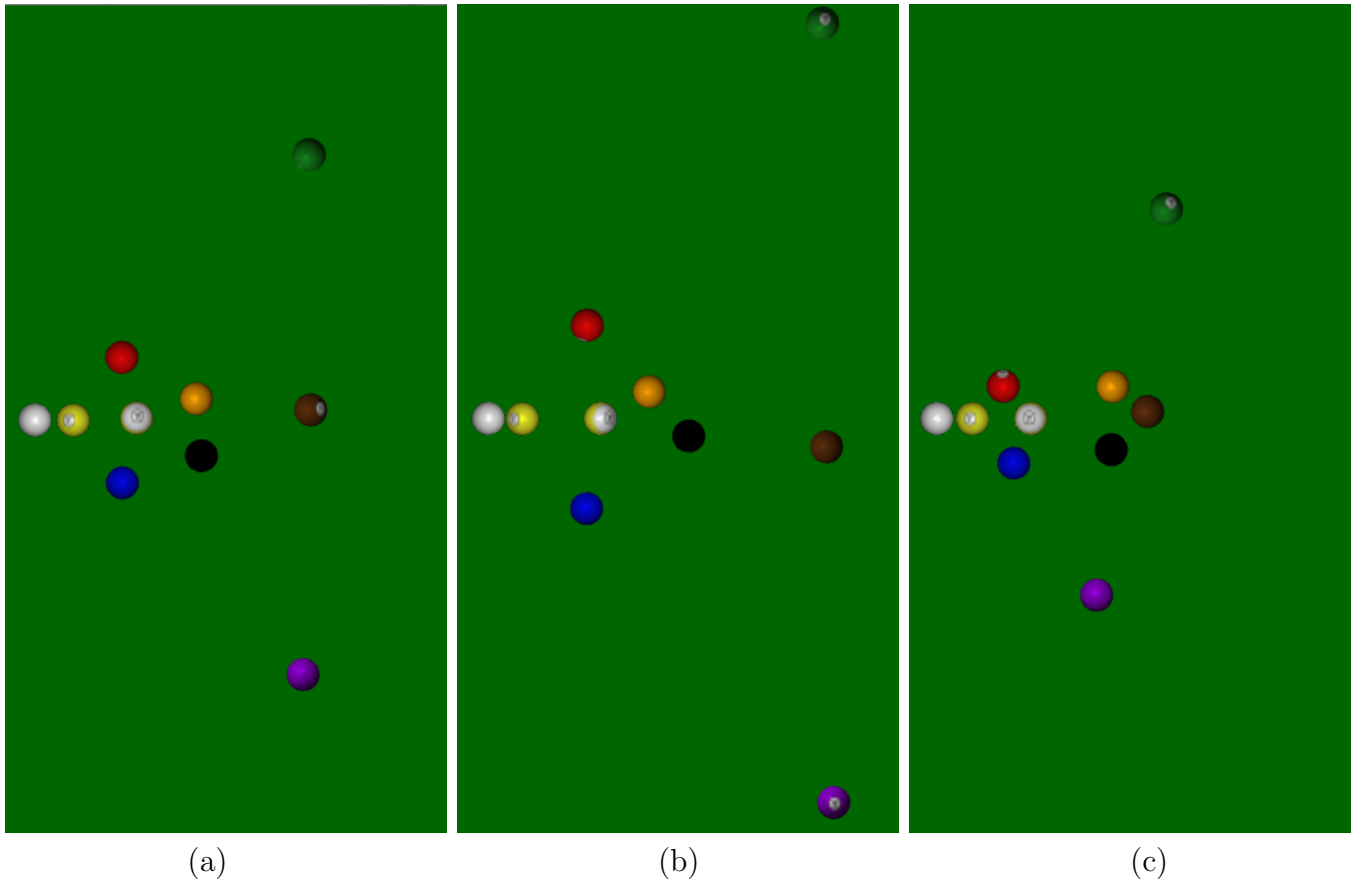


Figure 5.7 Resting configurations of ten balls (leftmost one being the cue ball) after three break shots: (a) stop shot, (b) follow shot, and (c) draw shot.



## CHAPTER 6. BATTING A FLYING OBJECT TO TARGET

In this chapter we will first describe the task of planning the motion of a flying object using a manipulator to bat it. Then we will move on to study the 2D case of planning the destination of the flying object using a manipulator with or without friction. Finally, we extend the motion planning results to 3D.

### 6.1 Task Description

In this task, a robotic manipulator with mass  $m_b$  is controlled to hit an object and alter its trajectory such that it will reach some target destination, say, a container. As shown in Fig. 6.1, the flying object with mass  $m_o$  needs to reach the target located at  $\mathbf{q}$ . We make the following assumptions:

a) The impact configuration has been pre-planned. In other words, the positions and orientations of the manipulator and the object at the moment of impact are known.

b) The object's velocity  $\mathbf{V}_o^-$  and angular velocity  $\boldsymbol{\omega}_o^-$  just before the impact are known.

After the impact, the object at velocity  $\mathbf{V}_o^+ = \mathbf{V}_o^- + \Delta\mathbf{V}_o$  will perform a free motion under gravity. Our goal is to plan the pre-impact velocity  $\mathbf{V}_b^-$  and angular velocity  $\boldsymbol{\omega}_b^-$  of the manipulator so the object's trajectory is altered to pass by the destination  $\mathbf{q}$ .

In this section, the subscripts  $x$ ,  $y$  and  $z$  of a letter (not bolded) represent the  $x$ -,  $y$ - and  $z$ -coordinates (or components) of a point (or vector) named by the same letter (bolded), respectively. For instance,  $q_x$  denotes the  $x$ -coordinate of a point  $\mathbf{q}$ , while  $V_{ox}$

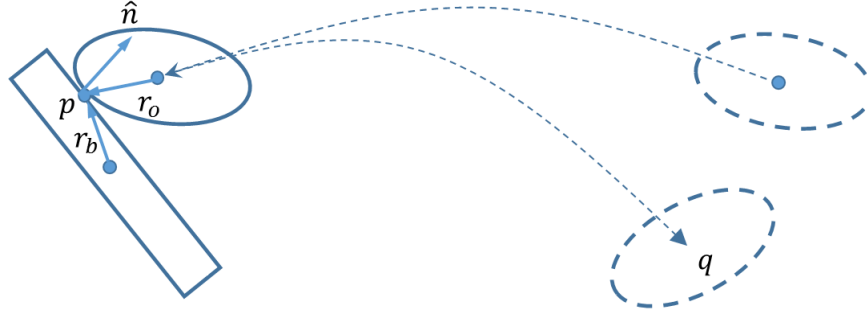


Figure 6.1 Batting an object to a target destination.

the  $x$ -component of a velocity  $\mathbf{V}_o$ .

## 6.2 Two-Dimensional Frictionless Impact Planning

In this section we first consider the planning task in 2D plane and assume that there is no friction between the manipulator and the object during the impact.

### 6.2.1 Impact Dynamics and Contact Kinematics

Let  $\mathbf{I}$  be the impulse exerted by the manipulator onto the object. An opposite impulse  $-\mathbf{I}$  is exerted on the manipulator by the object under Newton's third law. Denote by  $\mathbf{V}_b$  and  $\mathbf{V}_o$ , the velocities of the manipulator and the object, respectively, and by  $\omega_b$  and  $\omega_o$  their angular velocities. From (20) we know that the changes in their velocities during the impact are

$$\begin{aligned} \Delta \mathbf{V}_o &= \frac{1}{m_o} \mathbf{I}, & \Delta \omega_o &= \frac{1}{m_o \rho_o^2} \mathbf{r}_o \times \mathbf{I}, \\ \Delta \mathbf{V}_b &= -\frac{1}{m_b} \mathbf{I}, & \Delta \omega_b &= -\frac{1}{m_b \rho_b^2} \mathbf{r}_b \times \mathbf{I}, \end{aligned} \quad (6.1)$$

where  $\rho_b, \rho_o$  are the radii of gyration for the manipulator and object, respectively. As in Fig. 6.1,  $\mathbf{r}_i = (r_{ix}, r_{iy})^T$ ,  $i = b, o$ , are the vectors from the manipulator's and the object's centers of mass to the impact point  $\mathbf{p}$ . Let  $\mathbf{r}_{i\perp} = (-r_{iy}, r_{ix})^T$ ,  $i = b, o$ , be the vectors

perpendicular to  $\mathbf{r}_i$ . Let  $\mathbf{v}_b$  and  $\mathbf{v}_o$  be the velocities of the two points on the manipulator and the object, respectively, which coincide at the contact. We then have

$$\mathbf{v}_b = \mathbf{V}_b + \omega_b \mathbf{r}_{b\perp},$$

$$\mathbf{v}_o = \mathbf{V}_o + \omega_o \mathbf{r}_{o\perp}.$$

Then the contact velocity of the object relative to the manipulator at  $\mathbf{p}$  is

$$\mathbf{v} = \mathbf{V}_o + \omega_o \mathbf{r}_{o\perp} - \mathbf{V}_b - \omega_b \mathbf{r}_{b\perp}.$$

During the impact, it changes by the amount

$$\begin{aligned} \Delta \mathbf{v} &= \Delta \mathbf{V}_o + \Delta \omega_o \mathbf{r}_{o\perp} - \Delta \mathbf{V}_b - \Delta \omega_b \mathbf{r}_{b\perp} \\ &= \frac{1}{m_o} \mathbf{I} + \left( \frac{1}{m_o \rho_o^2} \mathbf{r}_o \times \mathbf{I} \right) \mathbf{r}_{o\perp} + \frac{1}{m_b} \mathbf{I} + \left( \frac{1}{m_b \rho_b^2} \mathbf{r}_b \times \mathbf{I} \right) \mathbf{r}_{b\perp} \\ &= \left( \frac{1}{m_o} + \frac{1}{m_b} \right) \mathbf{I} + \left( \frac{1}{m_o \rho_o^2} \mathbf{r}_{o\perp} \cdot \mathbf{r}_{o\perp}^T + \frac{1}{m_b \rho_b^2} \mathbf{r}_{b\perp} \cdot \mathbf{r}_{b\perp}^T \right) \mathbf{I} \\ &= \left( \left( \frac{1}{m_o} + \frac{1}{m_b} \right) \begin{pmatrix} 1 & 0 \\ 0 & 1 \end{pmatrix} + \frac{1}{m_o \rho_o^2} \mathbf{r}_{o\perp} \cdot \mathbf{r}_{o\perp}^T + \frac{1}{m_b \rho_b^2} \mathbf{r}_{b\perp} \cdot \mathbf{r}_{b\perp}^T \right) \mathbf{I} \\ &= S \mathbf{I}, \end{aligned}$$

where

$$S = \left( \frac{1}{m_o} + \frac{1}{m_b} \right) \begin{pmatrix} 1 & 0 \\ 0 & 1 \end{pmatrix} + \frac{1}{m_o \rho_o^2} \mathbf{r}_{o\perp} \cdot \mathbf{r}_{o\perp}^T + \frac{1}{m_b \rho_b^2} \mathbf{r}_{b\perp} \cdot \mathbf{r}_{b\perp}^T.$$

The impact can be divided into two stages (34, p. 212): compression and restitution. During compression, the kinetic energy is transformed into the potential energy stored at the contact. When compression ends, the energy reaches its maximum value  $E_{\max}$ . At this moment, the velocity becomes zero. During restitution, the elastic portion of the stored energy  $e^2 E_{\max}$  is released. Here  $e$ ,  $0 \leq e \leq 1$ , is the energy coefficient of restitution.

We apply an explanation from (54) for the energy loss. When compression ends the virtual spring stiffness suddenly increases by a factor of  $1/e^2$ . Under force continuity, simultaneously the change in length of the spring reduces to a fraction  $e^2$  of its previous value.

Absence of friction means that there is no impulse or energy exchange along the tangent direction. Given the one-to-one correspondence between impulse and time, energy  $E$  can be described as a function of impulse. This function has zero values at the start and the end of the impact, and its only discontinuity occurs at the end of compression (due to deformation, heat, etc.). It is differentiable during each impact phase:

$$\begin{aligned}
\frac{dE}{dI} &= -\dot{x} \\
&= -\mathbf{v} \cdot \hat{\mathbf{n}} \\
&= -(\mathbf{v}^- + \Delta\mathbf{v}) \cdot \hat{\mathbf{n}} \\
&= -\mathbf{v}^- \cdot \hat{\mathbf{n}} - (S\mathbf{I}) \cdot \hat{\mathbf{n}} \\
&= -v_n^- - \hat{\mathbf{n}}^T S \hat{\mathbf{n}} I,
\end{aligned} \tag{6.2}$$

where  $\mathbf{v}^- = \mathbf{V}_o^- + \omega_o^- \mathbf{r}_{o\perp} - \mathbf{V}_b^- - \omega_b^- \mathbf{r}_{b\perp}$  is the contact velocity before impact,  $v_n^-$  is the contact velocity along the normal direction before impact, and  $I = \|\mathbf{I}\|$ . Note that here  $\mathbf{I}$  is along the direction of  $\hat{\mathbf{n}}$ .

Denote  $I_c$  as the impulse at the end of compression, and  $I_r$  as the impulse at the end of restitution, which is the total impulse of the impact. At the end of compression, we have

$$\frac{dE}{dI} = 0. \tag{6.3}$$

Substitute (6.2) into (6.3),

$$I_c = -\frac{v_n^-}{\hat{\mathbf{n}}^T S \hat{\mathbf{n}}}.$$

Integrate (6.2) from 0 to  $I_c$ :

$$E_{\max} = \frac{(v_n^-)^2}{2\hat{\mathbf{n}}^T S \hat{\mathbf{n}}}. \tag{6.4}$$

When compression ends, the energy suddenly decreases from  $E_{\max}$  to  $e^2 E_{\max}$ . During restitution, the energy will decrease to zero. Thus we have

$$-e^2 E_{\max} = \int_{I_c}^{I_r} dE. \quad (6.5)$$

Solving  $I_r$  from (6.4) and (6.5), we obtain

$$I_r = -\frac{(1+e)(\mathbf{v}^- \cdot \hat{\mathbf{n}})}{\hat{\mathbf{n}}^T S \hat{\mathbf{n}}} = -\frac{(1+e)v_n^-}{\hat{\mathbf{n}}^T S \hat{\mathbf{n}}}. \quad (6.6)$$

### 6.2.2 Motion Planning

With the outcome of impact available, we are ready to plan the motion of the flying object. Without loss of generality, we put the origin at the impact point  $\mathbf{p}$ , and assume that the manipulator is batting the object rightward, i.e.,  $n_x > 0$  in  $\hat{\mathbf{n}} = (n_x, n_y)^T$ . From (6.1) and (6.6),

$$\begin{aligned} \Delta \mathbf{V}_o &= \frac{I_r}{m_o} \cdot \hat{\mathbf{n}} \\ &= -\frac{(1+e)(\mathbf{v}^- \cdot \hat{\mathbf{n}})}{m_o \hat{\mathbf{n}}^T S \hat{\mathbf{n}}} \cdot \hat{\mathbf{n}} \\ &= -\frac{(1+e)(v_{on}^- - v_{bn}^-)}{m_o \hat{\mathbf{n}}^T S \hat{\mathbf{n}}} \cdot \hat{\mathbf{n}}, \end{aligned} \quad (6.7)$$

where  $v_{on}^- = \mathbf{v}_o^- \cdot \hat{\mathbf{n}}$  and  $v_{bn}^- = \mathbf{v}_b^- \cdot \hat{\mathbf{n}}$ . Notice that other components of  $\mathbf{v}_b$  will not affect the behavior of the object after impact. Next we consider  $v_{bn}^-$  as the only variable since other terms in (6.7) are known. In order for the impact to happen,  $v_{bn}^- \geq v_{on}^-$ . From (6.7), the velocity of the object after impact is given by

$$\begin{aligned} \mathbf{V}_o^+ &= \mathbf{V}_o^- + \Delta \mathbf{V}_o \\ &= \mathbf{V}_o^- - \frac{(1+e)(v_{on}^- - v_{bn}^-)}{m_o \hat{\mathbf{n}}^T S \hat{\mathbf{n}}} \cdot \hat{\mathbf{n}}. \end{aligned} \quad (6.8)$$

For the object to pass through  $\mathbf{q}$ , it needs to satisfy the kinematic equations:

$$\mathbf{q} + \mathbf{r}_o = \mathbf{V}_o^+ t - (0, 0.5g)^T t^2, \quad (6.9)$$

for some flying time  $t$ , where  $g$  is the gravitational acceleration. Eliminating  $t$ , we obtain an equation involving the  $x$ - and  $y$ -components of  $\mathbf{V}_o^+$ ,  $\mathbf{q}$ , and  $\mathbf{r}_o$ ,

$$(V_{ox}^+)^2(q_y + r_{oy}) = V_{ox}^+ V_{oy}^+(q_x + r_{ox}) - 0.5g(q_x + r_{ox})^2. \quad (6.10)$$

Given a target  $\mathbf{q}$  and impact normal, we can solve the quadratic equation (6.10) to obtain the pre-impact velocity of the manipulator.

### 6.2.3 Reachable Region

To fully understand the problem, given  $\mathbf{V}_o^- = (V_{ox}^-, V_{oy}^-)^T$ ,  $\omega_o^-$ , and  $\hat{\mathbf{n}}$ , we will determine the region of the positions of  $\mathbf{q} = (q_x, q_y)^T$  reachable by the object's center of mass. The trajectory is determined by the normal velocity  $v_{bn}^-$  of contact on the manipulator. The point  $\mathbf{q}$ , if on the monotonic trajectory, has its  $y$ -coordinate depending on its  $x$ -coordinate and  $v_{bn}^-$ . We write  $q_y(v_{bn}^-, q_x)$ .

There are four cases separated by the signs of  $V_{ox}^-$  and  $\mathbf{V}_o^- \times \hat{\mathbf{n}}$ :

Case 1:  $V_{ox}^- > 0$ ,  $\mathbf{V}_o^- \times \hat{\mathbf{n}} \geq 0$ .

Case 2:  $V_{ox}^- > 0$ ,  $\mathbf{V}_o^- \times \hat{\mathbf{n}} < 0$ .

Case 3:  $V_{ox}^- \leq 0$ ,  $\mathbf{V}_o^- \times \hat{\mathbf{n}} \geq 0$ .

Case 4:  $V_{ox}^- \leq 0$ ,  $\mathbf{V}_o^- \times \hat{\mathbf{n}} < 0$ .

**Proposition 1.** *In Case 1,*

$$q_y(v_{on}^-, q_x) \leq q_y \leq q_y(+\infty, q_x),$$

where

$$q_y(v_{on}^-, q_x) = \frac{V_{ox}^- V_{oy}^- (q_x + r_{ox}) - 0.5g(q_x + r_{ox})^2}{V_{ox}^{-2}} - r_{oy}, \quad (6.11)$$

$$q_y(+\infty, q_x) = \frac{n_y}{n_x}(q_x + r_{ox}) - r_{oy}. \quad (6.12)$$

*Proof.* From (6.8), differentiate  $V_{ox}^+$  with respect to  $v_{bn}^-$ ,

$$V_{ox}^{+'}(v_{bn}^-) = \frac{dV_{ox}^+}{dv_{bn}^-} = \frac{(1+e)n_x}{m_o \hat{\mathbf{n}}^T S \hat{\mathbf{n}}}. \quad (6.13)$$

It is trivial to show that  $\hat{\mathbf{n}}^T S \hat{\mathbf{n}} > 0$ , which, coupled with  $n_x > 0$ , implies that  $V_{ox}^{+'}(v_{bn}^-) > 0$ . Thus,  $V_{ox}^+$  is linear in  $v_{bn}^-$  and monotonically increasing with  $v_{bn}^-$ . Since  $v_{bn}^- \geq v_{on}^-$ , we have

$$V_{ox}^+(v_{bn}^-) \geq V_{ox}^+(v_{on}^-) = V_{ox}^- > 0.$$

And also, from (6.9),

$$q_x + r_{ox} = V_{ox}^+ t > 0,$$

when  $t > 0$  (impact happens at  $t = 0$ ). Since  $V_{ox}^+ > 0$ , we obtain (6.12) from (6.10).

Take the partial derivative of  $q_y$  with respect to  $v_{bn}^-$ , substituting (6.13) in:

$$\frac{\partial q_y}{\partial v_{bn}^-} = \frac{1+e}{m_o \hat{\mathbf{n}}^T S \hat{\mathbf{n}}} \left( \frac{(q_x + r_{ox})(\mathbf{V}_o^- \times \hat{\mathbf{n}})}{V_{ox}^{+2}} + \frac{gn_x(q_x + r_{ox})^2}{V_{ox}^{+3}} \right). \quad (6.14)$$

The first and second terms on the right-hand side are both greater than 0 for  $v_{bn}^- \geq v_{on}^-$ , which means  $\partial q_y / \partial v_{bn}^- > 0$ . Thus, the lower bound of  $q_y$  is  $q_y(v_{on}^-, q_x)$  given in (6.12).

The upper bound is

$$\begin{aligned} q_y(+\infty, q_x) &= \lim_{v_{bn}^- \rightarrow +\infty} q_y \\ &= \lim_{v_{bn}^- \rightarrow +\infty} \frac{V_{ox}^+ V_{oy}^+ (q_x + r_{ox}) - 0.5g(q_x + r_{ox})^2}{V_{ox}^{+2}} - r_{oy} \\ &= \lim_{v_{bn}^- \rightarrow +\infty} \frac{n_y}{n_x} (q_x + r_{ox}) - r_{oy} \\ &= \frac{n_y}{n_x} (q_x + r_{ox}) - r_{oy}. \end{aligned}$$

□

Fig. 6.2(a) shows the reachable region for Case 1.

**Proposition 2.** In Case 2, let  $\rho = -\frac{V_{ox}^-(\mathbf{V}_o^- \times \hat{\mathbf{n}})}{gn_x}$ . The reachable region is

$$\left\{ \begin{array}{ll} q_y(+\infty, q_x) < q_y \leq q_y(v_{on}^-, q_x), & \text{if } 0 \leq q_x + r_{ox} < \rho, \\ q_y(+\infty, q_x) < q_y \leq q_y(v_{bn}^{-*}, q_x), & \text{if } \rho \leq q_x + r_{ox} \leq 2\rho, \\ q_y(v_{on}^-, q_x) \leq q_y \leq q_y(v_{bn}^{-*}, q_x), & \text{if } q_x + r_{ox} > 2\rho, \end{array} \right. \quad (6.15)$$

where

$$v_{bn}^{-*} = v_{on}^- - \frac{m_o \hat{\mathbf{n}}^T S \hat{\mathbf{n}}}{(1+e)} \left( \frac{V_{ox}^-}{n_x} + \frac{g(q_x + r_{ox})}{\mathbf{V}_o^- \times \hat{\mathbf{n}}} \right). \quad (6.16)$$

*Proof.* As in the proof of Proposition 1,  $V_{ox}^+ > 0$  and  $q_x > 0$  still hold when  $t > 0$ . However, since  $\mathbf{V}_o^- \times \hat{\mathbf{n}} < 0$ , the first term on the right-hand side of (6.14) is not always positive for  $v_{bn}^- \geq v_{on}^-$ , which means that an optimal point exists for the function  $q_y(v_{bn}^-)$ . To obtain the optimal point, we solve  $\partial q_y / \partial v_{bn}^- = 0$  and get (6.16). To decide whether  $v_{bn}^{-*}$  is a maximum or minimum point, we look at the second partial derivative of  $q_y$ :

$$\frac{\partial^2 q_y}{\partial v_{bn}^{-2}} = \left( \frac{1+e}{m_o \hat{\mathbf{n}}^T S \hat{\mathbf{n}}} \right)^2 \left( -\frac{2n_x(q_x + r_{ox})(\mathbf{V}_o^- \times \hat{\mathbf{n}})}{V_{ox}^{+3}} - \frac{3gn_x^2(q_x + r_{ox})^2}{V_{ox}^{+4}} \right). \quad (6.17)$$

And also,

$$V_{ox}^+(v_{bn}^{-*}) = -\frac{gn_x(q_x + r_{ox})}{\mathbf{V}_o^- \times \hat{\mathbf{n}}}. \quad (6.18)$$

Substitute (6.18) into (6.17),

$$\frac{\partial^2 q_y}{\partial v_{bn}^{-2}} = \left( \frac{1+e}{m_o \hat{\mathbf{n}}^T S \hat{\mathbf{n}}} \right)^2 \frac{n_x(q_x + r_{ox})(\mathbf{V}_o^- \times \hat{\mathbf{n}})}{V_{ox}^{+3}} < 0.$$

Thus,  $v_{bn}^{-*}$  is a maximum point.

When  $V_{ox}^-/n_x + g(q_x + r_{ox})/(\mathbf{V}_o^- \times \hat{\mathbf{n}}) > 0$ , i.e.,  $0 < q_x + r_{ox} < \rho$ , we have  $v_{bn}^{-*} < v_{on}^-$ . Since  $v_{bn}^{-*}$  is a maximum point, it can be inferred that  $q_y$  is monotonically decreasing for  $v_{bn}^- > v_{on}^-$ . Thus, the lower bound is (6.12), while the upper bound is (6.12).

When  $V_{ox}^-/n_x + g(q_x + r_{ox})/(\mathbf{V}_o^- \times \hat{\mathbf{n}}) \leq 0$  we can get  $v_{bn}^{-*} \geq v_{on}^-$ . Since  $v_{bn}^{-*}$  is a maximum point, the upper bound is

$$q_y(v_{bn}^{-*}, q_x) = \frac{n_y}{n_x}(q_x + r_{ox}) + \frac{(\mathbf{V}_o^- \times \hat{\mathbf{n}})^2}{2gn_x^2} - r_{oy}.$$



And the lower bound is the minimum of (6.12) and (6.12). To find  $q_x$  of division, let  $q_y(v_{on}^-, q_x) = q_y(+\infty, q_x)$ , which leads to

$$q_x^* = -\frac{2V_{ox}^-(\mathbf{V}_o^- \times \hat{\mathbf{n}})}{gn_x} - r_{ox}.$$

It can be easily shown that when  $q_x \geq q_x^*$ ,  $q_y(v_{on}^-, q_x) \leq q_y(+\infty, q_x)$ , thus the lower bound is  $q_y(v_{on}^-, q_x)$ . Otherwise, it is  $q_y(+\infty, q_x)$ .

To sum up, in Case 2, the reachable region is (6.15).  $\square$

The reachable region for Case 2 is shown in Fig. 6.2(b).

**Proposition 3.** *In Cases 3 and 4, the reachable regions in these two cases are respectively*

$$\begin{cases} q_y < q_y(+\infty, q_x), & \text{if } q_x + r_{ox} > 0, \\ q_y \leq q_y(v_{on}^-, q_x), & \text{if } q_x + r_{ox} \leq 0, \end{cases} \quad (6.19)$$

and

$$\begin{cases} q_y < q_y(v_{on}^-, q_x), & \text{if } q_x + r_{ox} < \rho, \\ q_y \leq q_y(v_{bn}^{*-}, q_x), & \text{if } q_x + r_{ox} \geq \rho. \end{cases} \quad (6.20)$$

*Proof.* For Case 3, we first consider the scenario when  $q_x + r_{ox} \geq 0$ , which implies  $V_{ox}^+ > 0$ . From (6.14), we know that  $\partial q_y / \partial v_{bn}^- > 0$ , in other words,  $q_y$  is monotonically increasing. From  $V_{ox}^+ > 0$ , we can obtain

$$v_{bn}^- > v_{bn}^{*-} > v_{on}^-,$$

where

$$v_{bn}^{*-} = -\frac{m_o \hat{\mathbf{n}}^T S \hat{\mathbf{n}}}{(1+e)n_x} V_{ox}^- + v_{on}^-.$$

Then for  $v_{bn}^- > v_{bn}^{*-}$ , the lower bound is

$$\begin{aligned} q_y(v_{bn}^{*-}, q_x) &= \lim_{V_{ox}^+ \rightarrow 0} \frac{V_{ox}^+ V_{oy}^+(q_x + r_{ox}) - 0.5g(q_x + r_{ox})^2}{V_{ox}^{+2}} - r_{oy} \\ &= -\infty. \end{aligned} \quad (6.21)$$

And the upper bound is given in (6.12).

Next when  $q_x + r_{ox} \leq 0$ , which leads to  $V_{ox}^+ \leq 0$  and  $\partial q_y / \partial v_{bn}^- \leq 0$ ,  $q_y$  is monotonically decreasing for  $v_{bn}^- \in [v_{on}^-, v_{bn}^{**}]$ . The lower bound is  $-\infty$ , while the upper bound is given in (6.12). Therefore, in Case 3, the reachable region is (6.19).

In Case 4, similar to Case 3, we first consider  $q_x + r_{ox} > 0$ , which implies  $V_{ox}^+ > 0$ , and  $v_{bn}^- > v_{bn}^{**}$ . However, since  $\partial q_y / \partial v_{bn}^-$  is no longer positive. From (6.16) we have  $v_{bn}^* > v_{bn}^{**}$ , which means that the optimal point of  $q_y$  will be reached. Also, from (6.17) we can infer that  $v_{bn}^*$  is a maximum point. Therefore, the upper bound is  $q_y(v_{bn}^*, q_x)$ , and the lower bound is the minimum of (6.21) and (6.12), which is  $-\infty$ .

When  $q_x + r_{ox} < 0$ , we have  $V_{ox}^+ < 0$ , and  $v_{on}^- \leq v_{bn}^- \leq v_{bn}^{**}$ . Performing similar analysis as in Proposition 2, it can be shown that the reachable region is

$$\begin{cases} q_y < q_y(v_{on}^-, q_x), & \text{if } q_x + r_{ox} < \rho, \\ q_y \leq q_y(v_{bn}^*, q_x), & \text{if } \rho \leq q_x + r_{ox} < 0. \end{cases}$$

For the simple case when  $q_x + r_{ox} = 0$ , if  $t = 0$ , then it is just the starting point at the origin. Otherwise,  $v_{ox} = 0$ . It is trivial to show that the upper bound is  $(\mathbf{V}_o^- \times \hat{\mathbf{n}})^2 / (2gn_x^2) - r_{oy}$ , and lower bound is  $-\infty$ .

Combine the above results, in Case 4 the reachable region is (6.20).  $\square$

Fig. 6.2(c) and (d) list the reachable regions (gray areas) in Cases 3 and 4, respectively.

## 6.2.4 Simulation and Experiment

This section presents an experiment with the planning strategy in the absence of friction described above, and compares the results with simulation.

In the experiment a  $2\frac{1}{2}$ D hexagonal, styrofoam object was thrown in the 2D plane towards a 4-DOF Barrett Technology WAM arm. Batting was performed using one joint in the same plane, with a wooden paddle attached as the end effector. A stationary, circular object was placed 1.5 away from the robot to serve as the target destination. The object had mass 0.0121 and included two line features in a ‘‘T’’ shape to uniquely

determine its orientation. It was thrown from 2.4 away at velocity 3.9 and angular velocity  $-21$ . The paddle had velocity 2.4. The energetic coefficient of restitution between the paddle and the object is 0.95. The sequence was captured at 196fps by a 2.2 megapixel Ximea xIQ color camera. Images were then processed using the Hough Line Transform algorithm (10) to fit the line features of the object.

To validate frictionless impact planning, accurate estimates of linear and angular velocity are required. Because the object had uniform mass distribution, there was no angular acceleration. Thus, the polar angle of the “T” shape was calculated, and the angular velocity was approximated by averaging the values across all frames. For position, when calculating linear velocity with a small time step between frames, noise grows significantly and produces erroneous values. To counter this, a Kalman filter was applied to reduce the affect of the noise that accumulated. The filter predicted the position and velocity at each frame using kinematics, and corrected them using the values obtained from image processing. Fig. 6.3 shows how the measurement noise from image processing is reduced over time for the estimate. It results in a smoothed estimate that accounts for air resistance by fitting the noisy data.

In simulation, we take the average of the velocities before impact and model the trajectory as a free motion. Fig. 6.4 compares the experimental and simulation results with the object for each of 8 consecutive frames. In the figure, the pre-impact trajectory of the object is shown as (a) in experiment, and (b) in simulation, while its post-impact trajectory is presented in (c) and (d). We can see that the trajectories match pretty closely. We compare errors in terms of the magnitude of position and orientation of the object with each frame as shown in Fig. 6.5. The average difference through the whole process is 0.0154 in position, and 0.0393 in orientation. The error in position was mainly due to air resistance on the object in the experiment, while the error in orientation was due to some frames being blurry.

## 6.3 Two-Dimensional Frictional Impact Planning

### 6.3.1 Impact Dynamics and Contact Kinematics

In this section we look at the scenario with friction. Suppose  $\hat{\mathbf{u}} = (n_y, -n_x)^T$  is the unit vector orthogonal to  $\hat{\mathbf{n}}$ . Also, we represent  $S = \begin{pmatrix} S_{11} & S_{12} \\ S_{12} & S_{22} \end{pmatrix}$  since  $S_{12} = S_{21}$ . Since friction is taken into account, we need to consider both normal impulse  $I_n$  and tangential impulse  $I_\perp$  during impact. Let  $\mu$  be the coefficient of friction between the objects. Equation (6.2) becomes

$$\begin{aligned}
 \frac{dE}{dI_n} &= -\mathbf{v}^- \cdot \hat{\mathbf{n}} - (S\mathbf{I}) \cdot \hat{\mathbf{n}} \\
 &= -\mathbf{v}^- \cdot \hat{\mathbf{n}} - \hat{\mathbf{n}}^T S \hat{\mathbf{u}} I_\perp - \hat{\mathbf{n}}^T S \hat{\mathbf{n}} I_n, \\
 &= -v_n^- - (\chi \hat{\mathbf{n}}^T S \hat{\mathbf{u}} + \hat{\mathbf{n}}^T S \hat{\mathbf{n}}) I_n, \\
 &= -v_n^- - S_{12} I_\perp - S_{22} I_n, \\
 &= -v_n^- - (\chi S_{12} + S_{22}) I_n.
 \end{aligned} \tag{6.22}$$

where  $\chi = \pm\mu$  if the contact is sliding, with the sign decided by the direction of tangential contact velocity. When the contact is sticking,  $\chi$  is the ratio, denoted  $\chi_s$ , of the derivatives of tangential and normal impulse at the moment.

From (61) for planar two rigid-body impact five contact modes may happen: (1) sliding, (2) sticking in compression phase (C-sticking), (3) sticking in the restitution phase (R-sticking), (4) reverse sliding in compression phase (CR-sliding), (5) reverse sliding in restitution phase (RR-sliding). Denote by  $I_{ns}$  the value of normal impulse when sliding ends, by  $I_{nc}$  when compression ends, and by  $I_{nr}$  when restitution ends which is the total impulse for the impact. When sliding stops, the relative contact velocity along the tangent direction should be zero, i.e.  $(\mathbf{v}^- + \Delta\mathbf{v}) \cdot \hat{\mathbf{u}} = 0$ . Solve this equation:

Table 6.1 Contact modes of impact.

	$ \chi_s  < \mu$	$ \chi_s  > \mu$
$I_{nc} < I_{nr} \leq I_{ns}$	sliding	sliding
$I_{ns} < I_{nc} < I_{nr}$	C-sticking	CR-sliding
$I_{nc} \leq I_{ns} < I_{nr}$	R-sticking	RR-sliding

$$I_{ns} = -\frac{\hat{\mathbf{u}}^T \mathbf{v}^-}{\hat{\mathbf{u}}^T S(-s\mu\hat{\mathbf{u}} + \hat{\mathbf{n}})}, \quad (6.23)$$

where  $s = v_{\perp}^-/|v_{\perp}^-|$  gives the sign of the tangent relative contact velocity. Suppose that sticking happens right after sliding ends, we have

$$\frac{dv_{\perp}}{dI_n} = 0. \quad (6.24)$$

Solve (6.24) to obtain

$$\chi_s = -\frac{\hat{\mathbf{u}}^T S \hat{\mathbf{n}}}{\hat{\mathbf{u}}^T S \hat{\mathbf{u}}},$$

which is a constant. Thus, if  $|\chi_s| < \mu$ , friction is able to prevent sliding, and the contact will stick for the rest of the impact. Otherwise, reverse sliding happens, and  $\chi = s\mu$  in this case. All the contact modes of the impact can be summarized in Table 6.1.

To simplify the derivation and without loss of generality, we re-orient the coordinate frame such that the  $y$ -axis is along the contact normal, i.e.  $\hat{\mathbf{n}} = \hat{\mathbf{y}} = (0, 1)^T$ . Consequently,  $\hat{\mathbf{u}} = \hat{\mathbf{x}} = (1, 0)^T$ . In the sliding mode, similar to the frictionless case, it can be shown that the total normal impulse is

$$I_{yr} = -\frac{(1+e)v_y^-}{\hat{\mathbf{y}}^T S(-s\mu\hat{\mathbf{x}} + \hat{\mathbf{y}})} = -\frac{(1+e)v_y^-}{-s\mu S_{12} + S_{22}}.$$

And the total tangent impulse  $I_{xr}$  is

$$I_{xr} = -s\mu I_{yr} = \frac{s\mu(1+e)v_y^-}{-s\mu S_{12} + S_{22}}.$$

In the compression-sticking mode, sliding stops before compression ends. Thus, when  $I_y \in [0, I_{ys}]$ ,  $\chi = -s\mu$  in (6.22), while when  $I_y \in [I_{ys}, I_{yr}]$ ,

$$\begin{aligned} \frac{dE}{dI_y} &= -\mathbf{v}^- \cdot \hat{\mathbf{y}} - \hat{\mathbf{y}}^T S \hat{\mathbf{x}} I_x - \hat{\mathbf{y}}^T S \hat{\mathbf{y}} I_y \\ &= -\mathbf{v}^- \cdot \hat{\mathbf{n}} - \hat{\mathbf{n}}^T S (-s\mu I_{ns} + \chi_s (I_n - I_{ns})) \hat{\mathbf{u}} - \hat{\mathbf{n}}^T S \hat{\mathbf{n}} I_n \\ &= -v_y^- + s\mu S_{12} I_{ys} - \chi_s S_{12} (I_y - I_{ys}) - S_{22} I_y. \end{aligned} \quad (6.25)$$

Also, we know that when compression ends, the normal impulse  $I_{yc}$  satisfies  $dE/dI_n = 0$ , from which we can obtain

$$I_{yc} = \frac{-S_{11}v_y^- + S_{12}v_x^-}{-S_{12}^2 + S_{11}S_{22}}. \quad (6.26)$$

Subsequently,

$$\begin{aligned} E_{\max} &= \int_0^{I_{ys}} dE + \int_{I_{ys}}^{I_{yc}} dE \\ &= \frac{(-S_{11}v_y^- + S_{12}v_x^-)^2}{2S_{11}(S_{11}S_{22} - S_{12}^2)} + \frac{S_{12}(v_x^-)^2}{2S_{11}(-s\mu S_{11} + S_{12})}. \end{aligned} \quad (6.27)$$

Substitute (6.27) and (6.25) into (6.5), solving the quadratic equation:

$$I_{yr} = (-b - \sqrt{b^2 - 4ac})/2a,$$

where

$$\begin{aligned} a &= -\frac{1}{2} \left( -\frac{S_{12}^2}{S_{11}} + S_{22} \right), \\ b &= -v_y^- + S_{12} \left( s\mu - \frac{S_{12}}{S_{11}} \right) I_{ys}, \\ c &= \frac{1}{2} \left( (1 - e^2)v_y^- I_{yc} - e^2 \frac{S_{12}}{S_{11}} v_x^- I_{ys} - (1 - e^2) \frac{S_{12}}{S_{11}} v_x^- I_{yc} \right). \end{aligned}$$

The total tangent impulse is

$$I_{xr} = -s\mu I_{ys} + \chi_s (I_{yr} - I_{ys}).$$

Similarly, we can obtain the normal and tangential impulses for the other three contact modes. The normal impulse when sliding ends have the same form given in (6.23).

And the impulses are according to five combinations of impact phases and contact modes:

(1) sliding:

$$\begin{aligned} I_{yc} &= -\frac{v_y^-}{-s\mu S_{12} + S_{22}}, \\ I_{yr} &= -\frac{(1+e)v_y^-}{-s\mu S_{12} + S_{22}}, \\ I_{xr} &= -s\mu I_{yr}. \end{aligned} \quad (6.28)$$

(2) compression-sticking:

$$\begin{aligned} I_{yc} &= \frac{-S_{11}v_y^- + S_{12}v_x^-}{-S_{12}^2 + S_{11}S_{22}}, \\ a &= -\frac{1}{2} \left( -\frac{S_{12}^2}{S_{11}} + S_{22} \right), \\ b &= -v_y^- + S_{12} \left( s\mu - \frac{S_{12}}{S_{11}} \right) I_{ys}, \\ c &= \frac{1}{2} \left( (1-e^2)v_y^- I_{yc} - e^2 \frac{S_{12}}{S_{11}} v_x^- I_{ys} - (1-e^2) \frac{S_{12}}{S_{11}} v_x^- I_{yc} \right), \\ I_{yr} &= (-b - \sqrt{b^2 - 4ac})/2a, \\ I_{xr} &= -s\mu I_{ys} + \chi_s (I_{yr} - I_{ys}). \end{aligned} \quad (6.29)$$

(3) restitution-sticking:

$$\begin{aligned} I_{yc} &= \frac{-v_y^-}{-s\mu S_{12} + S_{22}}, \\ a &= -\frac{1}{2} \left( -\frac{S_{12}^2}{S_{11}} + S_{22} \right), \\ b &= -v_y^- + S_{12} \left( s\mu - \frac{S_{12}}{S_{11}} \right) I_{ys}, \\ c &= -\frac{1}{2} S_{12} \left( s\mu - \frac{S_{12}}{S_{11}} \right) I_{ys}^2 - \frac{(1-e^2)(v_y^-)^2}{2(-s\mu S_{12} + S_{22})}, \\ I_{yr} &= (-b - \sqrt{b^2 - 4ac})/2a, \\ I_{xr} &= -s\mu I_{ys} + \chi_s (I_{yr} - I_{ys}). \end{aligned} \quad (6.30)$$

(4) compression-reverse sliding:

$$\begin{aligned}
I_{yc} &= -\frac{1}{s\mu S_{12} + S_{22}} \left( v_y^- + \frac{2s\mu S_{12} v_x^-}{-s\mu S_{11} + S_{12}} \right), \\
a &= -\frac{1}{2} (s\mu S_{12} + S_{22}), \\
b &= -v_y^- + 2s\mu S_{12} I_{ys}, \\
c &= -(1 - e^2) \left( (-v_y^- + 2s\mu S_{12} I_{ys}) I_{yc} - \frac{1}{2} (s\mu S_{12} + S_{22}) I_{yc}^2 \right) - e^2 s\mu S_{12} I_{ys}^2, \\
I_{yr} &= (-b - \sqrt{b^2 - 4ac})/2a, \\
I_{xr} &= -2s\mu I_{ys} + s\mu I_{yr}.
\end{aligned} \tag{6.31}$$

(5) restitution-reverse sliding:

$$\begin{aligned}
I_{yc} &= \frac{-v_y^-}{-s\mu S_{12} + S_{22}}, \\
a &= -\frac{1}{2} (s\mu S_{12} + S_{22}), \\
b &= -v_y^- + 2s\mu S_{12} I_{ys}, \\
c &= -s\mu S_{12} I_{ys}^2 - \frac{(1 - e^2)(v_y^-)^2}{2(-s\mu S_{12} + S_{22})}, \\
I_{yr} &= (-b - \sqrt{b^2 - 4ac})/2a, \\
I_{xr} &= -2s\mu I_{ys} + s\mu I_{yr}.
\end{aligned} \tag{6.32}$$

Given the total normal and tangential impulses in all contact modes, we can compute the post-impact velocity  $\mathbf{V}_o^+$  and angular velocity  $\omega_o^+$  of the object.

### 6.3.2 Impact planing

In order to perform motion planning for the object to reach the destination  $\mathbf{q}$ , we can choose the direction of the manipulator that hits the object. With a fixed hitting direction, there are two degrees of freedom we can control before impact. They are the tangent and normal components of the contact velocity of the manipulator, i.e., vector  $\mathbf{v}_b^-$ . Thus, any  $\mathbf{v}_b^-$  that generates a post-impact velocity of the object satisfying (6.10) is a solution.



Due to physical continuity, the feasible solutions with variables (hitting direction, normal velocity, and tangential velocity) will constitute a surface in 3D space. Fig. 6.6 presents an example.

Of these solutions we would like to find the optimal motion of the manipulator to achieve the task. The kinetic energy of the manipulator is introduced to characterize the effort of the manipulator. It is minimized here. Golden section search is applied to find the optimal point, marked red in Fig. 6.6. It corresponds to the pre-impact motion of the manipulator at (0.95, 4.05, 0.12). The hit generates the motion plotted in Fig. 6.7.

## 6.4 Three-Dimensional Frictionless Impact Planning

In this section, we look at the impact planning of the planning task in 3D. As in 2D case, we first consider the planning task in the absence of friction.

### 6.4.1 Impact Dynamics and Contact Kinematics

Since it is in 3D plane, the angular velocities of the manipulator and the object now becomes a 3D vector, denoted by  $\boldsymbol{\omega}_b$  and  $\boldsymbol{\omega}_o$ , respectively. For  $i = o, b$ ,  $\boldsymbol{\omega}_i$  is often described in terms of a fixed frame  $\mathcal{F}_i$  coincident with its canonical frame at its center of mass. Under the canonical frame, the angular inertia matrix  $Q_i$  is diagonalized. Since the manipulator or the object does not move during the infinitesimal impact period, we can look at the change in its angular velocity during the impact with respect to the same fixed frame  $\mathcal{F}_i$ . The rotation matrix  $R_i$  describes the orientation of  $\mathcal{F}_i$  relative to the world frame. From (20) we know that the changes in their velocities and angular velocities during the impact are

$$\begin{aligned} \Delta \mathbf{V}_o &= \frac{1}{m_o} \mathbf{I}, & \Delta \boldsymbol{\omega}_o &= Q_o^{-1} (\mathbf{r}_o \times (R_o^{-1} \mathbf{I})), \\ \Delta \mathbf{V}_b &= -\frac{1}{m_b} \mathbf{I}, & \Delta \boldsymbol{\omega}_b &= -Q_b^{-1} (\mathbf{r}_b \times (R_b^{-1} \mathbf{I})), \end{aligned} \quad (6.33)$$

During the impact, the contact velocity changes by the amount

$$\begin{aligned}
\Delta \mathbf{v} &= \Delta \mathbf{V}_o + R_o(\Delta \boldsymbol{\omega}_o \times \mathbf{r}_o) - \Delta \mathbf{V}_b - R_b(\Delta \boldsymbol{\omega}_b \times \mathbf{r}_b) \\
&= \frac{1}{m_o} \mathbf{I} + R_o(Q_o^{-1}(\mathbf{r}_o \times (R_o^{-1} \mathbf{I})) \times \mathbf{r}_o) + \frac{1}{m_b} \mathbf{I} + R_b(Q_b^{-1}(\mathbf{r}_b \times (R_b^{-1} \mathbf{I})) \times \mathbf{r}_b) \\
&= \left( \frac{1}{m_o} + \frac{1}{m_b} \right) \mathbf{I} - (R_o P_o Q_o^{-1} P_o R_o^{-1} + R_b P_b Q_b^{-1} P_b R_b^{-1}) \mathbf{I} \\
&= \left( \left( \frac{1}{m_o} + \frac{1}{m_b} \right) \begin{pmatrix} 1 & 0 & 0 \\ 0 & 1 & 0 \\ 0 & 0 & 1 \end{pmatrix} - R_o P_o Q_o^{-1} P_o R_o^{-1} - R_b P_b Q_b^{-1} P_b R_b^{-1} \right) \mathbf{I} \\
&= A \mathbf{I},
\end{aligned} \tag{6.34}$$

where

$$A = \left( \left( \frac{1}{m_o} + \frac{1}{m_b} \right) \begin{pmatrix} 1 & 0 & 0 \\ 0 & 1 & 0 \\ 0 & 0 & 1 \end{pmatrix} - R_o P_o Q_o^{-1} P_o R_o^{-1} - R_b P_b Q_b^{-1} P_b R_b^{-1} \right).$$

From Section 6.2.1 we know that the total impulse when restitution ends is

$$I_r = -\frac{(1+e)(\mathbf{v}^- \cdot \hat{\mathbf{n}})}{\hat{\mathbf{n}}^T A \hat{\mathbf{n}}} = -\frac{(1+e)v_n^-}{\hat{\mathbf{n}}^T A \hat{\mathbf{n}}}. \tag{6.35}$$

#### 6.4.2 Motion Planning

With the impact outcome available, we are ready to plan the motion of the flying object in 3D space. As in 2D case, we still assume that the manipulator is batting the object rightward, i.e.,  $n_x > 0$  in  $\hat{\mathbf{n}} = (n_x, n_y, n_z)^T$ . From (6.33) and (6.35),

$$\begin{aligned}
\Delta \mathbf{V}_o &= \frac{I_r}{m_o} \cdot \hat{\mathbf{n}} \\
&= -\frac{(1+e)(\mathbf{v}^- \cdot \hat{\mathbf{n}})}{m_o \hat{\mathbf{n}}^T A \hat{\mathbf{n}}} \cdot \hat{\mathbf{n}} \\
&= -\frac{(1+e)(v_{on}^- - v_{bn}^-)}{m_o \hat{\mathbf{n}}^T A \hat{\mathbf{n}}} \cdot \hat{\mathbf{n}},
\end{aligned} \tag{6.36}$$

where  $v_{on}^- = \mathbf{v}_o^- \cdot \hat{\mathbf{n}}$  and  $v_{bn}^- = \mathbf{v}_b^- \cdot \hat{\mathbf{n}}$ . In the absence of friction the other components of  $\mathbf{v}_b^-$  will not affect the behavior of the object after impact, we consider  $v_{bn}^-$  as the only variable. From (6.36), the velocity of the object after impact is given by

$$\begin{aligned} \mathbf{V}_o^+ &= \mathbf{V}_o^- + \Delta \mathbf{V}_o \\ &= \mathbf{V}_o^- - \frac{(1+e)(v_{on}^- - v_{bn}^-)}{m_o \hat{\mathbf{n}}^T A \hat{\mathbf{n}}} \cdot \hat{\mathbf{n}}. \end{aligned} \quad (6.37)$$

Given a target destination  $\mathbf{q} = (q_x, q_y, q_z)^T$ , it needs to satisfy the kinematic equations:

$$\mathbf{q} + \mathbf{r}_o = \mathbf{V}_o^+ t - (0, 0, 0.5g)^T t^2, \quad (6.38)$$

for some flying time  $t$ , where  $g$  is the gravitational acceleration.

Suppose we fix an impact normal. Then in the system of (6.38), we have two variables  $v_{bn}^-$  and  $t$ . This is an overconstrained problem, which means that in most cases we cannot accomplish the planning task. Therefore, it is necessary to relax the constraint of the fixed impact normal. The impact normal can be parameterized as

$$\hat{\mathbf{n}} = (\cos \phi, \sin \phi \cos \theta, \sin \phi \sin \theta), \quad \phi \in [0, \pi/2], \quad \theta \in [0, 2\pi). \quad (6.39)$$

Varying the impact normal introduces two more degrees of freedom into the system. Now we have four variables  $v_{bn}^-$ ,  $\phi$ ,  $\theta$ , and  $t$  in three equations (6.38), which ends up with one-dimensional set of the solution. Let  $\beta = (1+e)/(m_o \hat{\mathbf{n}}^T A \hat{\mathbf{n}})$ . Substitute (6.37) into (6.38),

$$q_x = V_{ox}^- t - \beta n_x V_{on}^- t + \beta n_x v_{bn}^- t - r_{ox}, \quad (6.40)$$

$$q_y = V_{oy}^- t - \beta n_y V_{on}^- t + \beta n_y v_{bn}^- t - r_{oy}, \quad (6.41)$$

$$q_z = V_{oz}^- t - \beta n_z V_{on}^- t + \beta n_z v_{bn}^- t - r_{oz} - 0.5gt^2. \quad (6.42)$$

Solve  $v_{bn}^-$ ,  $t$  from (6.40) and (6.41),

$$v_{bn}^- = \frac{(q_y + r_{oy})(V_{ox}^- - \beta n_x V_{on}^-) - (q_x + r_{ox})(V_{oy}^- - \beta n_y V_{on}^-)}{(q_x + r_{ox})\beta n_y - (q_y + r_{oy})\beta n_x}, \quad (6.43)$$

$$t = \frac{(q_x + r_{ox})n_y - (q_y + r_{oy})n_x}{n_y V_{ox}^- - n_x V_{oy}^-}. \quad (6.44)$$

Substitute (6.43), (6.44), and (6.39) into (6.42), we obtain a curve  $C(\phi, \theta) = 0$  in terms of  $\phi$  and  $\theta$ . Fig. 6.8 shows an example of the curve.

Among these solutions we would like to achieve the optimal motion of the manipulator to finish the task. As in Section 6.3, The kinetic energy of the manipulator is introduced as the metric to characterize the effort. More formally, the problem becomes:

$$\begin{aligned} \text{Minimize } E &= \frac{1}{2}m_b(v_{bn}^-)^2 \\ \text{s.t. } C(\phi, \theta) &= 0. \end{aligned} \quad (6.45)$$

Fig. 6.9 presents the kinetic energy curve corresponds to the example from Fig. 6.8. Based on the derivatives with respect to  $\phi$  and  $\theta$  we apply golden section search to track along the curve until the optimal point is reached. The optimal solution is marked red in Fig. 6.9.

## 6.5 Three-Dimensional Frictional Impact Planning

In this section, let's look at the 3D planning task with friction.

### 6.5.1 Impact Dynamics and Contact Kinematics

Adding contact friction, we need to consider the tangential impulse between the object and the manipulator during impact. The impulse  $\mathbf{I}$  can be decomposed along the normal and tangential directions:

$$\begin{aligned} \mathbf{I} &= \mathbf{I}_\perp + I_n \hat{\mathbf{n}} \\ &= I_u \hat{\mathbf{u}} + I_w \hat{\mathbf{w}} + I_n \hat{\mathbf{n}}, \end{aligned}$$

where  $\hat{\mathbf{u}}$  and  $\hat{\mathbf{w}}$  are two orthogonal unit vectors spanning the tangent plane, and  $I_n$ ,  $I_u$  and  $I_w$  are the magnitudes the normal and the two tangential impulses. From (6.34) the tangential contact velocity changes by the amount:

$$\Delta \mathbf{v}_\perp = (1 - \hat{\mathbf{n}}\hat{\mathbf{n}}^T)A\mathbf{I}.$$

Then the tangential contact velocity is

$$\begin{aligned}\mathbf{v}_\perp &= \mathbf{v}_\perp^- + \Delta\mathbf{v}_\perp \\ &= \mathbf{v}_\perp^- + (1 - \hat{\mathbf{n}}\hat{\mathbf{n}}^T)A\mathbf{I},\end{aligned}\tag{6.46}$$

where  $\mathbf{v}_\perp^-$  is the value right before the impact.

As in 2D frictional case, contact modes transition needs to be considered.

### 6.5.1.1 Sliding

The contact slides when tangential velocity is non-zero, i.e.  $\mathbf{v}_\perp \neq \mathbf{0}$ . Under Coulomb's law of friction, the tangential contact force  $\mathbf{F}_\perp$  and the normal contact force  $\mathbf{F}_n$  follows the relationship:

$$\mathbf{F}_\perp = -\mu\mathbf{F}_n = -\mu F_n \hat{\mathbf{v}}_\perp = -\mu F_n \frac{\mathbf{v}_\perp}{\|\mathbf{v}_\perp\|}.$$

Take the derivative of  $\mathbf{I}_\perp$  with respect to  $I_n$ ,

$$\mathbf{I}'_\perp = \frac{d\mathbf{I}_\perp}{dI_n} = \frac{\mathbf{F}_\perp}{F_n} = -\mu \frac{\mathbf{v}_\perp}{\|\mathbf{v}_\perp\|}.$$

From (6.46), we have

$$\begin{aligned}I'_u &= \frac{dI_u}{dI_n} = \hat{\mathbf{u}}^T \frac{d\mathbf{I}_\perp}{dI_n} \\ &= -\frac{\mu \hat{\mathbf{u}}^T}{\|\mathbf{v}_\perp\|} (\mathbf{v}_\perp^- + (1 - \hat{\mathbf{n}}\hat{\mathbf{n}}^T)A\mathbf{I}) \\ &= -\frac{\mu}{\|\mathbf{v}_\perp\|} (v_{\perp u}^- + \hat{\mathbf{u}}^T (1 - \hat{\mathbf{n}}\hat{\mathbf{n}}^T)A\mathbf{I}) \\ &= -\frac{\mu}{\|\mathbf{v}_\perp\|} (v_{\perp u}^- + \hat{\mathbf{u}}^T A\mathbf{I}),\end{aligned}\tag{6.47}$$

$$\begin{aligned}I'_w &= \frac{dI_w}{dI_n} \\ &= -\frac{\mu}{\|\mathbf{v}_\perp\|} (v_{\perp w}^- + \hat{\mathbf{w}}^T A\mathbf{I}).\end{aligned}\tag{6.48}$$

### 6.5.1.2 Sticking

The contact sticks when the tangential contact velocity becomes zero, i.e.,  $\mathbf{v}_\perp = \mathbf{0}$ .

Take the derivative of  $\mathbf{v}_\perp$  with respect to  $I_n$ ,

$$\mathbf{v}'_\perp = \frac{d\mathbf{v}_\perp}{dI_n} = (1 - \hat{\mathbf{n}}\hat{\mathbf{n}}^T)A \frac{d\mathbf{I}}{dI_n} = (1 - \hat{\mathbf{n}}\hat{\mathbf{n}}^T)A(\mathbf{I}'_\perp + \hat{\mathbf{n}}).$$

In order to maintain sticking,  $\mathbf{v}'_\perp = \mathbf{0}$ . Namely,

$$\hat{\mathbf{u}}^T A(\mathbf{I}'_\perp + \hat{\mathbf{n}}) = 0, \quad (6.49)$$

$$\hat{\mathbf{w}}^T A(\mathbf{I}'_\perp + \hat{\mathbf{n}}) = 0. \quad (6.50)$$

Expand the left hand side of (6.50),

$$\begin{aligned} \hat{\mathbf{u}}^T A(\mathbf{I}'_\perp + \hat{\mathbf{n}}) &= \hat{\mathbf{u}}^T A(I'_u \hat{\mathbf{u}} + I'_w \hat{\mathbf{w}} + \hat{\mathbf{n}}) \\ &= \hat{\mathbf{u}}^T A I'_u \hat{\mathbf{u}} + \hat{\mathbf{u}}^T A I'_w \hat{\mathbf{w}} + \hat{\mathbf{u}}^T A \hat{\mathbf{n}}. \end{aligned}$$

Equation (6.50) becomes:

$$\hat{\mathbf{u}}^T A \hat{\mathbf{u}} I'_u + \hat{\mathbf{u}}^T A \hat{\mathbf{w}} I'_w = -\hat{\mathbf{u}}^T A \hat{\mathbf{n}}. \quad (6.51)$$

Similarly, from (6.50) we obtain

$$\hat{\mathbf{w}}^T A \hat{\mathbf{u}} I'_u + \hat{\mathbf{w}}^T A \hat{\mathbf{w}} I'_w = -\hat{\mathbf{w}}^T A \hat{\mathbf{n}}. \quad (6.52)$$

Consider the coefficient matrix of equations (6.51) and (6.52):

$$M = \begin{pmatrix} \hat{\mathbf{u}}^T A \hat{\mathbf{u}} & \hat{\mathbf{u}}^T A \hat{\mathbf{w}} \\ \hat{\mathbf{w}}^T A \hat{\mathbf{u}} & \hat{\mathbf{w}}^T A \hat{\mathbf{w}} \end{pmatrix} \quad (6.53)$$

There are three cases:

a)  $\text{rank}(M) = 2$ . Solve (6.51) and (6.52) for  $I'_u$  and  $I'_w$ , which results in constant values  $\beta_u$  and  $\beta_w$ , respectively. Thus, we have

$$\mathbf{I}'_\perp = \beta_u \hat{\mathbf{u}} + \beta_w \hat{\mathbf{w}}.$$

If

$$\|\mathbf{F}_\perp/F_n\| = \|\mathbf{I}'_\perp\| = \sqrt{\beta_u^2 + \beta_w^2} < \mu, \quad (6.54)$$

tangential impulse due to friction will be enough to keep the contact sticking. Let  $\Delta I_n$  be the accumulation of the normal impulse since the beginning of sticking. Then the tangential impulse accumulation during the same period is

$$\Delta I_\perp = (\beta_u \hat{\mathbf{u}} + \beta_w \hat{\mathbf{w}}) \Delta I_n. \quad (6.55)$$

If condition (6.54) does not hold, the contact will not stick and sliding will continue.

b)  $\text{rank}(M) = 1$  and  $(-\hat{\mathbf{u}}^T A \hat{\mathbf{n}}, -\hat{\mathbf{w}}^T A \hat{\mathbf{n}})^T \in \text{col}(M)$ . In this case (6.51) and (6.52) are multiples of each other. Only one of them needs to be considered, say, equation (6.51). It defines a line in the  $I'_u - I'_w$  plane. Let  $(\beta_u, \beta_w)$  be the foot of the perpendicular from the origin to the line. If its distance  $\sqrt{\beta_u^2 + \beta_w^2} < \mu$ , then the contact will stay in the sticking mode. We can determine  $\Delta \mathbf{I}_\perp$  from (6.55) with the current  $\beta_u$  and  $\beta_w$  values. Otherwise, if  $\sqrt{\beta_u^2 + \beta_w^2} \geq \mu$ , the contact will not stick.

c)  $\text{rank}(M) = 1$  but  $(-\hat{\mathbf{u}}^T A \hat{\mathbf{n}}, -\hat{\mathbf{w}}^T A \hat{\mathbf{n}})^T \notin \text{col}(M)$ . No solution satisfies (6.51) and (6.52). The contact will never stick.

### 6.5.1.3 Compression and Restitution

Denote by  $v_n$  the normal component of the contact velocity  $\mathbf{v}$ . From (6.34), we have

$$\begin{aligned} v_n &= \hat{\mathbf{n}}^T (\mathbf{v}^- + \Delta \mathbf{v}) \\ &= v_n^- + \hat{\mathbf{n}}^T A \mathbf{I}. \end{aligned}$$

The change rate of the energy throughout the impact is

$$\begin{aligned} E' &= -v_n \\ &= -v_n^- - \hat{\mathbf{n}}^T A \mathbf{I}. \end{aligned} \quad (6.56)$$

Based on the impact model, compression ends when  $v_n = 0$ . At this point, maximum energy  $E_{\max}$  is stored at the contact. Immediately, the energy dissipates by a factor of  $e^2$ , where  $e$  is the energy coefficient of restitution. Restitution ends when  $E = 0$ .

We apply numerical integration to solve the impact results as in Chapter 5. The difference is that here when the sticking mode is reached, there is a closed form for the change in the impulse so we can stop numerical integration and solve the results directly.

Let the normal impulse  $I_n$  increase from zero. As  $I_n$  reaches certain value, a phase of impact will end or the contact mode will vary. When the contact is sliding, the change of the tangential impulse  $\mathbf{I}_{\perp}$  is tracked from integrating (6.47) and (6.48), while the energy change is tracked by integrating (6.56). At the point when sticking is reached before the impact ends,  $\mathbf{I}'_{\perp}$  will become constant. Thus, the change in the tangential impulse has a closed form (6.55) in terms of the change in  $I_n$ . So do the changes in  $\mathbf{I}$  and  $E$ . The condition (6.54), if holds, will hold until the end of the impact. A closed-form analysis can be performed after sticking to solve the value of  $\mathbf{I}$  at the end of the impact.

### 6.5.2 Motion Planning

Since we can compute the outcome of the impact in 3D case with friction, we would like to plan the motion of the flying object. With known pre-impact configuration, the velocity of the object after impact, though no closed-form solution exists, can be represented as a function in terms of the contact normal  $\hat{\mathbf{n}} = (n_x, n_y, n_z)^T$ , and the pre-impact contact velocity of the manipulator  $\mathbf{v}_b^- = (v_{bx}^-, v_{by}^-, v_{bz}^-)^T$ .

To simplify the problem and reduce degrees of freedom for better analysis, we fixed the impact normal, and check with a given normal, whether we can plan the velocity of the manipulator in order to hit the flying object to reach the target  $\mathbf{q}$ . The post-impact velocity of the object can be represented as  $\mathbf{V}_o^+ = \mathbf{V}_o^+(v_{bx}^-, v_{by}^-, v_{bz}^-) = (V_{ox}^+, V_{oy}^+, V_{oz}^+)$ . The



kinematic equations (6.38) needs to be satisfied. By eliminating  $t$ , we have

$$V_{ox}^+(q_y + r_{oy}) - V_{oy}^+(q_x + r_{ox}) = 0, \quad (6.57)$$

$$(V_{ox}^+)^2(q_z + r_{oz}) - V_{ox}^+V_{oz}^+(q_x + r_{ox}) + \frac{1}{2}g(q_x + r_{ox})^2 = 0, \quad (6.58)$$

which are two constraints with three variables, resulting in one dimensional set of solution. As in Section 6.4, we apply the kinetic energy of the manipulator to characterize the effort. Minimizing the kinetic energy  $E = \frac{1}{2}m_b ((v_{bx}^-)^2 + (v_{by}^-)^2 + (v_{bz}^-)^2)$  is equivalent to minimize  $(v_{bx}^-)^2 + (v_{by}^-)^2 + (v_{bz}^-)^2$ , since  $\frac{1}{2}m_b$  is a constant. Combined with (6.57) and (6.58), the problem becomes:

$$\begin{aligned} \text{Minimize } & f(\mathbf{v}_b^-) = (v_{bx}^-)^2 + (v_{by}^-)^2 + (v_{bz}^-)^2 \\ \text{s.t. } & g_1(\mathbf{v}_b^-) = V_{ox}^+(q_y + r_{oy}) - V_{oy}^+(q_x + r_{ox}) = 0 \\ & g_2(\mathbf{v}_b^-) = (V_{ox}^+)^2(q_z + r_{oz}) - V_{ox}^+V_{oz}^+(q_x + r_{ox}) + \frac{1}{2}g(q_x + r_{ox})^2 = 0. \end{aligned} \quad (6.59)$$

To solve this problem, we apply the Lagrange multipliers in numerical optimization. Introducing Lagrange multipliers  $\lambda_1$  and  $\lambda_2$  for the two constraints, we define the following Lagrangian function on 5 variables:

$$\mathcal{L}(\mathbf{v}_b^-, \lambda_1, \lambda_2) = f(\mathbf{v}_b^-) + \lambda_1 g_1(\mathbf{v}_b^-) + \lambda_2 g_2(\mathbf{v}_b^-).$$

The constrained optimization problem can be converted into an unconstrained root-finding problem. More formally, we would like to find a point  $(\mathbf{v}_b^-, \lambda_1, \lambda_2)$  such that

$$\nabla \mathcal{L}(\mathbf{v}_b^-, \lambda_1, \lambda_2) = \begin{pmatrix} \nabla f(\mathbf{v}_b^-) + \lambda_1 \nabla g_1(\mathbf{v}_b^-) + \lambda_2 \nabla g_2(\mathbf{v}_b^-) \\ g_1(\mathbf{v}_b^-) \\ g_2(\mathbf{v}_b^-) \end{pmatrix} = \mathbf{0}.$$

Newton's method is applied to solve this multivariate root-finding problem. We iterate  $(\mathbf{v}_b^-, \lambda_1, \lambda_2)$  as below:

$$(\mathbf{v}_{b,n+1}^-, \lambda_{1,n+1}, \lambda_{2,n+1}) = (\mathbf{v}_{b,n}^-, \lambda_{1,n}, \lambda_{2,n}) - \nabla^2 \mathcal{L}(\mathbf{v}_{b,n}^-, \lambda_{1,n}, \lambda_{2,n})^{-1} \nabla \mathcal{L}(\mathbf{v}_{b,n}^-, \lambda_{1,n}, \lambda_{2,n}),$$

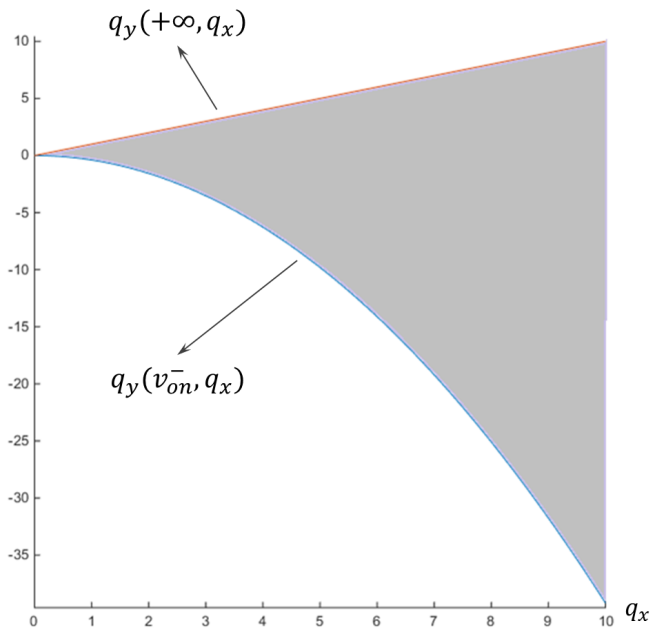
Table 6.2 Iterations of Newton's method.

iteration	$(\mathbf{v}_b^-, \lambda_1, \lambda_2)$	$f(\mathbf{v}_b^-)$
1	(0.2174,-2.1791,1.8988,-7.8101,-0.1714)	8.4015
2	(0.1787,-1.4909,0.9923,0.9744,0.0959)	3.2394
3	(0.1776,-1.2806,-0.2799,-2.4788,-0.2214)	1.7499
4	(0.1776,-1.2538,-0.2192,-1.7836,0.0193)	1.6517
5	(0.1776,-1.2438,-0.2497,-1.1521,0.0124)	1.6408
6	(0.1776,-1.2362,-0.2792,-1.1703,0.0125)	1.6375
7	(0.1776,-1.2319,-0.2953,-1.1777,0.0126)	1.6364
8	(0.1776,-1.2295,-0.3047,-1.1818,0.0127)	1.636
9	(0.1776,-1.228,-0.3103,-1.1841,0.0127)	1.6359
10	(0.1776,-1.2271,-0.3138,-1.1855,0.0127)	1.6358
11	(0.1776,-1.2266,-0.3158,-1.1863,0.0127)	1.6358

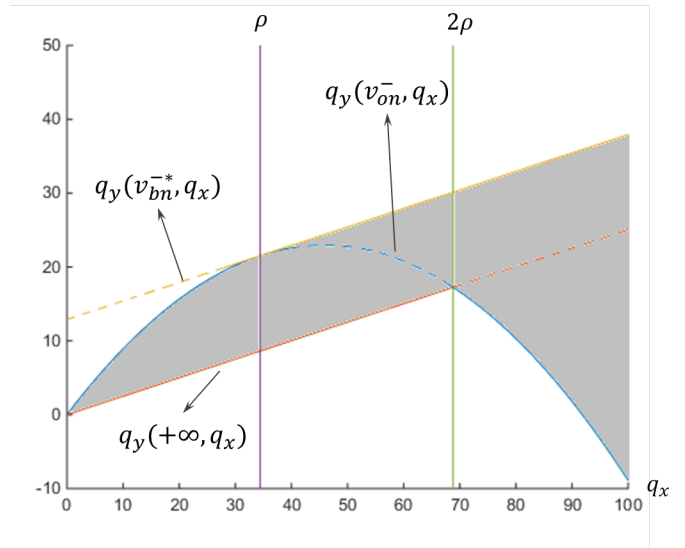
in which the Hessian of the Lagrangian is given by the following matrix

$$\nabla^2 \mathcal{L}(\mathbf{v}_b^-, \lambda_1, \lambda_2) = \begin{pmatrix} \nabla^2 f(\mathbf{v}_b^-) + \lambda_1 \nabla^2 g_1(\mathbf{v}_b^-) + \lambda_2 \nabla^2 g_2(\mathbf{v}_b^-) & \nabla g_1(\mathbf{v}_b^-) & \nabla g_2(\mathbf{v}_b^-) \\ \nabla g_2(\mathbf{v}_b^-)^T & 0 & 0 \\ \nabla g_1(\mathbf{v}_b^-)^T & 0 & 0 \end{pmatrix}.$$

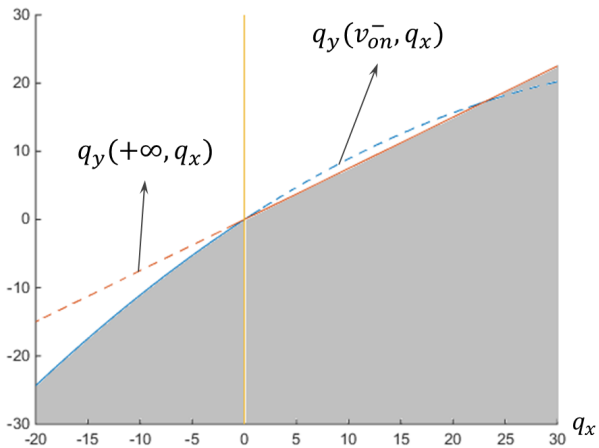
Since there is no closed form for  $\mathbf{V}_o^+$ , We use numerical differentiation to approximate the first and second derivatives. Next we presents an example, in which the object and the manipulator had mass 1 and 20, respectively. The coefficient of friction  $\mu$  is 0.2, and the coefficient of restitution  $e$  is 0.95. Put the hitting point at the origin, the target destination is  $\mathbf{q} = (10, -10, 460)$ . The hitting normal is  $\hat{\mathbf{n}} = (0.952, -0.051, 0.303)$ . Before impact the velocity and angular velocity of the object are  $(-1, -1, -1)$  and  $(0, \pi/4, \pi/4)$ , respectively. Table 6.2 shows the iterations of the Newton's method in the example. During the iterating process  $\nabla \mathcal{L}(\mathbf{v}_b^-, \lambda_1, \lambda_2)$  gradually converges to  $\mathbf{0}$ . The optimum is achieved at  $\mathbf{v}_b^- = (0.1776, -1.2266, -0.3158)$ .



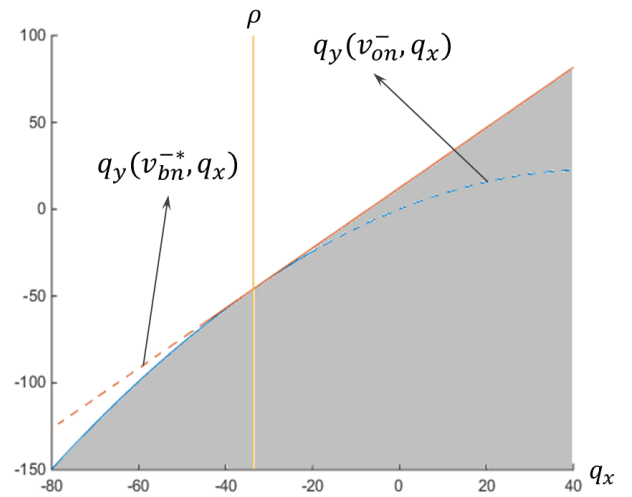
(a)



(b)



(c)



(d)

Figure 6.2 Example of reachable regions (gray area) of the object in the cases: (a)  $V_{ox}^- > 0, \mathbf{V}_o^- \times \hat{\mathbf{n}} \geq 0$ ; (b)  $V_{ox}^- > 0, \mathbf{V}_o^- \times \hat{\mathbf{n}} < 0$ ; (c)  $V_{ox}^- \leq 0, \mathbf{V}_o^- \times \hat{\mathbf{n}} \geq 0$ ; (d)  $V_{ox}^- \leq 0, \mathbf{V}_o^- \times \hat{\mathbf{n}} < 0$ .

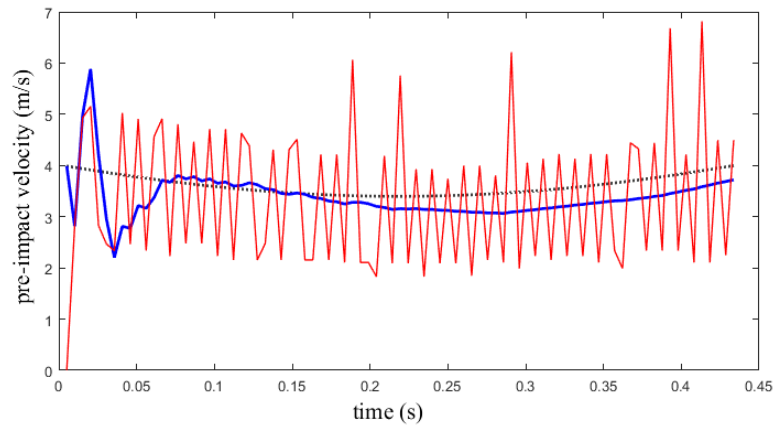
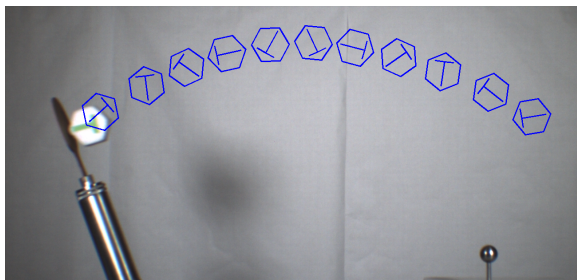
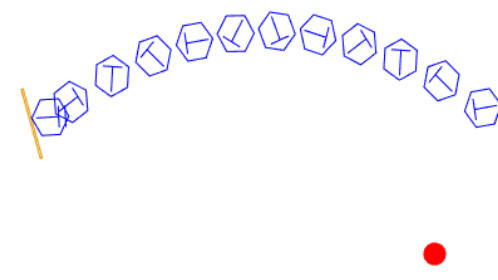


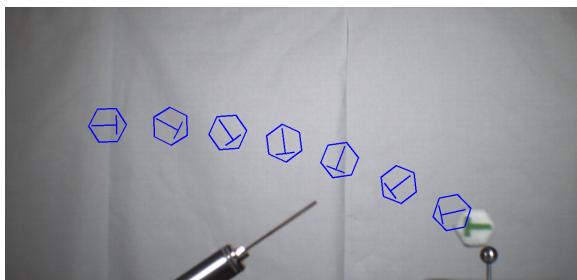
Figure 6.3 Magnitude of linear velocity from image processing (red line), kinematics (gray dotted line), and the Kalman filter's estimation (blue line).



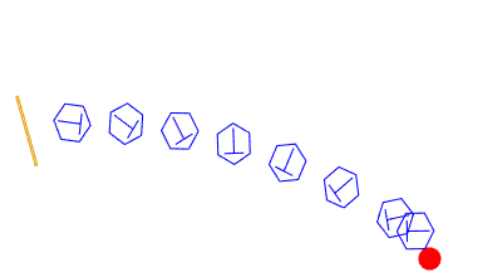
(a)



(b)

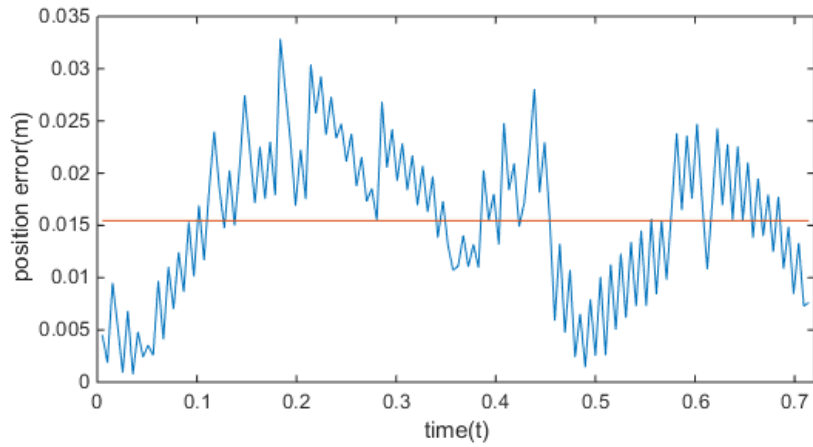


(c)

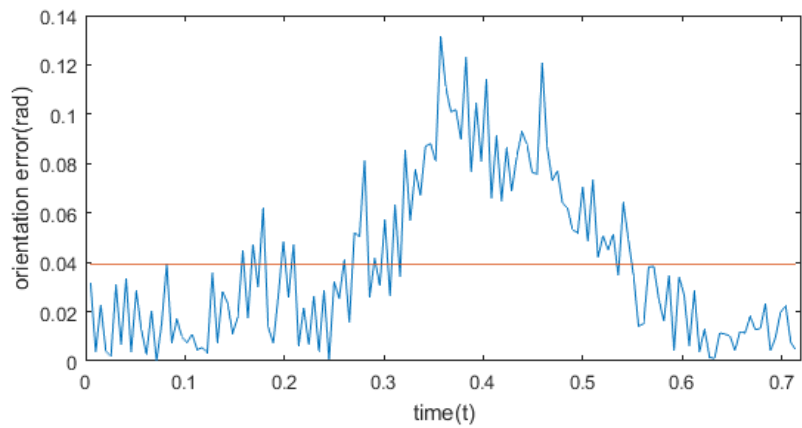


(d)

Figure 6.4 Trajectories of the planning task: pre-impact in (a) experiment and (b) simulation, post-impact in (c) experiment and (d) simulation.



(a)



(b)

Figure 6.5 Discrepancies between experiment and simulation along time in (a) position, and (b) orientation. The red line represents the average error throughout the process.

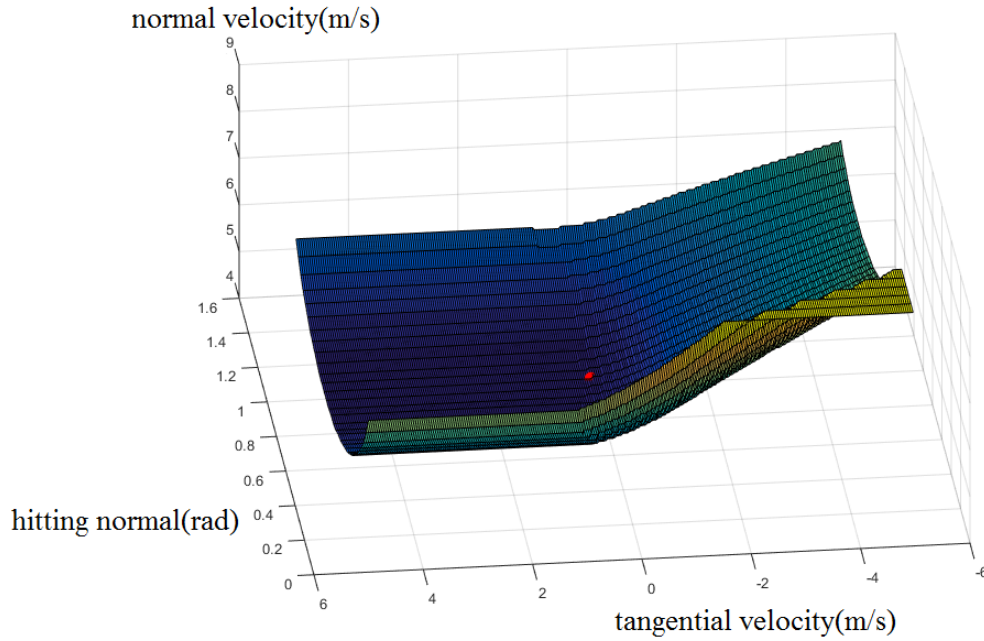


Figure 6.6 Solution surface of the frictional planning example for different hitting normal, tangential velocity, and normal velocity of the manipulator.

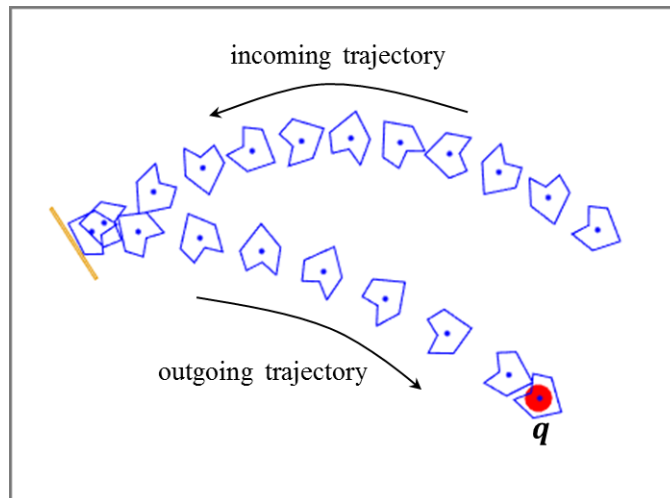


Figure 6.7 Trajectory of the optimal planning result.

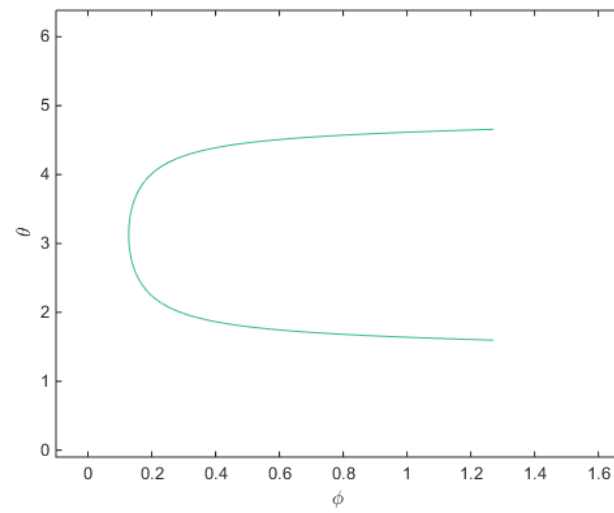


Figure 6.8 Solution curve of the 3D frictionless planning example for different hitting normal.

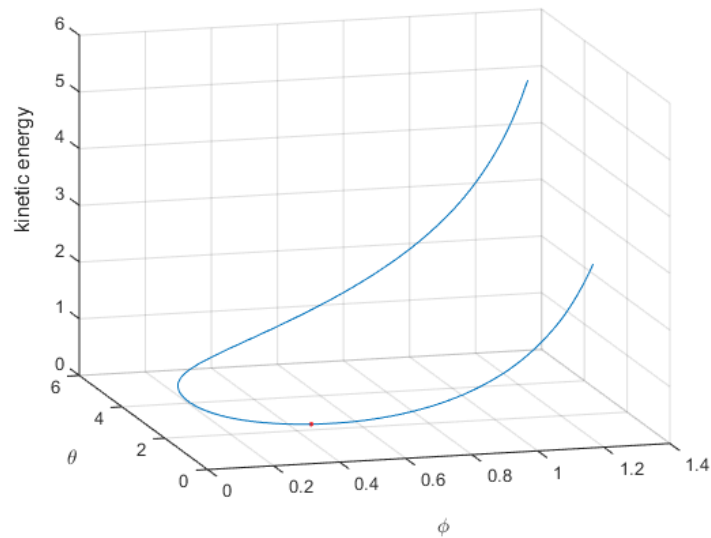


Figure 6.9 Kinetic energy curve of the 3D frictionless planning example for different  $\phi$  and  $\theta$ .

With the root found, we now solve the problem described by (6.59). Given an impact normal, we check whether the manipulator can hit the object to reach the target. If so, we obtain the best way which takes the least effort of the manipulator. Otherwise, it means that the manipulator cannot hit the object to the target with the current given hitting normal.



## CHAPTER 7. CONCLUSION

In this thesis we first introduce two types of squeezes on a deformable object. A stable squeeze minimizes the potential energy for the same amount of squeeze. A pure squeeze makes sure that the grasped object undergoes no rigid body motion during deformation to avoid unnecessary finger movements. And then we study the best strategy to resist an adversary finger poking against a grasped object via known translation. Our introduced metric is the amount of work performed by the grasping fingers, rather than the total force as usually used in rigid body grasping. Optimal resistance strategies are first analyzed assuming fixed point and segment contacts. Then, Algorithm 1 is proposed for area contacts under Coulomb friction, by incorporating the contact event detection subroutine from (15).

Next, we also propose a simple squeeze-and-lift strategy for grasping 3D deformable objects. The idea is to model changes in shape and contact geometry during the deformation, and repeatedly conduct liftability tests to predict when to switch the action from squeezing to lifting. To support the modeling, we extended our contact-based finite element analysis to 3D, with gravity taken into account.

After that a computational efficiently impact model for  $n$ -body system is introduced, in both frictionless and frictional cases. Simulation and experiment on Newton's cradle to validate the model in the frictionless case and simulation in the frictional case are performed, which give realistic outcomes.

Based on the impact model, we investigate the motion planning of batting a flying object to some target in both frictionless and frictional cases. Experiment was performed

to validate the planning strategy compared with simulation for 2D frictionless case. Although 2D analysis is complete and concise, it is not realistic and not easy to verify via experiments. Thus, analyses are generalized to 3D with or without friction. The result in the frictionless case is similar to 2D, but with one-dimensional set of solution. For the frictional case in 3D, the problem is converted into a root-finding one and Newton's method is applied to solve the optimal planning.

For future work, experiments with a 4-DOF WAM Arm can be performed to valid the model and algorithms. And also, in the current analysis tangential compliance during impact is ignored. Nevertheless, in some situations, like playing ping pong ball, tangential compliance plays a significant role affecting the impact outcome. Therefore, adding tangential compliance into the model is necessary for the next step.

## BIBLIOGRAPHY

- [1] Allgower EL and Georg K, Numerical path following, in *Handbook of Numerical Analysis*, vol. 5, North-Holland, 1997.
- [2] Bicchi A and Kumar V. Robotic grasping and contact: a review. In *Proceedings of the IEEE International Conference on Robotics and Automation*, pp. 348–353, 2000.
- [3] Bower AF. *Applied Mechanics of Solids*. CRC Press, 2009.
- [4] Boyd SP and Wegbreit B, Fast computation of optimal contact forces, *Robotics, IEEE Transactions*, vol. 23, pp. 1117–1132, 2007.
- [5] Brost RC and Goldberg KY. A complete algorithm for synthesizing modular fixtures for polygonal parts. In *Proceedings of the IEEE International Conference on Robotics and Automation*, pp. 535–542, 1994.
- [6] Buss M, Faybusovich L, and Moore J. Dikin-type algorithms for dexterous grasping force optimization, *The International Journal of Robotics Research*, vol. 17, pp. 831–839, 1998.
- [7] Chandrasekaran N, Haisler WE, and Goforth RE. A finite element solution method for contact problems with friction, *International Journal for Numerical Methods in Engineering*, 24:477–495, 1987.
- [8] Crandall SH, Dahl NC, and Lardner TJ. *An Introduction to the Mechanics of Solids*. McGraw-Hill, Inc., 2nd edition, 1978.

- [9] Cross R. Mechanics of swinging a bat. *American Journal of Physics*, 77:36-43, 2010.
- [10] Duda RO. and Hart PE. Use of the hough transformation to detect lines and curves in pictures. *Communications of the ACM*, 15(1):1115, 1972.
- [11] Francavilla A and Zienkiewicz OC. A note on numerical computation of elastic contact problems. *International Journal for Numerical Methods in Engineering*, 9:913–924, 1975.
- [12] Fung YC and Tong P. *Classical and Computational Solid Mechanics*. World Scientific, 2001.
- [13] Gallagher RH. *Finite Element Analysis*. Prentice-Hall, Inc., 1975.
- [14] Gopalakrishnan K and Goldberg K, D-space and deform closure grasps of deformable parts. *The International Journal of Robotics Research*, vol. 24, pp. 899–910, 2005.
- [15] Guo F, Lin H, and Jia YB. Squeeze grasping of deformable planar objects with segment contact and stick/slip transitions. In *Proceedings of the IEEE International Conference on Robotics and Automation*, 2013, pp. 3721–3726.
- [16] Hirai S, Tsuboi T, and Wada T. Robust grasping manipulation of deformable objects. In *Proceedings of the IEEE International Symposium on Assembly and Task Planning*, pp. 411–416, 2001.
- [17] Hirai S, Niwa M, and Kawamura S. Development of impulsive object sorting device with air floating. In *Proceedings of the IEEE International Conference on Robotics and Automation*, pp. 3065-3070, 1999.
- [18] Huang WH and Mason MT. Mechanics, planning, and control for tapping. *The International Journal of Robotics Research*, 19(10):883–894, 2000.

- [19] Jia YB. Planning the motion of a sliding and rolling sphere under friction. In *Proceedings of the IEEE International Conference on Robotics and Automation*, pp. 2396–2402, Seattle, WA, 2015.
- [20] Jia YB. Three-dimensional impact: energy-based modeling of tangential compliance. *The International Journal of Robotics Research*, vol. 32, no. 1, pp. 56–83, 2013.
- [21] Jia YB, Mason MT, and Erdmann M. Multiple impacts: A state transition diagram approach. *The International Journal of Robotics Research*, 32(1):84–114, 2012.
- [22] Jia YB. On computing optimal planar grasps. In *Proceedings of the IEEE/RSJ International Conference on Intelligent Robots and Systems*, pp. 3:427–434, 1995.
- [23] Keller JB. Impact with friction. *Journal of applied Mechanics*, 53(1):1–4, 1986.
- [24] Kerr J and Roth B. Analysis of multifingered hands. *The International Journal of Robotics Research*, vol. 4, pp. 3–17, 1986.
- [25] Kirkpatrick P. Batting the ball. *American Journal of Physics*, 31:606–613, 1963.
- [26] Ladd AM and Kavraki LE. Using motion planning for knot untangling. *International Journal of Robotics Research*, 23(7):797–808, 2004.
- [27] Li JW, Liu H, and Cai HG. On computing three-finger forceclosure grasps of 2-D and 3-D objects. In *Proceedings of the IEEE International Conference on Robotics and Automation*, vol. 19, pp. 155–161, 2003.
- [28] Li Z and Sastry SS. Task-oriented optimal grasping by multifingered robot hands. *Robotics and Automation, IEEE Journal*, vol. 4, pp. 32–44, 1988.
- [29] Liu C, Zhao Z, and Brogliato B. Frictionless multiple impacts in multibody systems. i. theoretical framework. *Proceedings of the Royal Society of London A: Mathematical, Physical and Engineering Sciences*, 464(2100):3193–3211, 2008.

- [30] Liu C, Zhao Z, and Brogliato B. Frictionless multiple impacts in multibody systems. ii. numerical algorithm and simulation results. *Proceedings of the Royal Society A: Mathematical, Physical and Engineering Science*, 465(2101):1–23, 2009.
- [31] Luo Q and Xiao J. Geometric properties of contacts involving a deformable object. In *Proceedings of the IEEE Symposium on Haptic Interfaces for Virtual Environment and Teleoperator Systems*, pp. 533–538, 2006.
- [32] Markenscoff X, Ni L, and Papadimitriou CH. The geometry of grasping. *International Journal of Robotics Research*, 9(1):61–74, 1990.
- [33] Markenscoff X and Papadimitriou CH, Optimum grip of a polygon. *The International Journal of Robotics Research*, vol. 8, pp. 17–29, 1989.
- [34] Mason MT. *Mechanics of Robotic Manipulation*. Cambridge, MA: The MIT Press, 2001.
- [35] Matsuno T and Fukuda T. Manipulation of flexible rope using topological model based on sensor information. In *Proceedings of the IEEE/RSJ International Conference on Intelligent Robots and Systems*, pp. 2638–2643, 2006.
- [36] Mishra B, Grasp metrics: optimality and complexity, in *Algorithmic Foundations of Robotics*, K. Goldberg et al. (ed.), pp. 137–165. A. K. Peters, Boston, MA, 1995.
- [37] Mirtich B and Canny J. Easily computable optimum grasps in 2-D and 3-D. In *Proceedings of the IEEE International Conference on Robotics and Automation*, 1994, pp. 739–741.
- [38] Mishra B, Schwartz JT, and Sharir M. On the existence and synthesis of multifinger positive grips. *Algorithmica*, 2(4):541–558, 1987.

- [39] Moll M and Kavraki LE. Path planning for deformable linear objects. *IEEE Transactions on Robotics and Automation*, 22(4):625–636, 2006.
- [40] Nguyen VD, Constructing force-closure grasps, *The International Journal of Robotics Research*, vol. 7, pp. 3–16, 1988.
- [41] Okamoto N and Nakazawa M. Finite element incremental contact analysis with various frictional conditions, *International Journal for Numerical Methods in Engineering*, 14:337–357, 1979.
- [42] Ponce J, Sullivan S, Sudsang A, Boissonnat J, and Merlet JP. On computing four-finger equilibrium and force-closure grasps of polyhedral objects, *International Journal of Robotics Research*, 16(1):11–35, 1997.
- [43] Ponce J, Stam D, and Faverjon B. On computing two-finger force-closure grasps of curved 2D objects, *International Journal of Robotics Research*, 12(3):263–273, 1993.
- [44] Remde A, Henrich D, and Worn H. Picking-up deformable linear objects with industrial robots. In *Proceedings of the International Symposium on Robotics*, Tokyo, Japan, 1999.
- [45] Rimon E and Blake A. Caging planar bodies by one-parameter two-fingered gripping systems, *International Journal of Robotics Research*, 18:299–318, 1999.
- [46] Rimon E and Burdick J. On force and form closure for multiple finger grasps. In *Proceedings of the IEEE International Conference on Robotics and Automation*, pp. 1795–1800, 1996.
- [47] Rodriguez A, Mason MT, and Ferry S. From caging to grasping, *International Journal of Robotics Research*, 31(7):886–900, 2012.

- [48] Sachdeva TD and Ramakrishnan CV. A finite element solution for the two-dimensional elastic contact problems with friction, *International Journal for Numerical Methods in Engineering*, 17:1257–1271, 1981.
- [49] Saha M and Isto P. Motion planning for robotic manipulation of deformable linear objects. In *Proceedings of the IEEE International Conference on Robotics and Automation*, pp. 2478–2484, 2006.
- [50] Senoo T, Namiki A, and Ishikawa M. Ball control in highspeed batting motion using hybrid trajectory generator. In *Proceedings of the IEEE International Conference on Robotics and Automation*, pages 1762–1767, 2006.
- [51] Senoo T, Namiki A, and Ishikawa M. High-speed batting using a multi-jointed manipulator. In *Proceedings of the IEEE International Conference on Robotics and Automation*, volume 2, pages 1191–1196, 2004.
- [52] Sinha PR and Abel JM. A contact stress model for multifingered grasps of rough objects, *IEEE Transactions on Robotics and Automation*, 8(1):7–22, 1992.
- [53] van der Stappen AF, Wentink C, and Overmars MH. Computing immobilizing grasps of polygonal parts, *International Journal of Robotics Research*, 19(5):467–479, 2000.
- [54] Stronge WJ. *Impact Mechanics*. Cambridge University Press, 2004.
- [55] Tagawa K, Hirota K, and Hirose M. *Manipulation of dynamically deformable object using impulse-based approach*. INTECH Open Access Publisher, 2010.
- [56] Tian J and Jia YB. Modeling deformations of general parametric shells grasped by a robot hand, *IEEE Transactions on Robotics*, 26(5):837–852, 2010.
- [57] Trinkle JC. On the stability and instantaneous velocity of grasped frictionless objects, *IEEE Transactions on Robotics and Automation*, 8(5):560–572, 1992.



- [58] Wakamatsu H, Arai E, and Hirai S. Knotting/unknotting manipulation of deformable linear objects, *International Journal of Robotics Research*, 25(4):371–395, 2006.
- [59] Wakamatsu H and Hirai S. Static modeling of linear object deformation based on differential geometry, *International Journal of Robotics Research*, 23(3):293–311, 2004.
- [60] Wakamatsu H, Hirai S, and Iwata K. Static analysis of deformable object grasping based on bounded force closure, In *Proceedings of the IEEE/RSJ International Conference on Intelligent Robots and Systems*, pp. 3324–3329, 1996.
- [61] Wang Y and Mason MT. Two-dimensional rigid-body collisions with friction. *Journal of Applied Mechanics*, 59: 635–642, 1992.
- [62] Wang YT, Kumar V, and Abel J. Dynamics of rigid bodies undergoing multiple frictional contacts. In *Proceedings of the IEEE International Conference on Robotics and Automation*, pages 2764–2769, 1992.